TUNNELING SPECTROSCOPY OF CARBON NANOSTRUCTURES: A ROMANCE IN MANY DIMENSIONS

BY

TRAVIS LEE DIRKS

DISSERTATION

Submitted in partial fulfillment of the requirements
for the degree of Doctor of Philosophy in Physics
in the Graduate College of the
University of Illinois at Urbana-Champaign, 2010

Urbana, Illinois

Doctoral Committee:

Associate Professor Alexey Bezryadin, Chair
Assistant Professor Nadya Mason, Director of Research
Professor John D. Stack
Assistant Professor Smitha Vishveshwara

Abstract

In this dissertation we present results from various methods of tunneling spectroscopy in carbon nanotubes, which shed light on electron – electron interaction in carbon nanotubes and low dimensional systems in general. We also apply those methods to two dimensional graphene sheets. We first review the fabrication techniques used to make the devices studied here. Some of the techniques are standard in nanofabrication, and some were developed in-house to make the particular device geometries studied here possible. In particular, we developed recipes for the growth and contact of clean, ultra-long carbon nanotubes as well as for the fabrication of non-invasive top tunnel probes. We then present results on normal metal tunneling spectroscopy of carbon nanotube devices of varying length. We measure the exponent of the conductance power law in the density of states as a function of device length over two orders of magnitude and find unexpected evidence of finite size effects in long devices. Next, we present results from the first measurement of the non-equilibrium electron energy distribution function in carbon nanotubes measured via non-equilibrium superconducting tunneling spectroscopy and find little evidence of scattering at low temperatures, which is consistent with a clean, strongly interacting Luttinger liquid. In addition, we discuss two ways we are working to extend this powerful technique. We also present results of superconducting tunneling spectroscopy of a clean carbon nanotube quantum dot. We are able to characterize the energy spectrum of the quantum dot and distinguish between spin singlet and spin triplet shell filling. We observe elastic and inelastic co-tunneling features which are not visible when the probe is made normal by a magnetic field. These co-tunneling rates have important technological implications for carbon nanotubes as single electron transistors. We also observe an energetically forbidden conductance inside the superconducting gap that could be related to inelastic scattering in the carbon nanotube quantum dot. Finally, we present results from the first application of the superconducting tunneling spectroscopy technique to graphene, a two dimensional system. We observe conductance oscillations consistent with Fabry-Perot interference. We also observe a gate dependant pair of subgap peaks, symmetric about bias voltage. We hypothesize that these peaks are due to conductance through bound Andreev states confined to a graphene quantum dot below the superconducting tunnel probe.

To those who dare to think.

Acknowledgements

I can recall standing beside the trampoline with my brother Trent in our backyard. I must have been in about third grade and we were looking at an isolated cloud in the east that was cast in beautiful peach and pink colors. I remember wondering why that cloud was pink in the east when the sun was setting in the west, but it was an idle thought. This isn't one of those corny I-knew-then-what-I wanted-to-do stories. No, what I recall very clearly is that *time* was foremost on my mind. Specifically, the unfathomably long time before I would graduate and not have to go to school anymore. I remember counting the years, which were, of course, denominated in grades: fourth grade, fifth grade, sixth grade, … twelfth grade. Nine long years to freedom! At about the same length of time I'd been on this earth, it's no wonder it seemed like an eternity. I can only imagine the horror in my former self had he known I would voluntarily sign up for another 10 years!

Now, at three times my age then, my time is still measured in years that start in fall and end in summer – but I wouldn't alter my course if I could, because I love what I have learned about who I am and what I can do. However, a Ph.D. is a hard thing and I want to acknowledge the costs and the people who have helped me bear them. I think the only thing I actually regret about the whole thing is that it is necessary to be so far from my family. In particular, I wish I'd been able to see more of my brothers', Trent and Trace's, growth into the good men they have become. And I'd like to thank them and all of my family for not holding my absence against me.

When I think about how I ended up here certain things my parents did keep coming back to me and I remember them fondly. First, and most directly, it was the fact that my parents taught me to work with tools that secured me a position in the Mason research group, because before science could be done, a lab had to be built. It's been a secret joy of mine that after a bachelor in physics and a year of graduate classes, it was my ability to tell a philips from a flat head, that got me a position in the work I wanted to do. And through it all, though many of the tools are different, it has been learning to build things again that I've found truly enjoyable in my time in graduate school. Second, I'm very happy that my mom, Jana, kindled a love of books in me that has never abated. I remember her reading to us at bedtime; spending money she didn't have on books for us (a proud tradition which I continue to this day!) and looking the other way when the change draw never filled up (but my collection of Hardy boys books did). I'm also grateful that I

can't recall having difficulty connecting math to the real world because my Dad, Greg, taught me math *in* the real world. I remember the epiphany when I grasped the idea of area while he was teaching me to use a tape measure and calculate the number of drywall sheets we would need from the store. How many screws should we get? How long will it take us to get there? How much ground beef should we buy? Though I never learned to do the math in my head the way he can, turning problems and questions into math is what a physicist does, and I'm glad I learned it early enough that it feels instinctual. Finally, I don't think I grasped how much of me came from my parents, until mom pointed out that dad and I have the same heroes – only his ride horses and mine fly spaceships (this observation had the added bonus of opening up an entirely new genre for me to devour!). It took the company of some really good people to get through this process and I want to thank you, Mom and Dad, for nourishing the sort of character that attracted those good people.

The first of those people is my beloved fiancée Radhika. When we started this journey, long enough ago that I think in some places we'd be married by common law by now, she was my new optics lab partner (I said *lab partner*) and she's been my partner ever since. If I didn't have you to share this long road with, I'd have turned off long ago. Thank you for continuing to be my Muse, inspiring great things in me. With this chapter that we've written coming to a close, I've never been more excited about the future we will fashion together!

Guy Tal, what can I say? Friend. Business partner. Ninja. You have brought new meaning to, and are forever connected with, the phrases "why not?" and "maybe". I'm not sure we'd have done the crazy things we did, and the crazier things yet to come, had you not proven me wrong and made it all the way across the country on that absurd bike trip of yours (Europe was really just rubbing it in). And King Dave Layton, you left for greener pastures too soon, but you're still a voice in my head and all barbeques and sweet tea are in your honor. Hopefully now that we're both headed to indeterminate places, we'll end up without a major ocean between us.

This work would not have gotten done without some key people I had the privilege of working with. First, I thank Dr. Yung-Fu Chen, with whom I worked closely while he was a postdoc in our lab. Yung-fu is a great friend and his depth of knowledge and willingness to spend time sharing it is truly impressive and much appreciated. We all felt that absence keenly when you moved on and I suspect you will make a great professor someday. Serena Eley, you've been

there since the beginning when the floor of the lab wasn't even poured yet. It has been great sharing an office and ideas with you. I can't decide whether it was more fun in the beginning when we disagreed on everything or in the end when we realized we were both saying the same thing. Nick Bronn, you've been a good friend and always dependable for a proper Manhattan when something is in need of celebration. Someday perhaps I'll take all those hangers out of your attic… Cesar Chialvo, I always feel like we're thinking the same thing, especially when you're cursing in Spanish. Far more rare than the PhD we've all been working towards are people who can always be trusted to say what they mean. Never lose the habit. Clare Yanjing Li, working with you directly over the past year or so as you take over this line of research has been great. I hope I've managed to pass along a few things and I wish you great success. I'd also like to thank Tony Banks. Without the microfab facilities none of this work would be possible, and without Tony, everything falls apart. You keep all the balls in the air most of the time, and keep a sunny disposition even when a few come crashing down. A special thanks to Scott Maclaren, who runs an exceptional AFM laboratory, but more than that you've been a great mentor, adviser, and friend in my many extracurricular ventures. May **TINY** advances bring **S**uper **N**ormal **S**poils! (Or should I say a **B**ig **H**aul?)

I should also mention Mrs. Kaye Pickett and Dr. Thomas Pickett. Of course I had many great teachers and professors before graduate school. These two stand out for their tag-team efforts at a point when I faced a fork in the road. She showed me science in high school and he roped me into physics in my first year of college from what would have likely been a rather lucrative engineering career. I can't thank you enough.

Graduate school is a hard thing. I think you only really know the meaning of that sentence when you've been through it. I've tried to explain it to others when they are starting out and I remember others trying to explain it to me. I'm lucky that through it all I've had a great advisor. Nadya is a great scientist and has a real knack for leading people who don't like to be led which sometimes involves standing back and letting them learn the lessons you've already learned. So in tribute, I'll acknowledge one more thing she said that I could have listened more closely too. As all graduate students do, when I started working I read my advisor's thesis, and in the acknowledgements Nadya says she was glad to have left graduate school with her sanity intact. I must have thought it was a clever, tough-in-cheek opening when I first read it years ago and

maybe it was, but when I reread it recently, it had real resonance. I, too, am glad to leave with my sanity intact.

Table of Contents

List of Tables

List of Figures

List of Abbreviations

AC	Alternating current
ACE	Acetone
AFM	Atomic force microscopy
ALD	Atomic layer deposition
BCS	Bardeen, Cooper, Schrieffer
CNT	Carbon nanotube
CB	Coulomb blockade
DC	Direct current
DOS	Density of states
EBL	Electron beam lithography
IPA	Isopropyl alcohol
MIBK	Methyl isobutyl ketone
MMA	Methyl methacrylate
PMMA	Poly (methyl methacrylate)
SEM	Scanning electron microscopy
SGM	Scanning gate microscopy

Chapter 1
Introduction

Landau's Fermi Liquid theory established that the low energy excitations of an interacting electron system can be approximated as "dressed" non-interacting electrons, i.e. free fermionic quasi-particles of the same charge and spin, but differing mass and velocity. The key insight is that electrons are diffuse enough that interactions are small and can be treated as perturbations on a non-interacting system. To say that the theory is successful would be a criminal understatement, as it explains many properties of the three dimensional, bulk materials that make up most of our world, over a wide temperature range. Yet, as dimensionality is reduced, the assumption that e-e interactions can be treated as perturbations becomes more questionable. With each reduction in dimensionality the space loses, for lack of a better word, "aroundness"[*] – meaning a particle in the space loses an option for avoiding an interaction. The assumption that e-e interactions can be treated as a perturbation fails in one dimension,[1] the only extended space which completely lacks ways around. Like passengers attempting to disembark from an airplane, interactions are geometrically guaranteed to be crucial. In zero dimensions, systems called quantum dots, e-e interactions dominate transport, as the finite energy necessary to add an electron to the dot becomes measureable.

[*] By aroundness, I mean to suggest the options to avoid collision that a car driver has, and a train conductor does not and similarly that a Airplane pilot has and a car driver does not.

Although pondering the various properties and extents of dimensionality has long been the province of mathematicians and philosophers, we are fortunate to live in a time when such seemingly esoteric suppositions can finally be put to a test. For example, dimensional considerations alone led to the prediction of and subsequent experimental support for novel particles called anyons*. [2-4] The theoretical study of low dimensional electron systems has a long history, going back at least to Bethe's exact solution to the spin 1/2 Heisenberg XXZ spin chain[5]. For decades low dimensional problems were regarded as mere toy models, good only for starting on more complicated 3D problems. However, with the emergence of real world low dimensional experimental systems, such as 2D electron gases and graphene (2D) and carbon nanotubes (1D) the area has enjoyed a new prominence over the past 20 years.

For example, Tomonaga,[6] and later Luttinger[7], studied a special class of interacting 1-D electron models, to calculate the low energy behavior of one dimensional systems. Later, Haldane showed that the solutions apply to the low energy excitations of a generic 1D electron gas[8]. It was then that Haldane coined the term Luttinger liquid, in analogy to the Fermi liquid. The quasiparticles of this model are bosonic density wave excitations and many of the predictions made have been recently verified in real world systems; examples include spin charge separation[9-13], noise characteristics[14], and a power law suppression of the DOS at low energy[15,16].

Carbon nanotubes (CNTs) are a quintessential 1D system. CNTs are made of sheets of carbon atoms in a hexagonal lattice, called graphene, rolled into a tubular shape with diameters of about 1 nm and typical lengths of a few tens of microns. The first high strength CNT composite entered the market at least 400 years ago near present day Syria.[17] However, it wasn't until 1991 that Sumio Iijima discovered the existence of CNTs while hunting for fullerenes. The 1D nature of transport in CNTs can be understood by a back-of-the-envelope comparison of approximate quantum energy level spacing, ΔE, in the circumferential direction and the temperature and voltages to which the CNTs are exposed: $\Delta E \sim (h v_f)/(\pi d) \sim 1.3 eV \rightarrow \Delta E / k_b \sim 15,000 K$, where v_f is the Fermi velocity and the diameter, $d \sim 1$ nm is the circumference of a typical CNT. Our measurements are taken at temperatures much less than 15000 K, which, for scale, is nearly

* Anyons are particles whose wave function changes by $e^{i\theta}$ where theta is free to be any angle between the 0 and π of bosons and fermions.

three times the temperature of the sun's surface. Applied bias voltages never exceed 0.1 eV, well below energies where any but the ground state could be occupied. Thus, CNTs clearly act as purely 1D systems for common transport measurements.

Electron transport measurements, in particular tunneling spectroscopy, can give powerful insight into the strength and nature of electron scattering and energy relaxation. The conductance of a tunnel junction is proportional to a convolution of the density of states (DOS) and electron energy distribution, f (E), of the material on either side of the junction. In tunneling spectroscopy the conductance of a junction of two materials, one well understood, and one to be further studied, is measured while multiple parameters are varied. In this way, one can find out how the convolution of the DOS and f (E) in the unknown material depends on the varied parameters. In a common form, the material to be studied is sandwiched between two normal metal contacts which have a featureless DOS and a Fermi distribution. Any observed features in the conductance data are then directly attributable to the spectra of the studied material. For instance, normal metal tunneling spectroscopy has been used to reveal the predicted Luttinger liquid power law dependence of the DOS on voltage and temperature in CNTs.[15,16] The exponent of the power law is predicted to be directly related to the strength of e-e interactions in CNTs.[18] Thus normal metal tunneling spectroscopy can be a powerful tool for studying e-e interactions.

However, other choices of tunnel probes exist and offer significant advantages to normal metals. Superconductors are a particularly useful alternative and have been used in the field of scanning tunneling spectroscopy.[19,20] The sharply peaked Bardeen, Cooper, Schrieffer (BCS) density of states offers two prime advantages. First, the amplitude of the peaks drastically enhances the conductance of weak tunneling processes, making the study of very weak processes easier. Second the sharpness of the peaks allows the determination of the DOS and non-equilibrium f (E) separately via non-equilibrium tunneling spectroscopy.

Understanding of e-e interactions, scattering, and energy relaxation in CNTs and graphene is crucial to understanding low dimensional conduction in general, and is essential if these materials are to be harnessed for technological applications such as single electron transistors and low power electrical interconnects. Tunneling spectroscopy in its various forms is a powerful technique to help bring about this understanding.

1.1 Outline

In this dissertation we present results on various methods of tunneling spectroscopy in CNTs which shed light on e-e interaction in CNTs and low dimensional systems in general. We also apply those methods to two dimensional graphene sheets.

In Chapter 2 we review the fabrication techniques used to make the devices studied here. Some of the techniques are standard in nanofabrication, and some were developed in-house to make the particular device geometries studied here possible. In particular, recipes for the growth and contact of clean, ultra-long CNTs as well as the fabrication of non-invasive top tunnel probes were developed in house. Also, I hope I will be forgiven for pontificating a bit on strategy in the face of fabrication uncertainty and errors.[*] Finally we briefly review the standard measurement circuits we used to acquire the data presented here.

In Chapter 3 we present results on normal metal tunneling spectroscopy of CNT devices of varying length. We measure the exponent of the conductance power law in the DOS as a function of device length over two orders of magnitude. In changing the length of the device, we are tuning several related parameters, including the overall size of the correlated state, the impact of lead capacitance, and the number of defects. We also find unexpected evidence of finite size effects in long devices.

In Chapter 4 we present results from the first measurement of the non-equilibrium electron energy distribution function in CNTs measured via non-equilibrium superconducting tunneling spectroscopy. We find little evidence of scattering at low temperatures, which is consistent with a clean, strongly interacting Luttinger liquid. We then present two ways we are working to extend this powerful technique.

In Chapter 5 we present results of superconducting tunneling spectroscopy of a clean CNT quantum dot. We are able to characterize the energy spectrum of the quantum dot and distinguish between spin singlet and spin triplet shell filling. We observe elastic and inelastic co-tunneling features which are not visible when the probe is made normal by a magnetic field. These co-tunneling rates have important technological implications for CNTs as single electron transistors. When finite bias is applied to the CNT end-to-end, we are able to spectroscopically measure the

[*] Be sure not to miss the Tweezerman's creed.

applied bias. We also observe an energetically forbidden conductance inside the superconducting gap, which is not present without an end-to-end bias.

In Chapter 6 we present results from the first application of the superconducting tunneling spectroscopy technique to graphene, a 2D system. We observe conductance oscillations consistent with Fabry-Perot interference. We also observe a gate dependant pair of subgap peaks, symmetric about bias voltage. We hypothesize that these peaks are due to conductance through bound Andreev states, confined to a graphene quantum dot below the superconducting tunnel probe.

Finally in Chapter 7 our main results are summarized. We also mention possible directions of future research in these areas.

Chapter 2
Fabrication and Measurement of Low Dimensional Devices

2.1 Introduction*

Have you ever seen a ship in a bottle? When I see one I mostly think about the intricate painstaking process of making it. But sometimes it's helpful to forget the how and just be amazed that it can be made. It's the same with the devices studied here. They are conceptually simple, but deceptively difficult to fabricate. Our goal is, typically, to put some current through a CNT and see how it responds. If a carbon nanotube were just a carbon tube that could be held in the hand like a resistor, a thirty second soldering job would do the trick. However, because CNTs are in fact decidedly nano, everything gets … complicated. The CNTs cannot be made or fabricated, they must be grown under specific conditions that change with the weather. Then, they need to be located. Once found, devices can be built on top of them, but things are again complicated by the size/aspect ratio. Many metals have surface tension issues with CNTs and will ball up and make bad contact. Also all evaporated metals are hot on arrival and tend to damage the underlying tube, which cannot dissipate the heat fast enough. So, in this chapter, I will lay out the details of the fabrication process that makes this "ship in the bottle" possible, but along the way don't forget to be amazed that it is.

* They say a picture is worth a thousand words. In my case it appears to be an underestimate. So while perusing the figures in this chapter, know that they have saved you, the reader, much drudgery. If you are very new to fabrication, or just love drudgery, see Appendix I for more detail.

In this chapter I first describe the basic band structure of CNTs. Next I describe the techniques that form the basic building blocks of the fabrication process used to make the devices described in this dissertation. In section 2.4 I will then briefly outline the major steps in the complete fabrication process. For the practitioner I will give some thoughts on fabrication strategy under conditions of high failure rates in section 2.5. And finally in section 2.6 I will outline the standard measurement techniques used to acquire the data presented here.

2.2 Carbon Nanotubes

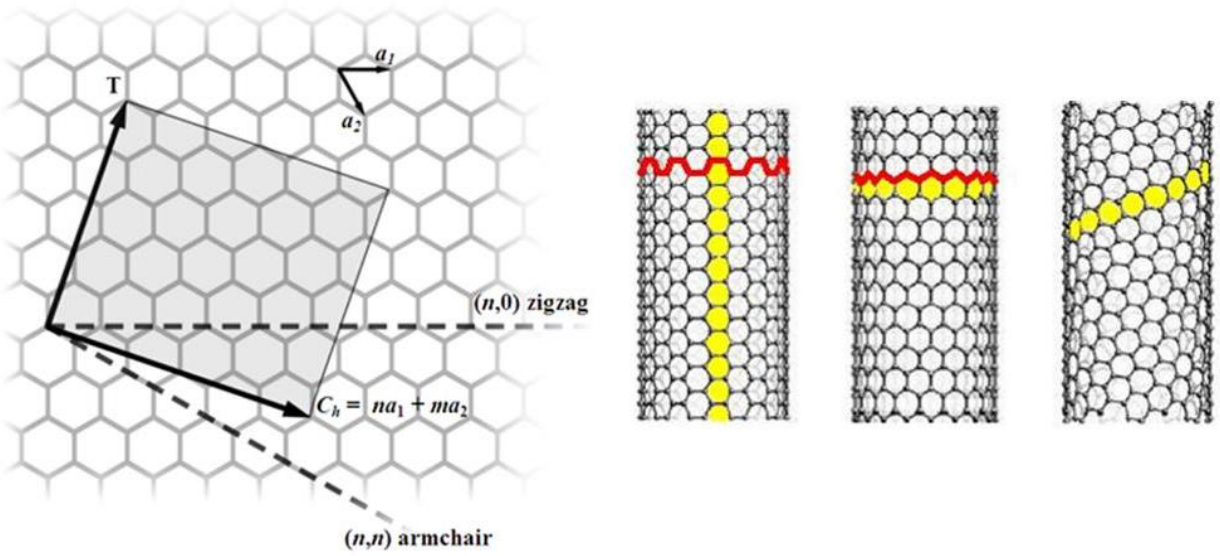

Figure 2-1: On the left, an illustration of the chiral vector, which is the vector perpendicular to the long axis of the CNT, along which the graphene is rolled. Ch=na1+ma2, where a1 and a2 are the lattice vectors. The condition of metallic CNTs is that 2n+m is a multiple of 3. One the right, and illustration of an armchair, zigzag, and chiral carbon nanotube respectively.

CNTs are sheets of carbon atoms in a hexagonal lattice rolled into a tube shape with diameters of about 1 nm and typical lengths of a few tens of microns (right side of Figure 2-1). As mentioned in Chapter 1, the first high strength CNT composite entered the market at least 400 years ago around present day Syria[17]. Made from carbon rich Indian Wootz steel, CNTs grew inside micro-pores within the famous Damascus sabers during the blade treatment procedure. The mechanical properties that made Damascus blades famous are a result of the carbon-carbon bond, natures strongest, and the unique geometry of the molecule.[21]

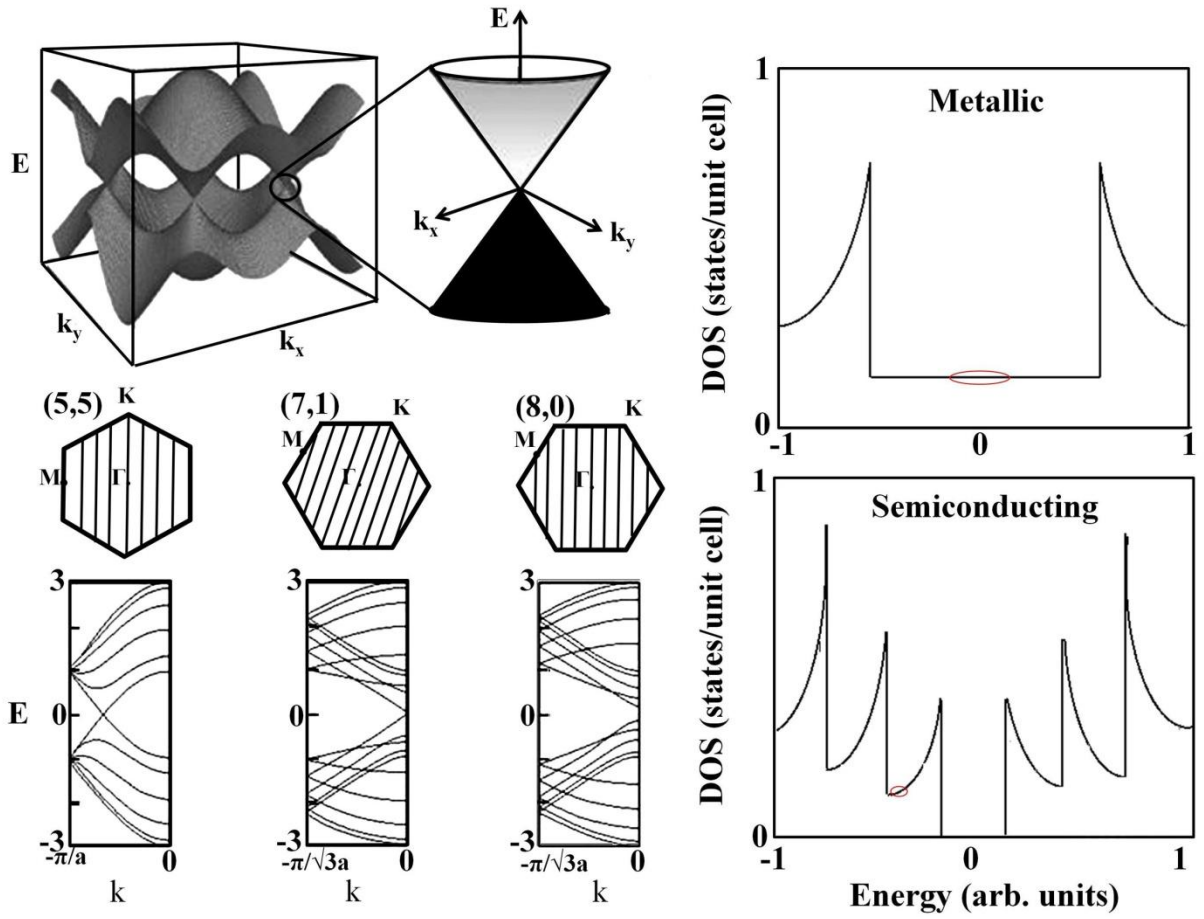

Figure 2-2: On the top left, 2D dispersion relation of graphene. Close up is the Dirac cone around the degenerate K point through which a 1D mode must pass in order for a CNT to be metallic. On the bottom left, dispersion relations for CNT 1D modes with associated Brillion zone slices above. Labels (n,m) of the chiral vector. On the right, schematic of a metallic and semiconducting CNT density of states. In the work presented here we are generally working with metallic CNTs or gating a semiconducting CNT to a region in which it is effectively metallic as indicated by the red circles.

Also remarkable are the unique electrical properties. Depending on how one rolls the graphene sheet, the resulting nanotube can be either metallic or semiconducting[21] (left side of Figure 2-1). The metallic tubes can support current densities much higher than copper and the semiconducting tubes have mobilities of about 100,000 $cm^2\ V^{-1}s^{-1}$ at room temperature, compared to silicon which is less than 1400 $cm^2\ V^{-1}s^{-1}$.[22] Thus CNTs are often held up as the hope for extending Moore's law for transistors down to a few nanometers. While this application

is probably at least a decade way, there are several products in production now, including flat panel displays and high resolution scanning probe microscope tips.

As mentioned in Chapter 1, the small diameter of CNTs leads to quantization along the circumference. This quantization results in quantization of the 2D dispersion relation of graphene (see top left of Figure 2-2) into the 1D modes of CNTs (see Bottom left of Figure 2-2), which are the vertical slices at the quantized values. Metallic CNTs result from having a 1D mode pass though one of the degenerate K points on the graphene dispersion relation.

2.3 Building Blocks of Nano-fabrication

2.3.1 Ebeam Lithography Step

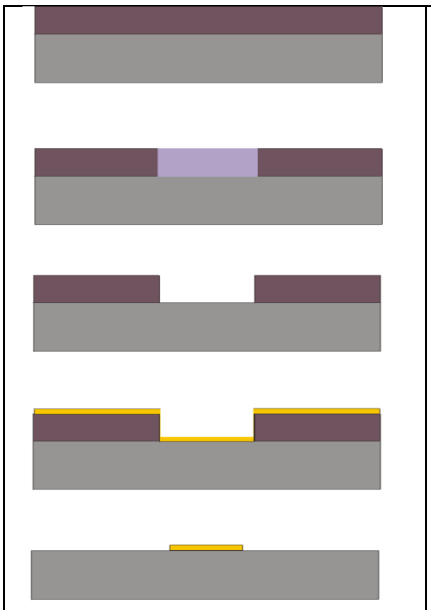

Step 1: An electron-beam sensitive polymer, polymethyl methacrylate (PMMA), is spun on to the Si wafer.

Step 2: An electron beam, from a scanning electron microscope is used to expose the PMMA, breaking the bonds between polymer chains.

Step 3: The exposed PMMA is dissolved way.

Step 4: Metal is evaporated over the entire wafer to the desired thickness.

Step 5: The remaining PMMA is dissolved, removing the unwanted metal.

Figure 2-3: Process diagram of an Electron Beam Lithography (EBL) step.

Electron beam lithography (EBL) is a method of creating devices with features sizes down to the order of nanometers and it is the basic building block of nanofabrication. An EBL step is like painting a sign with stencils. Figure 2-3 illustrates the process. In Steps 1-3, lay down the stencil, to mask off the parts you don't want to paint. In step 4 everything is painted. Finally in step 5 the mask is peeled off to get rid of the unwanted paint, or in our case metal, and leave the intended pattern. By layering metal in this way we can build up interesting devices. (As an

aside, the reverse process is also common in nanofabrication, in which the surface is first painted, the part you want to remain is masked off, and the rest if then etched away. Because these etching processes can cause defects in CNTs these techniques are not use in this work.)

The Paint: Metal Evaporation

Electron Beam Evaporation:

In electron beam evaporation metal in a crucible, called the source, is heated with a collimated, directed electron beam until it is hot enough to emit gaseous metal. A sample is placed above the source to receive the evaporated metal and the entire process occurs in high vacuum, typically 10^{-5} torr or less. Because the metal tends to stick to whatever it hits first and cool instead of rebounding, e-beam evaporation is semi-directional with the source functioning, loosely, as a point source. This is important because it leads to easier liftoff, and allows one to take advantage of shadowing effects in fabrication. Ideally the beam is swept quickly over the entire area of the source such that it becomes one uniform temperature. Usual rates of evaporation are between 1 and 5 angstrom per second. CNTs and Graphene are sensitive to defects caused by heat during evaporation. For this reason rates are kept around 1 Å/s to give heat time to dissipate without taking an unacceptable length of time to evaporate. For the samples discussed in this thesis, all metal was laid down with e-beam evaporation except the superconducting tunnel probes discussed in Chapter 5-Chapter 6, which were thermally evaporated.

Thermal Evaporation

The process of thermal evaporation is very similar to electron beam evaporation except the method of heating the source is different. Here the metal to be deposited is heated by running current through a “boat” which is a piece of metal with a higher melting point then the source. The metal is thus Joule heated until it evaporates. This process is directional for the same reason as electron beam evaporation. Thermal evaporation was used to deposit Pb/In top probes used in Chapters 4 - 6. A piece of carbon tape was used to electrically connect the top of the PMMA mask to ground. Before this step was taken, many devices did not conduct after the Pb evaporation. It is hypothesized that charge was building up on the PMMA mask during evaporation and arcing to the devices below. Pb was chosen as a contact metal because of its

wide superconducting gap and its low melting point, which is thought to make for a more gentle evaporation.

Removing the stencil.

People say liftoff is an art. This is what people say when they can do something but they can't tell you how. It should be the easiest part. Simply place the chip in a beaker of ACE and stand back for a half hour. The ACE will dissolve the PMMA and the unwanted layer of metal will float away like a leaf on the wind. This is called lift off and with Chromium it really is that simple. After about 2 seconds in the ACE a wave roles over the mirror Cr surface, crumpling it like a giant earthquake rippling through the earth's surface. Fifteen minutes later the Cr can be peacefully rinsed away. With two angstroms of iron, things are similarly copacetic. Everything else can be a horrible pain. For some insight into what techniques do and do not work for these devices see Appendix I

2.3.2 Growth and Location

In one sense carbon nanotubes are surprisingly easy to grow. They can be fabricated via several different mechanisms, such as arc discharge,[23,24] laser ablation[25], and chemical vapor deposition.[26] All three methods rely on combing a source of heat, a source of carbon and a catalyst. In chemical vapor deposition (CVD) a wafer is exposed to one or more volatile precursors, which react to deposit a desired substance on the surface. In the CVD CNT growth method, hydrogen and methane are flown past a silicon substrate covered with Fe catalyst in a tube furnace heated to ~900 C. CVD growth offers several important advantages for our purposes. First, the tubes grow directly on the substrate, which eliminates a deposition step necessary in arc discharge. Second, they tend to be clean, that is, relatively free of amorphous carbon. Finally CVD allows for ultra-long, semi-directional CNT growth, which is crucial for some of the devices studied here.

Typically CNTs are grown at 900C in 1000 sccm of methane and 100 sccm of hydrogen for 10 minutes. This results in CNTs on the order of ten microns long. In the growth of CNTs we have precious few control knobs. In fact, the main obstacle barring CNTs from commercialization in electronics is the inability to controllably grow the correct type of CNT (semiconducting or metallic) in a particular place and orientation. One can roughly control the

diameter of the CNTs because of the observed correlation between CNT and catalyst particle diameter[27-29]. CNTs larger than a few nm in diameter tend to be multi-walled. Thus I use 0.2 nm of evaporated Fe as a catalyst, which results in a relatively tight distribution of tube diameters around 1 nm, ranging as low as 0.5 nm and as high as 2 nm. Other variables that have been shown to affect diameter are carbon feeding rate,[30] type of carbon source,[31-33] and growth temperature.[34] The temperature dependence is particularly interesting, since it was found that the diameter of a single tube could be varied by changing the temperature sharply during growth, with higher temperature leading to smaller diameter. The other important controllable variables are the growth time, the overall flow of gases, and the ratio of hydrogen to methane. In general, holding other variables constant, more overall flow will result in cleaner growths with lower tube density. Similarly, higher ratios of hydrogen to methane will result in cleaner growths with lower tube density.

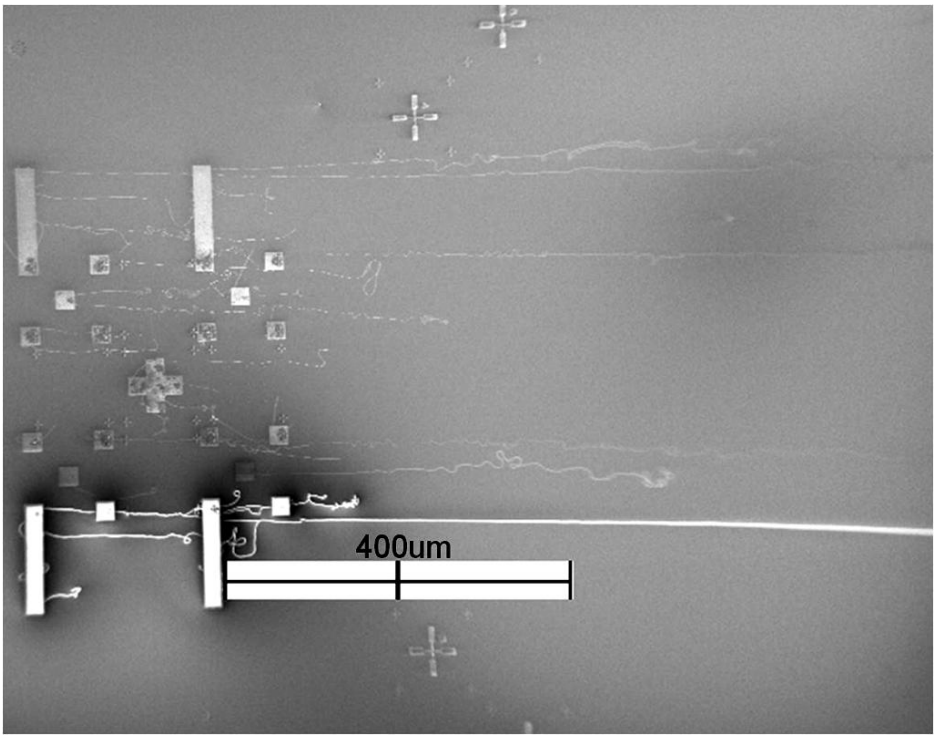

Figure 2-4: SEM of ultra-long CNT growth with length between 300 and 5000 nm, with the upper limit set by the end of the substrate.

There is a well known (to the initiated), but un-discussed problem with CVD CNT growth. After my first successful winter growing CNTs I was warned that many time CNTs will not grow

in the summer. I scoffed at the idea. Why would CNTs grown in a CVD at 950 K in methane and hydrogen, sitting an air-conditioned building, care if it was a little warm and humid outside? A knowing smile was my answer. Alas, they do care, very much. I didn't have a decent growth until November! Eventually, during my next barren summer, I developed an annealing procedure that has allowed growth year round, on the theory that humidity was the problem. Before growth, the sample(s) are heated at 250C overnight in 200 sccm Ar. The temperature is then ramped to 700C in 100 sccm Ar and 60 sccm H_2 and baked for 10 min. Then the temperature is ramped to the growth temperature. The fact that this annealing procedure helps, indicates that the problem is related to humidity and oxidation of the catalyst particles.

There are several known methods for growth of ultra-long aligned CNT,[35-37] all of which rely on decreasing the Van der Waal's interaction between the CNT and the substrate. Since ultra-long CNTs are crucial for the work discussed in Chapter 3, I developed a variant of Hong's low flow method[36] in which the sample was placed in a small diameter quartz tube, which was calculated to produce laminar flow of gasses over the chip. It was believed that this stable laminar flow allowed CNTs to remain floating over the surface during growth. However, I found that laminar flow was not crucial and had more success using similar gas flows − 100 sccm methane and 60 sccm hydrogen − but deliberately inducing mild turbulent flow by using an open boat, the calculated Reynolds number of which is far outside the laminar flow regime (see Figure 2-7). The growth temperature is 950 C. This recipe results in CNTs from 200 to 5000 microns long, the length being limited by growth time and the size of the substrate. The recipe results in tubes between 0.5 and 2.5 nm in diameter, with the most frequent diameter 1.4 nm. Tubes below 2nm in diameter are generally single walled. After growth I determine the location of the CNTs with respect to the alignment marks using scanning electron microscopy.

2.3.3 Atomic Layer Deposition

Atomic layer Deposition (ALD) is a self-limiting process that deposits conformal monolayers of materials onto substrates of varying compositions. ALD is similar to chemical vapor deposition (CVD), except that the ALD reaction breaks the CVD reaction into two half-reactions. First a precursor gas is exposed to the substrate (in our case, the first precursor is water). A mono layer of precursor reacts with and sticks to the substrate, while the rest is pumped away. Then the second precursor (TriMethylAluminum) is exposed to the wafer. The

ensuing chemical reaction (which creates a single layer of AlO_x) is limited by the amount of the first precursor on the substrate, thus the remaining material is a monolayer. The technique produces very thin films with very few pinholes. Both of these traits are essential to the controlled fabrication of the tunneling probes discussed below. It is also important that the ALD process happens at relatively low temperatures, 180 C. Also it is possible that this very thin, ~1 nm, insulating layer between the CNT and the evaporated contacts, provides a channel for heat conduction away from the CNT during evaporation. This is thought to reduce damage to underlying CNTs or Graphene. See Appendix I for recipe.

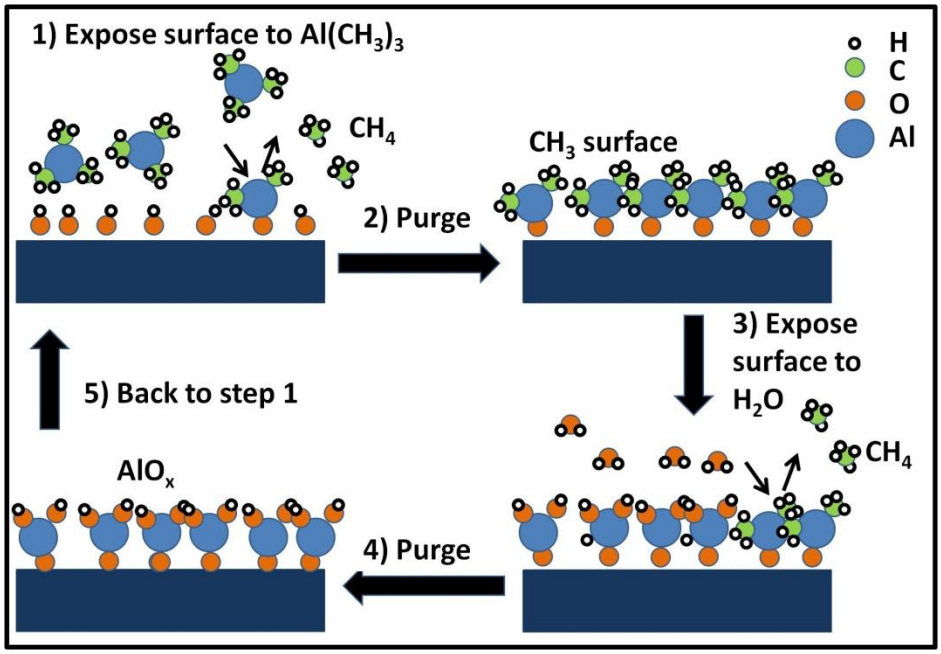

Figure 2-5: ALD is a set of two separate self limiting surface reactions. The first precursor is TriMethylAluminum. The second is water. In the above diagram, process is read clockwise, with resulting Aluminum Oxide layer in the lower left corner.

2.4 The Fabrication Process

In Figure 2-6, one can see the major fabrication steps required to birth the devices discussed. Figure 2-7 is a pictorial map of the fabrication process, showing a sample in different stages of development: just after growth, just after electrical contact, and just after laying down a middle tunnel probe.

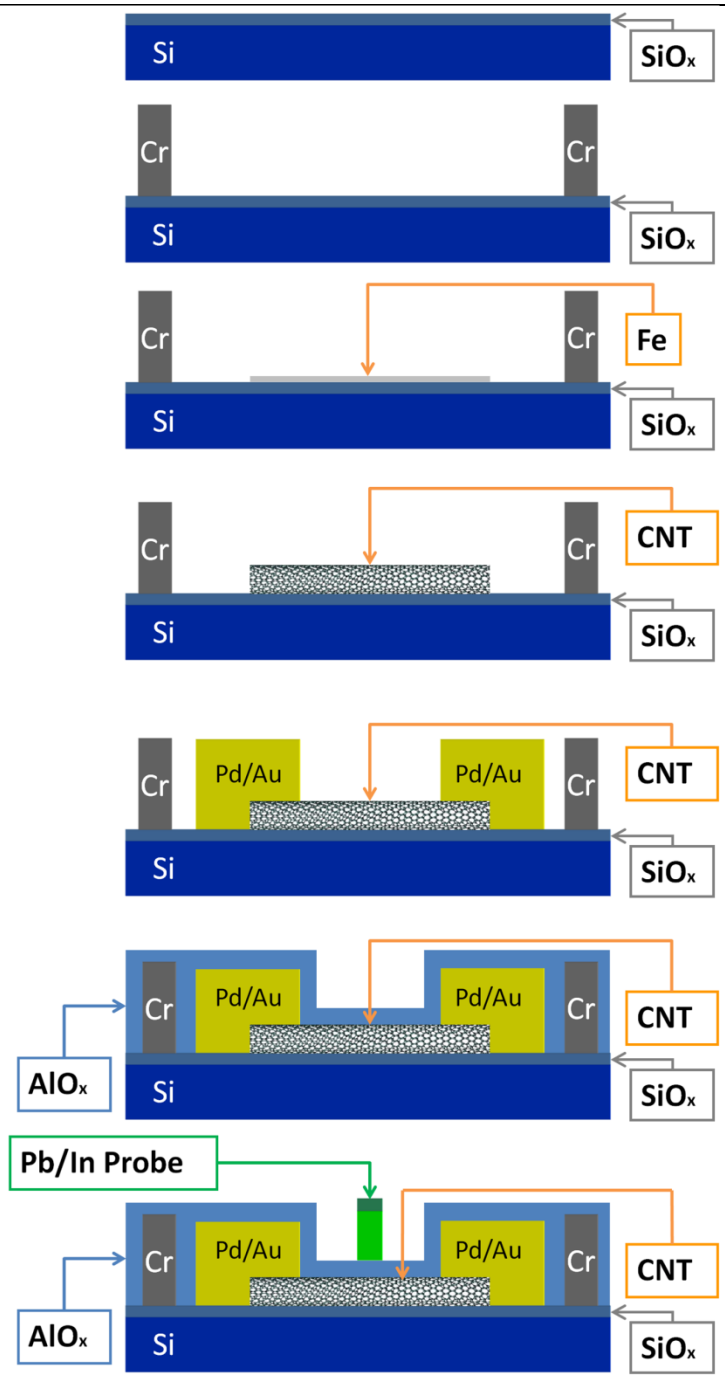

Step 0: Doped Si wafer is a universal back gate in the finished device. Device is insulated from back gate by thermally grown oxide (typically 1µm thick)

Step 1: EBL 60 nm thick Cr alignment marks

Step 2: EBL 2 angstrom thick Fe catalyst pads near the alignment marks

Step 3: wafer placed in a chemical vapor deposition oven for CNT growth. After growth CNTs located relative to alignment marks by SEM

Step 4: A custom CAD pattern of electrical contacts is drafted. Then EBL 5 nm Pd / 30 nm Au End Contact Pads.

Step 5: Apply ~1.2 nm Al_2O_3 via Atomic Layer Deposition to the entire sample, for tunnel probe insulating layer.

Step 6: EBL 200 nm Pb / 30 nm In top tunnel probe. Finally the wafer is glued to a sample carrier with silver paint and the device is electrically connected to the carrier by wedge bonding.

Figure 2-6: Process Map of the major fabrication processes required to produce a three probe superconducting tunneling spectroscopy device. For details on EBL see section 2.3.1.

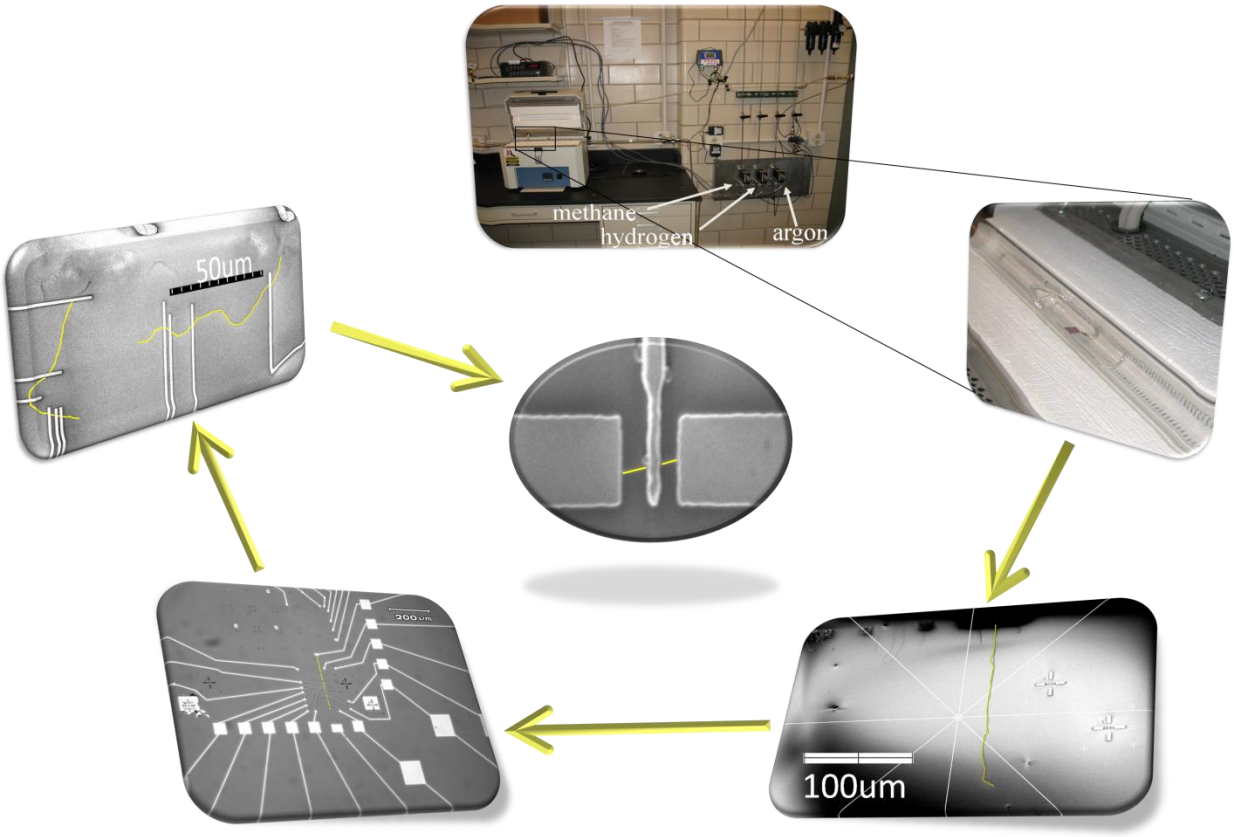

Figure 2-7: Pictorial map of fabrication process. From top to bottom: CVD System, close-up of Chip in oven, SEM image of CNT and alignment marks, SEM of contacted CNT, Close up SEM of same device, Finally a close up image a device with an added top tunneling probe. CNTs are false colored yellow in the above SEM images.

2.5 Strategery

Moderator: I would ask each candidate to sum up in a single word the best argument for his candidacy.

George W. (Will Ferrell): Strategery.

"God grant me the serenity to accept the things I cannot change; the courage to change the things I can; and the wisdom to know the difference."

-Reinhold Niebuhr

There are very few problems in fabrication that are fundamentally unsolvable, however when it is you against the process, the finite nature or your time makes everything a question of economics: how best to budget this finite resource to accomplish the task before you. Some investments of your time will return more than others, and it pays to think about these issues to maximize your return.

The first thing to consider is that small chances of error compound quickly when one is subject to them repeatedly. A poignant example that one hopes to avoid personally occurs in the emergency room. The doctors and nurses in emergency rooms are highly trained professionals operating under extreme pressure and amongst all the actions they perform to keep a person alive each day they have a minuscule 2% error rate. Unfortunately the average emergency room patient requires the performance of 178 separate actions each day. Thus, on average, each patient is the victim of two errors per day.[38] So at first pass, it pays to eliminate any unnecessary steps or processes. Don't roll the dice if you don't have to.

Some clarification of terms: At the largest scale, by "wafer", we mean a larger piece of silicone which might contain several or many "samples" or "chips" which will be broken apart sometime before measurement. A "sample" or chip" is a single piece of silicon which might contain a few or many devices to be measured, which can be mounted in a cryostat. Device means a single thing to be measured; usually this consists of one CNT or piece of graphene with two or more contacts.

There are two basic types of failure: global (wafer or chip wide) failure and local (device level) failure. Global failure is almost always a preventable error, such as an equipment malfunction and cannot generally be overcome by brute force production of chips for two reasons. First, chips are the unit of production and their loss is expensive time wise. Second these errors usually indicate a problem in the lithography process that will repeat until it is fixed, for example contaminated metal, old resist, broken shutter etc. These types of errors must be confronted head on and fixed.

Local failures can also be a preventable error, such as a tweezer scratch. These types of errors should be minimized but are less costly than chip wide failures, since you only lose one or a few devices at a time. However most local failures are probably at best random problems that can be optimized but not fixed. An example is high resistance contacts. On one chip with 72 identical

devices, meaning the devices were processed in parallel with the same contact geometry, but with different tubes, 72% had a resistance between 6 and 100 KOHMs while 22% had a resistance greater than 100 MOhm, with only 6% of devices in between. These are the sorts of problems that Intel unleashes a fleet of process engineers on. Attack them at your own peril. This type of error is best overcome by brute force. It is generally cheap in terms of time to increase the number of devices on a chip since most operations are performed at a chip level on all devices simultaneously. A similar idea can be applied to wafer scale and batch processing. In fact, major increase in productivity came when I introduced wafer stage processing into my procedure.[*] Generally samples are wafer stage processed until after catalyst evaporation and then batch processed during CNT growth. If equipment failure is at all common it is best to limit batch and wafer scale fabrication to the early stages when you have not invested much in each chip. This is an unseen cost of living with high equipment failure rates. Sample production could be drastically increased if batch/wafer processing remained practical in the later stages of production.

When a process cannot be eliminated and the problem cannot be solved by mass production, the only route left is to work to lower the error rate to acceptable levels, which are lower than one might think. A prime example of this type or problem is the most frequent operation in sample fabrication: sample transfer via tweezers. If one wants sample transfer to add only a 2% chance of error over the fabrication process and there are 20 required transfers, the error rate per transfer must be reduced to 0.1%, meaning only one fumbled chip in a thousand. Thus the Tweezerman's creed:

> The Tweezerman's creed:
>
> These are my Tweezers. There are many like them, but these are mine. My tweezers are my best friend. They are my life. I must master them as I master my life. My tweezers, without me, are useless. Without my tweezers, I am useless. I must grasp my tweezers true. I must transfer more smoothly than my enemy, time, who is trying to kill me. I must beat him before he beats me.

[*] Many people underestimate the advantages of wafer stage processing, so as a first order estimate, let's assume one wants to make 36 samples. 6 steps x 36 samples = 216 steps. One the other hand if the samples are wafer stage processed for the first 3 steps, the total steps required is 3+3x36=111, cutting fabrication time in half. This does however put many more devices at risk to global failure mechanisms.

> My tweezers and I know that what counts in this war is not the number of samples we transfer, nor the speed at which we move. We know that it is the drops and scratches that count.
>
> My tweezers are human, even as I, because they are my life. Thus, I will learn them as brothers. I will learn their weaknesses, and their strengths. I will keep my tweezers clean and ready, even as I am clean and ready. We will become part of each other.
>
> Before God I swear this creed. My tweezers and I are the defenders of my efforts. We are the masters of our destiny. We are the saviors of my life. So be it, until victory is mine and there is no enemy, but publication.

For the practitioner: An old saying, which is actually an old marketing slogan says “God created men equal, Col. Colt made them equal..." referring to the way colt revolvers drastically decreased the difference between the expert and the novice. For the Colt of Tweezers see Appendix I.

There is a second significant preventable danger to samples that occurs primarily during sample movement: Static discharge. CNT and graphene devices are very sensitive to static and will vaporize from shocks you never even feel. For this reason an antistatic regimen is essential. In most cases it is enough to ground yourself, your tweezers, and whatever your sample is sitting in or on before you move the sample. In winter however, I always carry around a polonium anti-static source. This is an alpha particle source primarily used by people who work with film that ionizes the air and allows static electricity to discharge through the air slowly. Other antistatic measure that pay: when handling the sample limit yourself to cotton, short sleeved shirts, don’t wear shoes, wear a grounding strap, and use metal chairs or stools.

2.6 Measurement Setup

Depending on the temperatures that must be accessed, samples are measured inside a helium dunker probe that has a base temperature of 4 Kelvin, or an Oxford He^3 cryostat with a base temperature of 0.25 Kelvin. The conductance measurements are taken via standard lockin technique in which a small low frequency AC signal, $V_{excitation}$, is used to measure the differential conductance of the sample at the applied DC bias voltage, V_b. Lockin measurements are good

when low signal, low noise measurements are required. Since the conductance is only measured at the excitation frequency (and higher harmonics), noise at other frequencies is filtered out. The excitation frequency should be low, so as to sample the DC response of the measured device, and as free of noise as possible at harmonic frequencies. As depicted in Figure 2-8, for end-to-end measurements a 0.1mV, 17.137Hz excitation voltage from the lockin (SR830) was added to a DC bias Voltage from a voltage source (Keithley 2400) by either a simple BNC T, or with the sum box discussed below. The $V_{excitation}$ is generally divided by 10,000 (meaning the lockin output is 1V) and the bias voltage is divided by 100. The total voltage is then applied to one end of the sample. The resultant current is routed through an Ithaco current amplifier, then back into the lockin for readout. The back gate voltage is sourced by a Kiethley 2400.

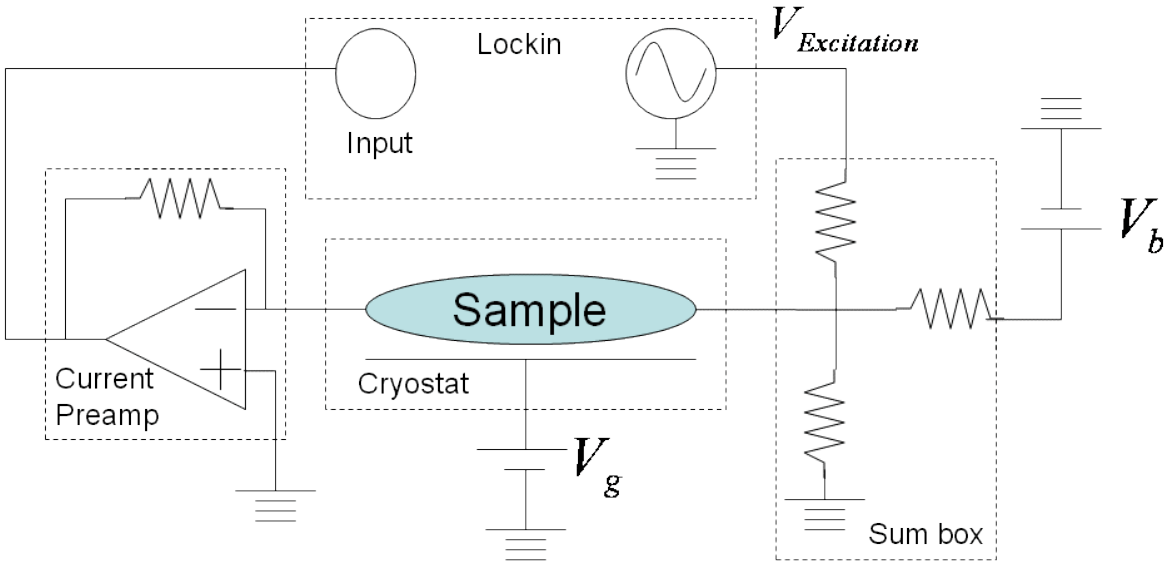

Figure 2-8: Measurement Circuit for two-probe, end-to-end conductance measurements. $V_{excitation}$ is the AC excitation voltage. V_b is the DC bias voltage. V_g is the backgate voltage.

As seen in the circuit diagram in Figure 2-9, measurements through the tunneling probe on three probe devices are done with a similar circuit as shown in Figure 2-8, only the source is applied to the middle tunnel probe, instead of to the end. Also a smaller excitation voltage of 0.025 mV is generally used. In the non equilibrium measurements discussed in Chapter 4 - Chapter 6 an end-to-end bias voltage is applied to the device, while still measuring conductance through the tunnel probe. This configuration results in many potential ground loop issues. For

this reason the end-to-end DC bias voltage was provided by a floating 9V battery and a variable voltage divider, instead of a grounded powered source (such as a Keithley 2400). Also, $V_{excitation}$ and the tunnel probe bias are added using the sumbox seen in Figure 2-10. This box's function is to isolate the output signal from the ground of the input signal. The ground of the entire circuit is then defined by the drain.

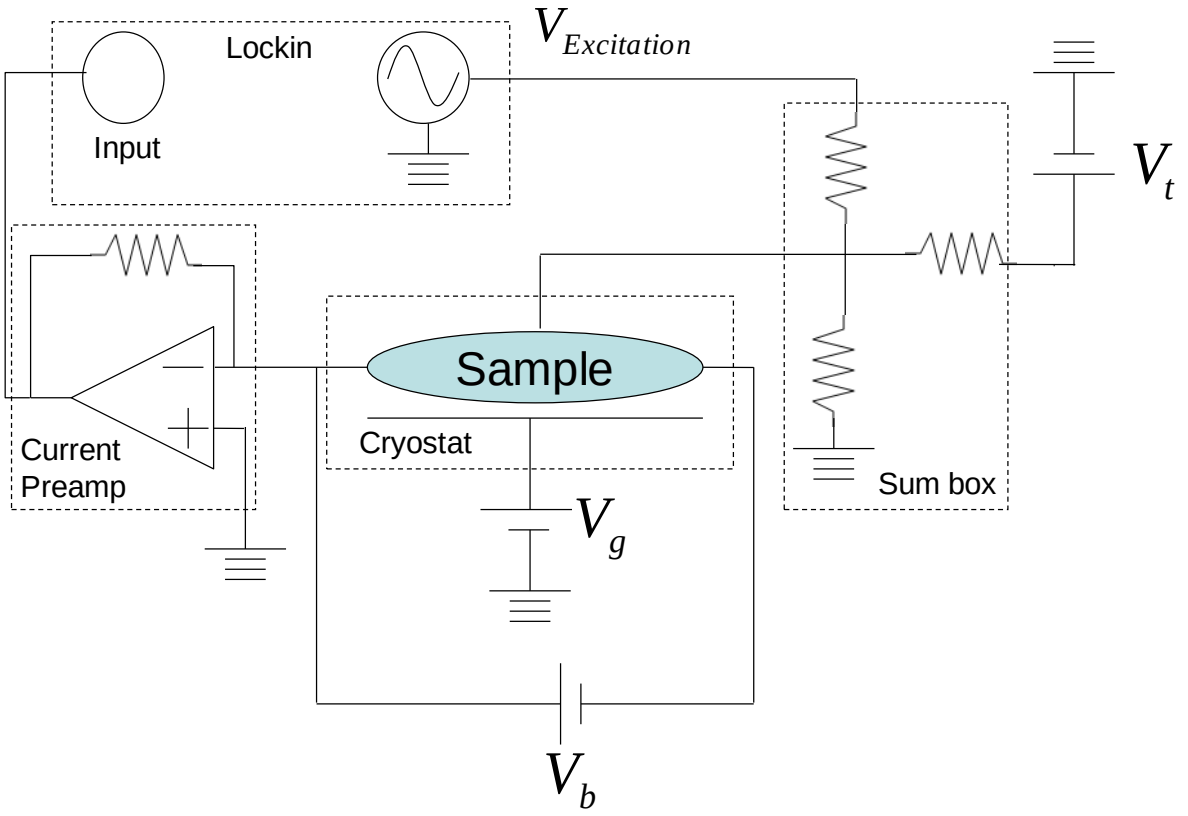

Figure 2-9: Measurement circuit used in Chapter 5 - Chapter 6 for three probe non-equilibrium measurements. $V_{excitation}$ is the AC excitation voltage. V_b is the DC end-to-end bias voltage. V_g is the backgate voltage. V_t is the DC tunnel probe voltage.

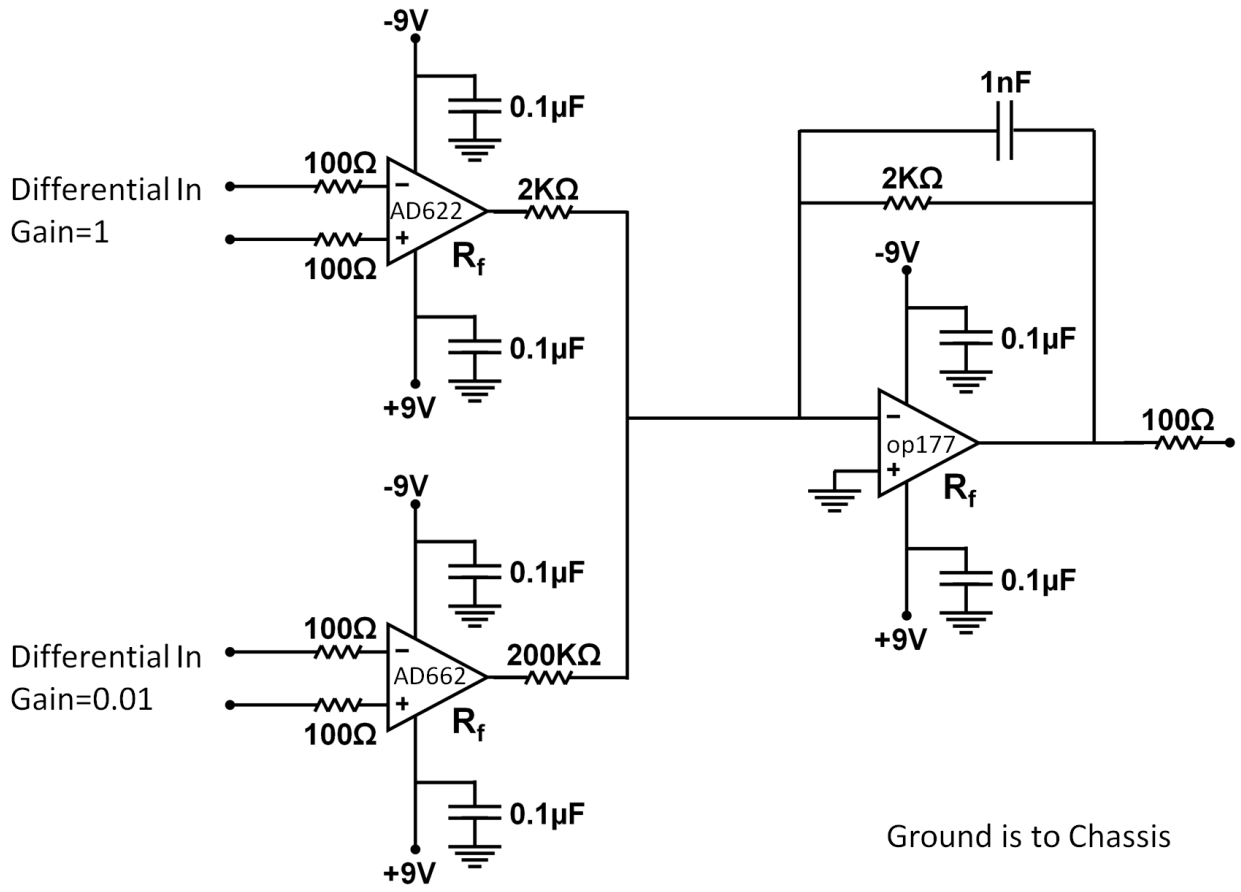

Figure 2-10: Circuit diagram for a floating differential sumbox used to isolate the measurement circuit from the grounds of the Voltage sources used. Circuit design is from Norman O Birge's laboratory at Michigan State University. The key to a well functioning sumbox is to match the 0.1 µF capacitors well.

Chapter 3
Normal Metal Tunneling Spectroscopy of CNTs: Dependence of Zero Bias Anomaly on CNT Length

3.1 Introduction

Two-probe normal metal tunneling spectroscopy of CNTs has a rich history. Conductance measurements through two normal metal, high contact resistance, end probes have revealed interesting phenomena such as Coulomb blockade,[39,40] Fabry Perot oscillations,[41,42] and zero bias anomaly (ZBA).[15,16] In particular, the ZBA is predicted to be directly related to the strength of electron-electron interaction in CNTs. Though many of these results are ten years old, the low temperature length dependence remains little studied. Here we add to the CNT ZBA body of work by measuring ZBAs in devices of varying length. The main reason this remains unstudied is that the properties of CNT devices vary with tube diameter and chirality, which makes comparisons between devices of different lengths difficult. Comparison between different length devices is also made difficult by the devices' highly variable contact resistances. In the work to be discussed in this chapter, we have attempted to circumvent some of these difficulties by fabricating many devices in parallel on the same long CNT (see Figure 3-2). Measuring many devices on the same long CNT removes variability in CNT properties and makes contact resistance more uniform. Similar devices have been fabricated by other groups, but no low temperature measurements were performed[43]

Such low temperature measurements on devices of varying length could be particularly interesting in the ZBA regime which, according to some theories, is due to Luttinger Liquid phenomena. In a Luttinger liquid the low energy excitations are bosonic density waves, or plasmons. Here the ZBA is predicted to be a power law, the exponent of which is related to the strength of electron-electron interaction on the CNT by the Luttinger liquid theory. As discussed below, the power law exponent, alpha, is a function of *g*, which is a measure of the strength of e-e interactions. Thus, by measuring the dependence of alpha on the length of the device, we can infer the dependence of the e-e interactions on the length. Changing the length of the device, may tune several related parameters, including the overall size of the correlated state, the impact of lead capacitance, and the number of defects. These parameters are thought to affect the Luttinger liquid state, which in turn affects the observable conductance power law as a function of temperature and bias voltage. We find that the trend in the dependence of alpha on length is consistent with a naïve Luttinger liquid prediction, but that the intrusion of zero dimensional effects makes any stronger statement difficult. We also observe a dependence of alpha on gate voltage which is expected in the intermediate regime between Coulomb blockade and Luttinger liquid and consistent with evidence of a defect density on the order of a μm.

In this chapter I will first briefly discuss the fabrication process and measurement setup, the details of which were discussed in Chapter 2. I will then discuss measurement regime considerations, give brief overview of Luttinger liquids, and sketch the source of the power law suppression of the density of states. I will also present a naive Luttinger prediction of alpha's dependence on length, followed by comparison to the measured dependence of alpha on length. Finally, I will present three pieces of data that suggest the presence of backscattering defects in the CNT, which effect the measurement of alpha. I will then conclude and present future directions of research in this area.

3.2 Sample Fabrication

Samples were fabricated as described in section 2.4 through the fourth step in Figure 2-6. They consist of a single long CNT with many contacts fabricated varying distances apart, as shown in Figure 3-1 and Figure 3-2. Ultra-long tube growth was a new development when I began this effort. I verified the results of two[35,36] of three[37] published methods of ultra-long tube growth, and developed a variant of one of the methods to fit our needs (See section 2.3.2). These

ultra-long CNTs are long enough that one could easily put 20-50 devices on a single CNT. More typically I would put 8-10 devices of varying length on two different CNT's on the same substrate, since I was limited by the 32 leads on our dunker probe. Figure 3-2 is and AFM image of one such device. Note the astonishing fact that the 1nm thick CNT is visible through the ~ 40 nm thick contact pads. The measured height of these ridges on the contact pad is typically only a bit smaller then the bare tube on substrate. This implies that the CNT is physically more or less intact under the metal. The carbon atoms that make up the tube would be much thinner, say an angstrom or two, were they not still in a tube shape. This is somewhat interesting since evaporated contacts are known to electrically cut CNTs.[44,45] The implication is that relatively minor distortions of the CNT, such as lattice defects or possibly compression of the CNT, that leave the overall tube shape intact are enough to cut electrical contact between the two sides; this reinforces the idea of waveguide-like conduction through CNTs.

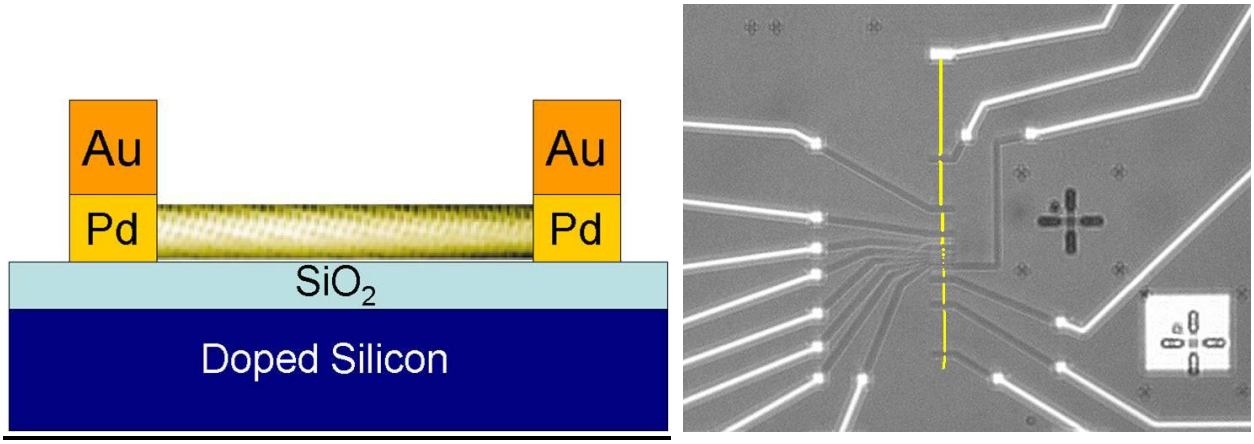

Figure 3-1: On the left, geometry of basic CNT device. On the right, optical image of multiple contacts on a single ultra-long CNT. CNT is represented by the yellow line and is ~280 μm long.

Measurement setup:

Two-terminal conductance measurements were performed inside a helium dunker probe that has a base temperature of 4 K, using standard lockin techniques. For the measurement circuit and details, see Figure 2-8. The back gate voltage and the DC Bias voltage are sourced by Kiethley 2400s. A 0.1mV excitation voltage is sourced by a Stanford lock-in at 17.137Hz. The AC excitation is voltage added to the DC bias voltage and applied to one side of the device. The

return signal is routed though an Ithaco current amplifier, and then input to the lock-in to measure the conductance.

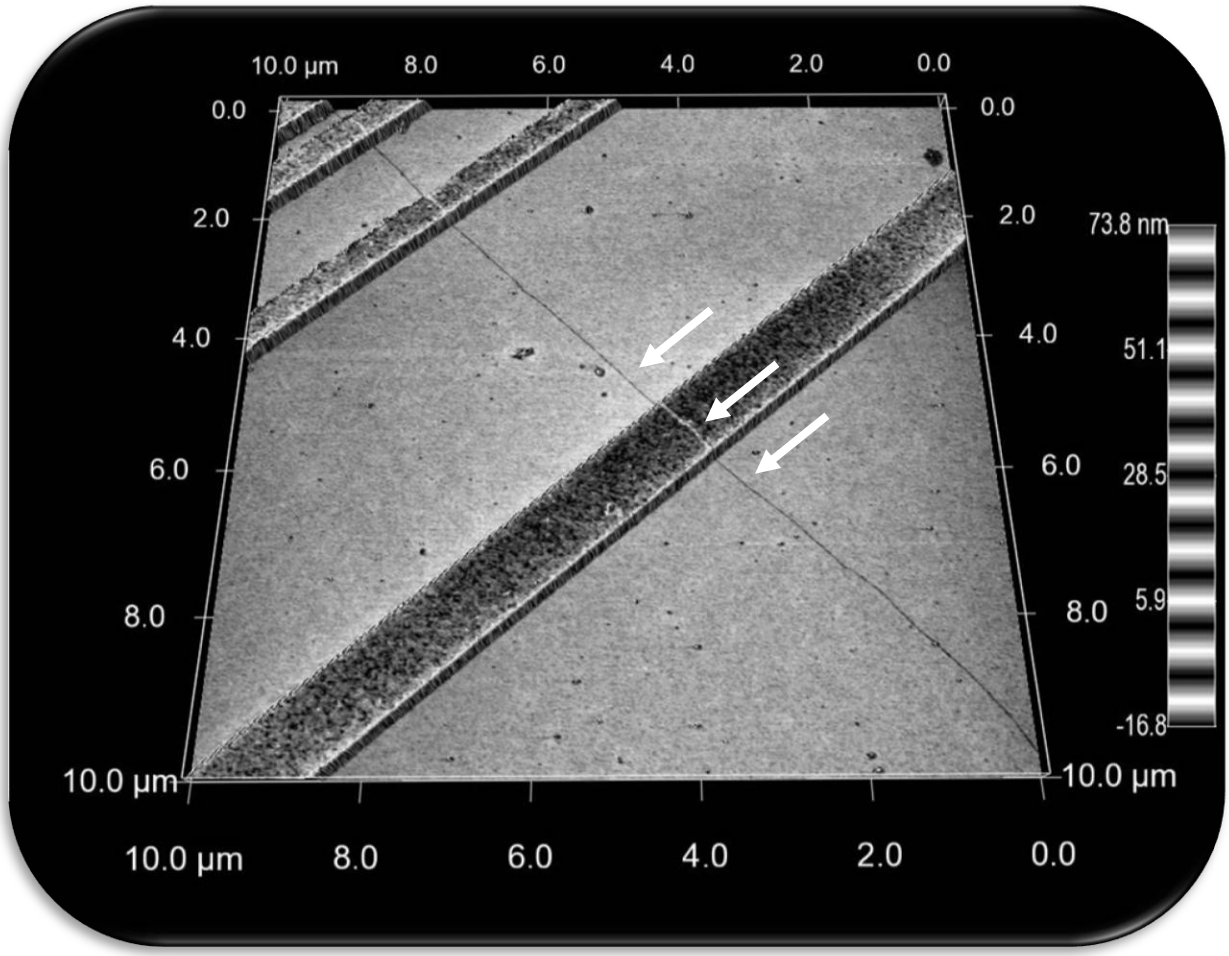

Figure 3-2: A 3-d rendered AFM image of three devices of varying lengths on a single ultra-long CNT. The 1nm thick CNT is visible through the ~40nm thick contact pads see white arrows.

3.3 Measurement Regime Considerations

For these measurements, we want to avoid complications from 0D confinement effects such as Coulomb blockade. Coulomb blockade refers to the conductance steps seen at low bias as one tunes through the discrete energy levels associated with confinement along the length of the CNT. Thus we want the energy with which we are probing the system, $eV+k_bT$, to be larger than the "particle in a box" level spacing: $\Delta E = h v_f / L < eV + k_bT$. For example, in a one micron CNT $\Delta E \approx 1$ meV, so we must use temperatures above $1\text{meV}/k_b \sim 10\text{K}$ or bias voltages above 1mV.

The AC excitation voltage must be smaller still, so that the oscillation doesn't average over the behavior of interest. In addition, we cannot measure at very high energy scales because the low energy approximation at the heart of Luttinger Liquid calculations fails in this regime. Empirically, this failure appears to happen around k_bT~100K and V~10mV. Thus in both temperature and bias sweeps, we are limited to fitting the power law over less than a single decade. Apart from the differences between devices, this is a major cause for the spread in reported values of alpha.

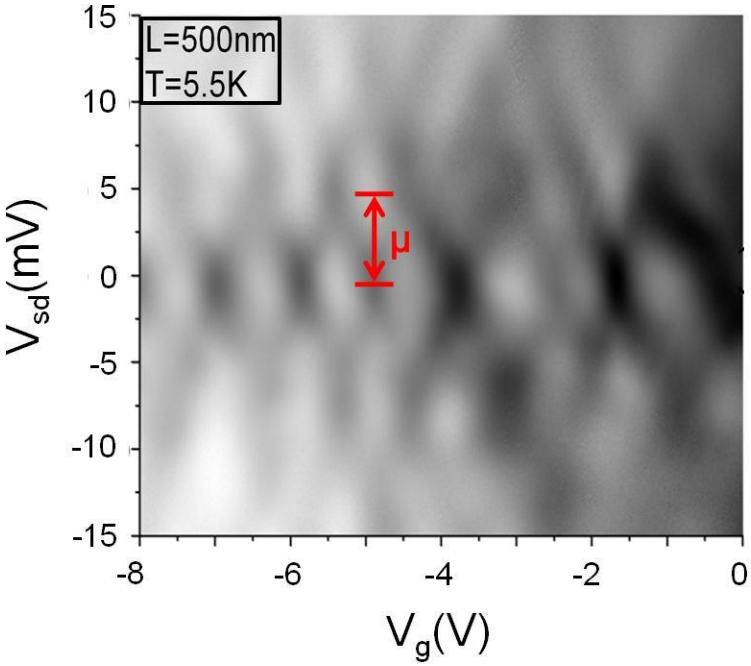

Figure 3-3: Fabry Perot interference pattern as observed in a 500nm long CNT at 5.5 Kelvin indicating coherent transport across the length of the device. μ is the change in bias voltage between the conductance maxima and minima and can be related to the size of the interference cavity.

Before getting to the correct energy regime, let us see what things look like when the system is too cold, and what we can learn from it. For example, Figure 3-3 shows conductance of a very clean CNT device at 5.5 K. The vertical axis is the bias from source to drain contact. The horizontal axis is the voltage applied to the back gate. A clear Fabry Perot pattern is seen, indicating we are in a regime in which $\Delta E = hv_f / L > eV + k_bT$, which is indeed the case for a 500 nm CNT at 5.5K. In Fabry Perot interference, the CNT acts as a coherent wave guide and the electron wave-function interferes between the two metal contacts, like light between two

semi-transparent mirrors. The phenomenon occurs at low temperatures when the contacts to the CNT are very low resistance. So, oscillatory conductance phenomena are a good clue that one is approaching or in a temperature regime in which dot type effects begin to show themselves. One can find the implied channel length from the Fabry Perot wavelength by setting the round trip phase change, $L\mu/\hbar v_f$, equal to 2π, where μ is the distance between a conductance peak and valley in the bias direction times e, as indicated in Figure 3-3. We find that $L = hv_f/2\mu \sim 400nm$. This is consistent with the physical device length of 500 nm. Measurement in this regime also allows a rough measurement of the coherence length in CNTs. Since Fabry-Perot interference is coherent interference across the entire device, its observation is proof that the coherence length in the CNT is at least as long as the device. I have observed this phenomenon in lengths of up to 0.75 um at 4K.

3.4 Luttinger liquid theory's zero bias anomaly predictions

Electron-electron interactions are thought to be particularly strong in CNTs because electrons are effectively confined to a line. The Luttinger liquid theory is a theory of the low energy excitations of such an arrangement. One can gain a lot of insight into the Luttinger liquid by considering a classical equivalent. Imagine a host of like-charged marbles confined to a pipe (left of Figure 3-4). Dump the marbles in there and once things settle down, that is at low energy, one can approximate the system as series of coupled harmonic oscillators, the excitations of which are density waves. In Luttinger liquid theory this approximation is made when we linearize the dispersion relation[46] (right of Figure 3-4). In this theory the strength of interactions, or the stiffness of the oscillators, is measured by the parameter g.

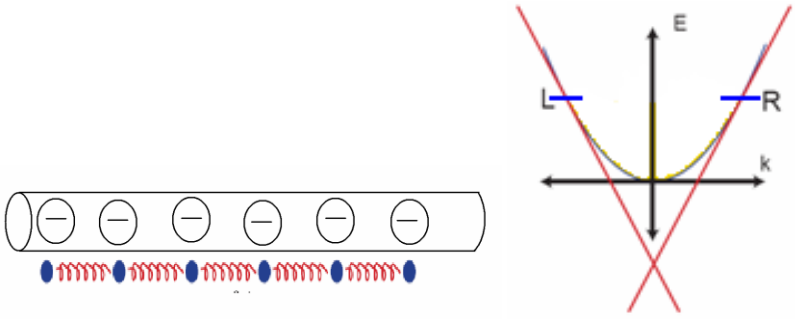

Figure 3-4: On left, a classical analog of a Luttinger liquid. On the right, the linearized CNT dispersion relation.

Perhaps the most easily observable, novel property of LL theory is the anomalous power law suppression of the conductance and DOS known as the ZBA. This is a result of the unique collective nature of the LL state, caused by the strong e-e interactions. The addition of a single electron requires the rearrangement of all other electrons in the state and is thus strongly suppressed at low energies.

Sketch of Derivation of Characteristic Conductance Power Laws:

The Luttinger Hamiltonian*, ignoring spin, which is a separable problem, is:

$$\hat{H} = \int \frac{g}{2}(\frac{d\theta}{dt})^2 + \frac{1}{2g}(\partial_x \theta)^2 dx,$$

Where θ is a displacement field related to the charge density: $\rho(x)=(k_f+\partial_x\theta)/\pi$

Here g, is a measure of the strength of e-e interactions, with g=1 corresponding to no interactions, g<1 corresponding to repulsive interactions, and g>1 corresponding to attractive interactions. Using the commutation relations, one can find the equation of motion, which is the familiar wave equation $\partial_t^2\theta = v^2\partial_x^2\theta$. The charge excitations move at a velocity $v=v_f/g$. In the associated spin density problem we arrive at the same result, only there are no spin interactions, thus g=1 and $v=v_f$. This is what is known as spin-charge separation[47]. Also, note that as g gets smaller, v gets larger, as we would expect for stronger repulsion and therefore a stiffer medium for plasmon propagation. In single-walled CNTs the measured Luttinger parameter is g ≈ 0.3, indicating strongly repulsive interactions.[15]

To calculate the density of states for adding a particle of energy E one can start from Fermi's Golden rule: $\rho_{LL}(E) = 2\pi\sum_n |< n \mid \psi^t(x) \mid 0 >|^2 \ \delta(E_n - E_0 - E)$,

where $|n>$ are the eigenstates of the Luttinger Hamiltonian discussed above, and E_n are the corresponding energies. After a nontrivial mathematical interlude[1] one arrives at: $\rho_{LL}(E) \propto E^{\alpha}$

The exponent, alpha, is a function of the interaction strength, g, and depends crucially on the boundary conditions. For a single walled CNT with four conduction channels contacted on the

* For more details on setting up the Luttinger Hamiltonian see Ref 1.

ends, $\alpha = (g^{-1} - 1)/4$; contacted in the middle, or bulk, $\alpha = (g^{-1} + g - 2)/8$, roughly half of the end value because the electron can "relax" in two directions.

With the LL DOS in hand we can calculate the conductance for tunneling from a Fermi metal lead into a LL:

$$I = 2\pi t^2 \rho_{metal}(E_f) \int_0^V dE \rho_{LL}(E) \propto E^{\alpha+1}$$

$$G = \frac{dI}{dV} = \frac{dI}{dE}\frac{dE}{dV} \propto E^{\alpha}, \quad \text{where } \frac{dE}{dV} = e \text{ and } E = eV + k_b T$$

When eV<<k_bT we can ignore the bias voltage contribution to energy and:

$$G \propto T^{\alpha}; eV << k_b T$$

When eV>>k_bT we can ignore the temperature contribution to the overall energy and:

$$G \propto V^{\alpha}; eV >> k_b T$$

Hence one can measure the Luttinger exponent and extract the strength of e-e interactions from simple transport measurements.

For comparison to experiment, we would like to estimate the expected value of alpha for a given length. We start with a formulation for *g* derived from the original Hubbard Hamiltonian[1]: $g = (1 + \frac{V}{h v_f})^{-\frac{1}{2}}$ which we can write in terms of the charging energy, $U = \frac{e}{C_{total}}$, and the mean level spacing, $\Delta = \frac{h v_f}{4L}$, which leads to $g = (1 + \frac{2U}{\Delta})^{-\frac{1}{2}}$,[48] the stronger the e-e interactions, the larger the charging energy. For the purposes of estimation, we use the classical capacitance, C_c, for a wire above a metal sheet separated by a dielectric: $C_c = \frac{2\pi\varepsilon}{\ln(L/R)} L$, where *L/R* is the aspect ratio and ε is the dielectric constant. Therefore, $g = [1 + \frac{4e^2}{\pi h v_f \varepsilon} \ln(\frac{L}{R})]^{-\frac{1}{2}}$. Plug this back into the equations for alpha and we get Figure 3-5, which shows the expected behavior of the power law exponent alpha as a function of the CNT length.

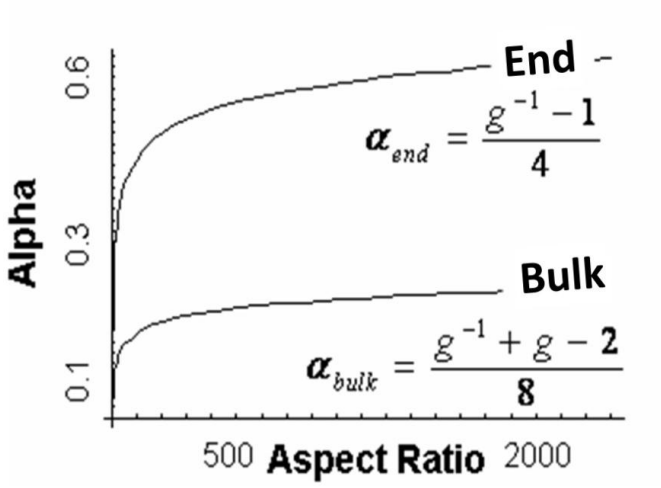

Figure 3-5: Rough prediction of power law exponent alpha as a function of the aspect ratio of the CNT.

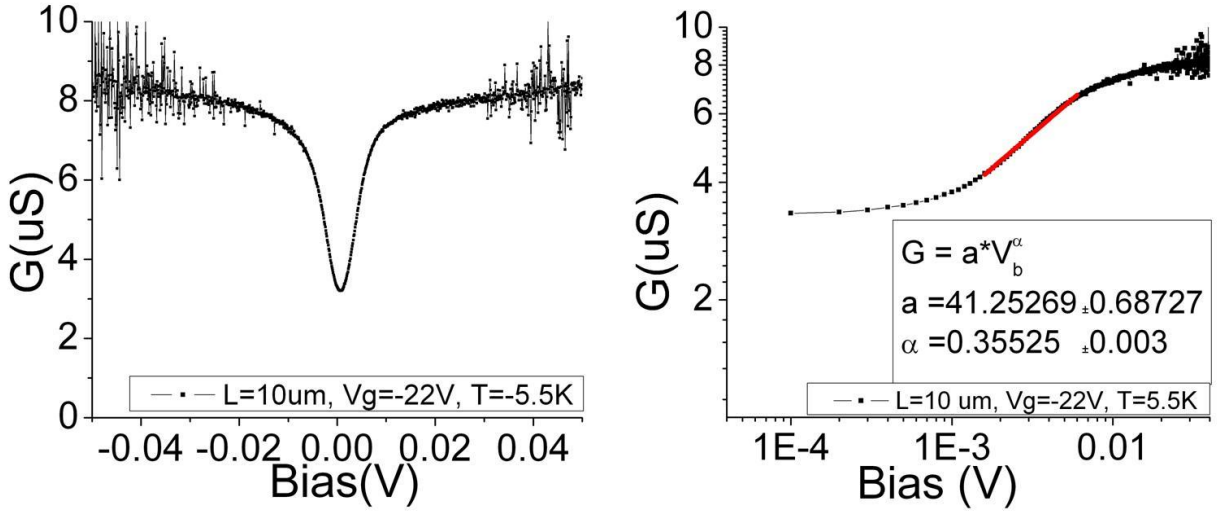

Figure 3-6: On the left is an end-to-end bias sweep of a 10 μm long CNT device at 5.5 K on a linear scale. On the right, is the same data on a log-log scale. Red line is a fit to the equation in the box below, the slope of which is the Luttinger exponent.

3.5 Results and discussion

Figure 3-6 shows a bias sweep of a 10 μm long CNT. On the left is conductance vs. bias voltage on a linear scale. On the right is the same data on a log-log scale, on which the conductance is predicted to be a straight line. Notice that the conduction is thermally smeared at low bias voltage, here beginning just above 1 meV, and also saturated at high bias, which is

beyond the Luttinger regime. We fit the small linear region in between to extract alpha. By performing the same measurements on CNTs of many different lengths we can build up a picture of alpha's dependence on length.

The length dependence of alpha for four different ultra-long CNTs is shown in Figure 3-7. It is clear that alpha increases with length, and the trend is qualitatively similar to the prediction in Figure 3-5. Now, with a hop, skip and a jump we can arrive at the dependence of electron-electron interactions on length. Since $\alpha \propto g^{-1}$ and lower g means stronger repulsive interactions we can say that since alpha increased with length, g decreases with length, and therefore electron-electron interactions become stronger with increased CNT length.

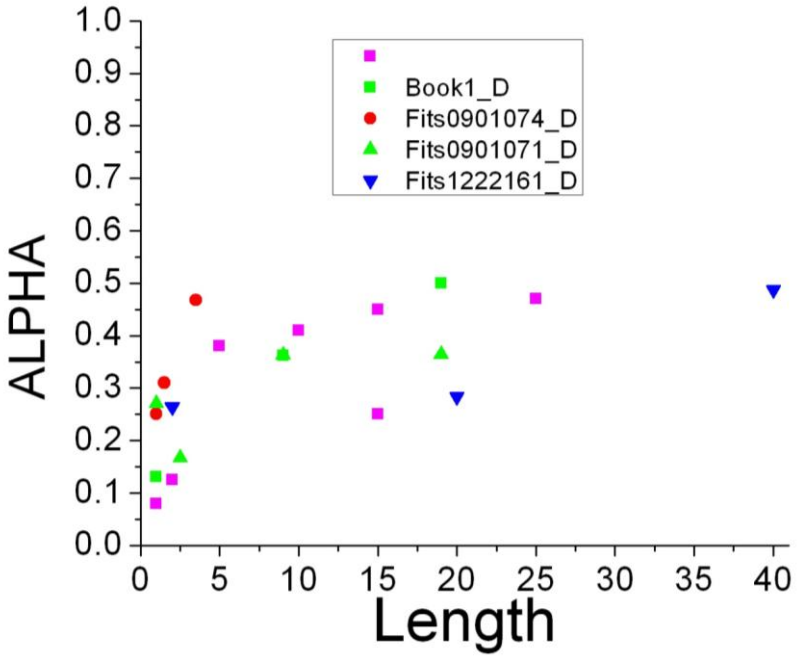

Figure 3-7: Alpha vs. Length for 20 devices on 4 different ultra long CNTs. Two Devices contacted with Pd/Au, and two with Cr/Au. The data is qualitatively similar to the expected evolution of alpha with length shown in Figure 3-5.

However, there are at least three reasons to believe that these small steps might in fact be gaping chasms. There are three separate indications that the CNTs studied here have a defect density of roughly 1 per 2-4 μm. This means the devices studied here are likely composed of several or many Luttinger liquids in series, instead of one whole piece. In other words, much of

our "length dependence" may actually be measurement of multiple tubes of same effective length, given by the defect density, in series.

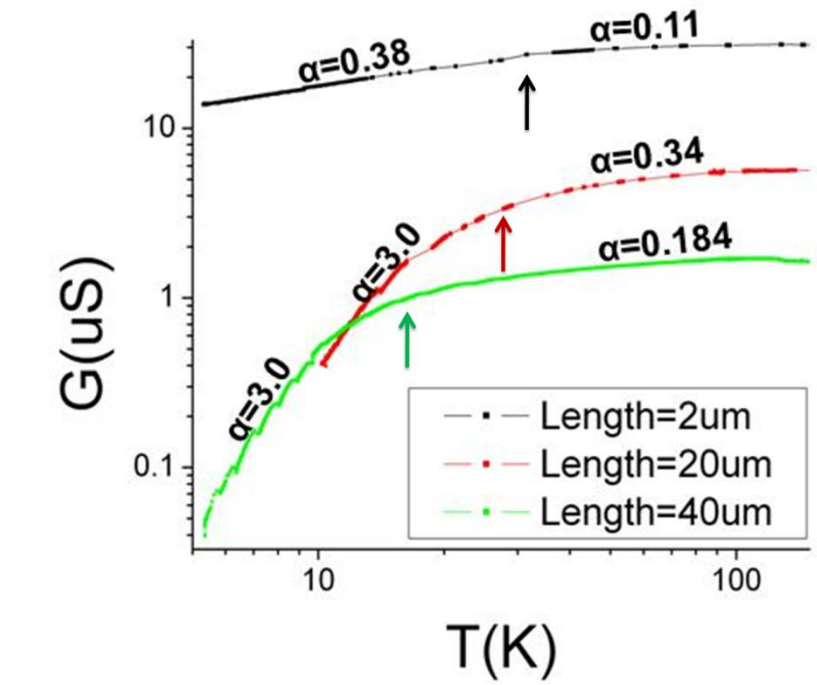

Figure 3-8: Conductance versus Temperature on a log-log plot for three different tube lengths. Arrows point to change in slope. Note the wildly different exponent slopes at high and low temperature.

I will now present three pieces of evidence that defects have broken up the CNT and possibly modified alpha. First, we observe evidence of the "breaking up" of the tube in conductance versus temperature data. It is predicted that in the intermediate temperature regime, between 0D and 1D physics, the zero bias conductance versus temperature sweep will have a kink below which alpha will increase as the charging effects add to the conductance suppression.[49,50] The black curve in Figure 3-8 is a temperature sweep for a 2 μm long CNT device that shows a kink at roughly 30 K, indicated by the black arrow, which is consistent with the above prediction. What is surprising is that longer CNTs show an even sharper drop off at a roughly similar temperature. This is surprising since one would expect the temperature of the kink to decrease with increased CNT length, since both level spacing and charging energy are inversely proportional to length. So for example, if a 2 μm device drops off at 30 K, one would expect a 20 μm to drop off at 3 K and a 40 μm at 1.5 K, instead of ~25 K and 15 K as indicated by the red

and green arrows. There is something else of note: the "kink" for the longer tubes is much more of a gradual drop off and the final slope is ten times steeper than the 2 μm device. It is possible that this is caused by a series of defects in the long CNTs, effectively breaking them up into many devices in series.

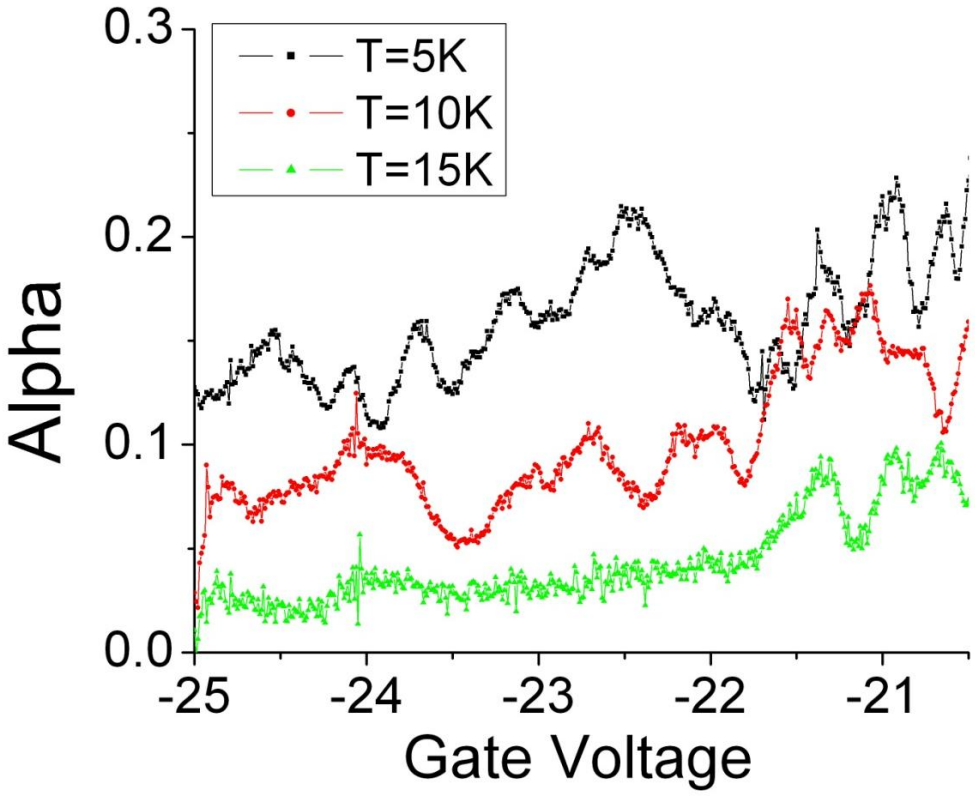

Figure 3-9: Alpha vs. gate voltage for a 10 micron CNT device at 5, 10, and 15 degrees Kelvin.

We also see evidence of defects in the gate voltage dependence of alpha. It is predicted that in the crossover between Coulomb blockade (CB) and Luttinger liquid that alpha varies meaningfully with gate voltage. This has been seen before in multi-walled CNT[49], and is predicted to exist in single walled CNTs as well[50]. We clearly observe this dependence of alpha on gate voltage. See Figure 3-9 for Alpha vs. Vg in a 10 μm CNT. In the crossover regime, CB peaks in the density of states are thermally broadened until they overlap, creating an oscillating DOS, which results in the predicted oscillations in alpha. Observation of these finite size effects up to 15 K is another indication that there is a length scale, shorter than the 10 μm length of the CNT involved, since 15 K >> $\hbar v_f/k_b L$ ~ 1 K. The temperature dependence of the oscillation amplitude is previously unmeasured, though gate hysteresis and the irregular nature of the

oscillations make comparison with theory challenging. We can only say with certainty that the size of the oscillations increases with decreasing temperature as predicted. While interesting in its own right, this effect makes it exceedingly hard to compare values of alpha at particular gate voltages between gate sweeps and therefore between devices. The only alternative is to go to much higher temperatures, where much of the ZBA is washed out by thermal effects. We are also limited by deviations due to gate hysteresis. When the gate is swept in one direction, charge gets trapped in the silicon oxide layer near the CNT, causing the sweep in the other direction to be offset. Thus, in this crossover regime we are left to compare the entire alpha vs. gate voltage curves, which take much longer to procure.

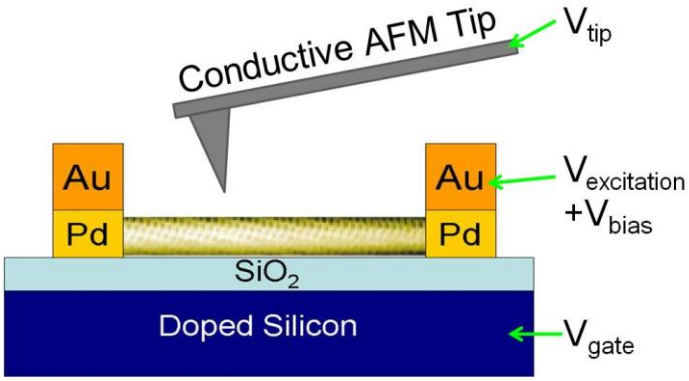

Figure 3-10: Diagram of scanning gate microscopy technique in which conductance through a device is measured while a local gate, in the form of an AFM tip is scanned over the device, mapping out spatially areas of sensitivity to the gate.

As final evidence that our CNT devices have significant defects, some of them were subject to scanning gate microscopy(SGM), a technique used to reveal gate tunable CNT defects.[51] Figure 3-10 illustrated the setup. In SGM an AFM with a conductive tip is used as a local gate. A DC bias is applied to the AFM tip and the tip is scanned over the CNT while the end-to-end conductance is measured. Defects are indicated by areas in which the local gate has an inordinately large effect on conductance. As you can see in Figure 3-11, in this ~2 μm long device we see five areas of conductance modulation. The two at the contacts are expected due to Schottky barriers. The other three are likely defects in the CNT, or local charge traps in the underlying substrate. SGM of very long CNT devices, 20 to 40 μm revealed a defect density of about 3-4 μm, which is the same order of magnitude as that indicated by the temperature sweep data. Unfortunately, we were not able to correlate defect density with the behavior of alpha.

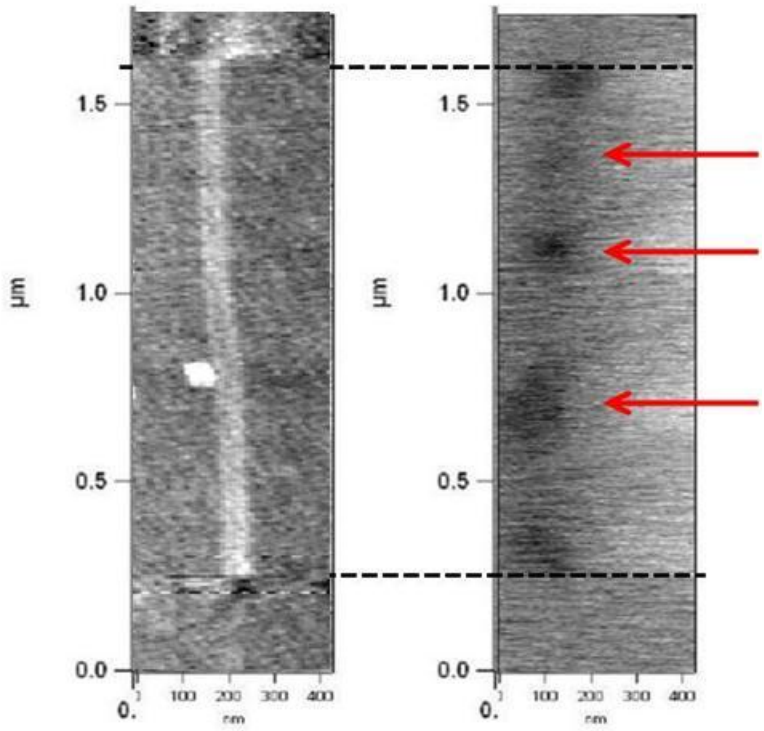

Figure 3-11: On the left, an AFM image of a CNT device contacted at the top and bottom. On the right, a scanning gate microscopy image of the same CNT. There are expected Schottky barriers at both contacts, but three additional areas of conduction modulation are indicated by red arrows.

In conclusion, we have measured the dependence of the ZBA on device length. We have preliminary evidence that alpha increases with length in a way that is roughly consistent with a naïve Luttinger prediction. We have also found that our devices exhibit a defect density on the order of a micron, as indicated by temperature sweeps, variation of alpha with gate voltage, and direct observation with scanning gate microscopy. Thus, zero dimensional effects are seen on a scale that is determined more by the defect density, than the length of the CNT. Consequently, the area over which conductance goes as a power law in both voltage and temperature in long CNTs can be significantly less than expected due to competing effects at low temperature, making the accuracy of power law fits questionable. This unhappy result is forced by tight bounds at high and low energy scales. First empirically, the power law fails to hold on the high side at ~10-20 meV and ~100-125 K, which are roughly equivalent energies. Second, on the low side, the benefits of increased length are lost to defects. In the future, studies will require better control over the defect density. Current routes to decreasing the defect density include

suspending the CNT, or using an oxide layer with fewer charge traps, such as Al_2O_3. Another possibility is to fabricate local gates over defects found with scanning gate microscopy. These defects are gate tunable, and with a local independently addressable gate one could gate the defects away. This would allow not only that study of conductance in a very long Luttinger liquid, but also how conductance changes, as the defects are controllably varied in strength and number.

Chapter 4
Non-equilibrium Tunneling Spectroscopy*

As demonstrated in Chapter 3, although e-e interactions are thought to be particularly strong in CNTs and important in CNT transport[14,48,52-54], it is challenging to measure their strength with any precision in two-probe measurements. Two-probe measurements determine the strength of e-e interactions through the CNT DOS which is suppressed by the power law exponent alpha. As discussed in the previous chapter there are many problems with the accuracy of these measurements, so it is desirable to find a more direct path to determine e-e interactions. Two-probe normal metal tunneling spectroscopy measurements only probe the CNT density of states convolved with a Fermi distribution. However, measurement of the *non-equilibrium* electron energy distribution function, f (E) should give direct information about energy relaxation processes† and scattering rates that is not accessible in the DOS.[55-58] In this chapter I will discuss how we adapt to CNTs a beautiful non-equilibrium tunneling spectroscopy technique first demonstrated in mesoscopic wires.[59] This technique allowed the non-equilibrium f (E) and hence the scattering rate between quasiparticles in the wire to be quantitatively determined.[59] CNTs are true one dimensional systems, so they are expected to show stronger electron-electron interaction

* This work is reproduced in part from: Chen, Y.-F., Dirks, T., Al-Zoubi, G., Birge, N. O. & Mason, N. Nonequilibrium Tunneling Spectroscopy in Carbon Nanotubes. *Physical Review Letters* **102**, 036804 (2009).

† By "energy relaxation processes" we mean those processes that allow two populations of electrons with differing energy distributions to exchange energy and come to a thermalized equilibrium.

effects than mesoscopic wires. In addition, in the studied temperature ranges, CNTs should exhibit Luttinger Liquid behavior. It is believed that energy relaxation does not occur in a uniform clean Luttinger liquid because forward scattering processes cannot satisfy both energy and momentum conservation laws.[56] However, in the presence of interactions that vary spatially, as one might expect near the contacts of a finite CNT device[56], and in the presence of backscattering defects,[55] energy relaxation may be allowed.

The non-equilibrium tunneling spectroscopy technique requires a means of biasing the electrons in the CNT out of equilibrium while measuring the tunneling current through a weakly coupled probe that has a sharp feature in the DOS, here a superconductor. Creating such a device in CNTs required the surmounting of a perennial problem in CNT device fabrication: evaporated metal contacts damage the underlying tube, effectively cutting it. Thus, while multi-terminal measurements on CNTs have been demonstrated with scanned probes[60] and molecular leads,[61] lithographically fabricating probes remained elusive despite their many advantages, such as allowing for the possibility of utilizing multiple probes of varying materials. As discussed below, we have solved the problem of fabricating non-invasive terminals to CNTs, and here present a review of the first measurements of a CNT non-equilibrium f (E). We also present current efforts to extend the technique.

I inherited this experimental technique in fine working order from Yung-Fu Chen, a former postdoc in our lab, who developed the crucial technique for putting down a non-invasive tunnel probe and measuring CNTs out of equilibrium. I joined the project near its middle, initially to provide clean CNTs with low resistance contacts. While I fabricated and helped measure a couple of supplementary samples, the work I will review in the first part of the chapter is primarily his. After reviewing what the technique is, and what we can learn from it, I will outline the way in which I have worked to extend it.

4.1 Fabrication and Measurement Methods

As depicted in Figure 4-1, the devices studied in this chapter consist of metallic single-walled carbon nanotubes with diameters of 1-3 nm, lengths 1.1-2.0 μm. Fabrication details are covered in Chapter 2 and Appendix1. The devices were made with high conductance contacts at each end (0.3 nm Cr / 35 nm Au or 6.5 nm Pd / 35 nm Au), a superconducting tunneling probe in the

middle (200 nm wide, 200 nm thick Pb caped with 30 nm In to prevent oxidation), and a heavily doped Si substrate as a backgate. The tunnel probes are separated from the nanotubes by ~1.2 nm of AlO_x. The oxide provides tunneling resistances through the probes, R_{tunnel} ~ 1-5 MOhm, that are typically 10-100 times larger than the nanotubes' end-to-end resistances, $R_{end\text{-}to\text{-}end}$. In order to reliably measure the non-equilibrium f (E), the tunnel probe itself should not change the distribution. Therefore the current through the CNT should be dominated by electrons from the end contacts, implying that the resistance through the end contacts should be significantly lower than through the tunnel probe.[62] Therefore, we only measure samples that have $R_{tunnel} >> R_{end\text{-}to\text{-}end}$. This technique relies heavily on the ALD system's ability to produce uniform monolayers without pin holes. The difference between $R_{tunnel} \sim R_{end\text{-}to\text{-}end}$ and R_{tunnel} effectively insulating is only about 3 atomic layers.

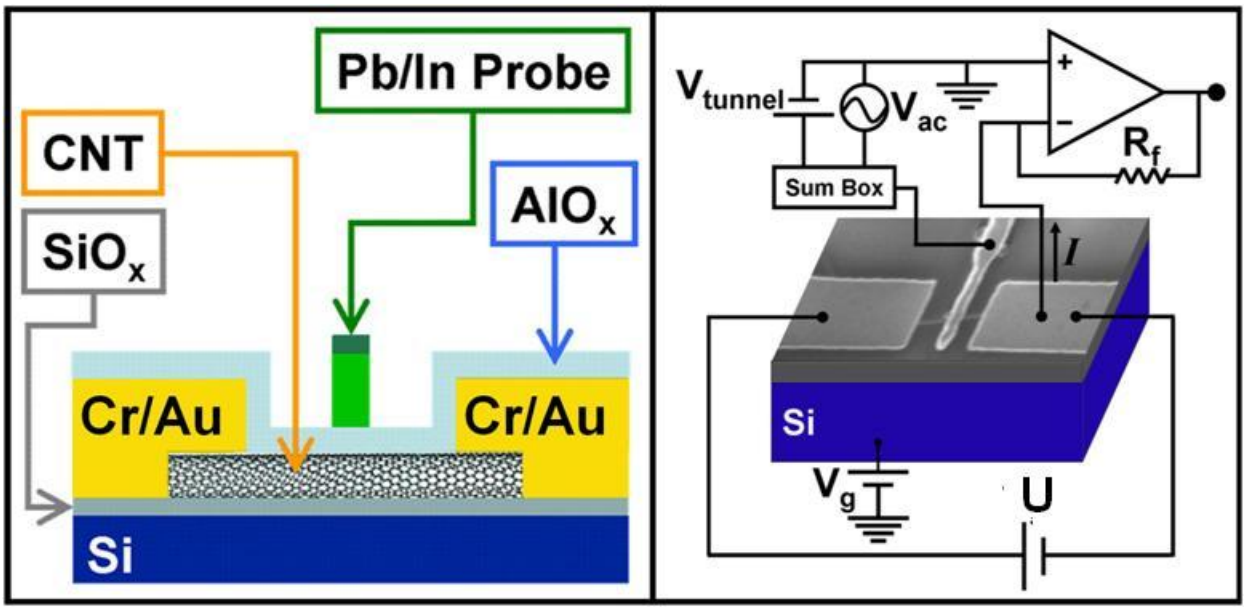

Figure 4-1: On the left, side cut sample geometry showing the layering of the CNT, end contacts, Al_20_3, and SC tunnel probe. On the right, an SEM image of a typical device, with diagram of the measurement circuit.

Measurements were made through heavily filtered leads in a top-loading dilution refrigerator and in an Oxford He^3 cryostat. Tunneling differential conductance measurements were performed by applying a sum of dc bias voltage V_{tunnel} and ac excitation voltage V_{ac} to the superconducting probe, and a voltage V_g to the back gate, while measuring the current I at one of the nanotube end contacts (see Figure 4-1 on right). For the non-equilibrium measurements, a

non-zero DC voltage U was applied across the nanotube end contacts.* Five devices, on separate chips, were measured in detail; all behaved similarly in non-equilibrium measurements. In the following I will present results from one of those devices.

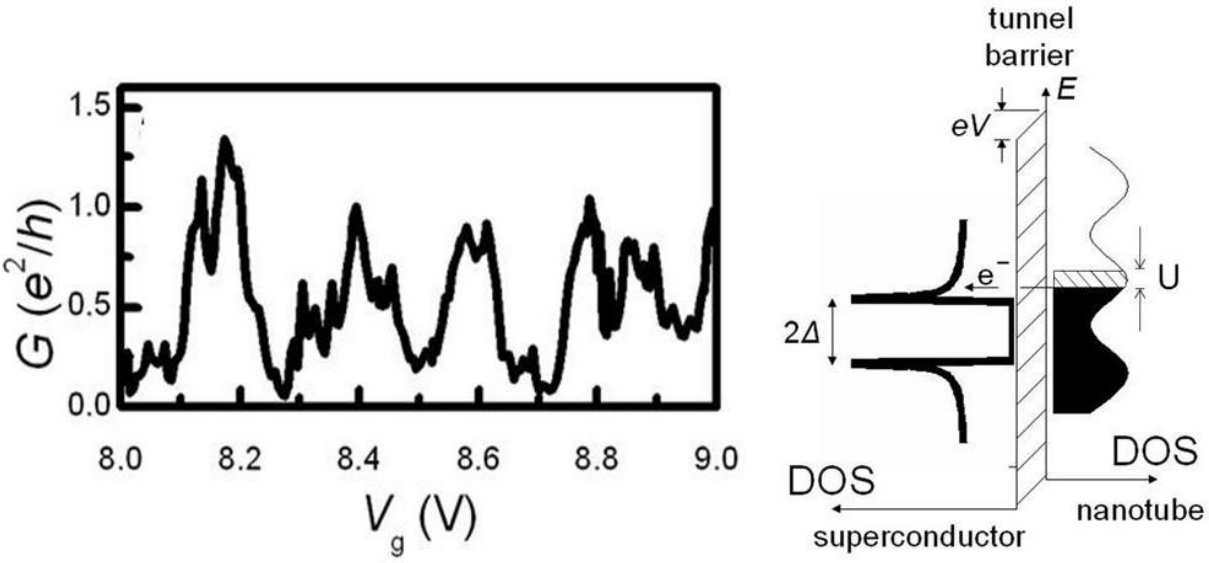

Figure 4-2: On the left, end-to-end differential conductance at U = 1 mV as a function of gate voltage at T=1.5K. Broadened oscillatory peaks indicate the CNT is in the open quantum dot regime. On the right, schematic diagram of an electron tunneling from a nanotube to a superconductor. The density of states (DOS) of the nanotube shows a modulation with single-particle energy spacing, as expected for an open quantum dot, while the superconducting DOS exhibits a BCS-like gap of 2Δ. The Tunnel probe bias is depicted at the tunnel barrier as eV, and the end bias shown, labeled U. The hashed area between the Fermi energy for the grounded lead and U indicates partially filled levels.

4.2 Sample Characterization and Equilibrium Measurements

Figure 4-2 shows nanotube end-to-end conductance as a function of gate voltage V_g, at temperature $T \approx 1.5$ K. Although $k_B T$ is smaller than the level spacing ($hv_F/L \sim 1$ meV) and charging energy ($e^2/2C \sim 2$ meV), the tube conductance does not pinch off to zero. In addition, although we see some oscillations as a function of V_g and U, the conductance values reach $\sim e^2/h$ and any peaks are broadened. These observations imply that the coupling between the nanotube

* For discussion of how to circumvent the tricky grounding loop problems that this configuration presents see section 2.6.

and the end contacts is strong, so that the measurements are taken in an open quantum dot regime. Thus, for the purpose of this experiment, the CNTs are treated as having a continuous DOS that can be slightly modulated with V_g and U (see Figure 4-2).

When the nanotube is in equilibrium (U = 0), the tunneling current $I(V)$ through the superconductor/insulator/nanotube junction, in the open dot regime with bias V across the junction, is given by

$$I(V) \approx \frac{1}{eR_T}\int_{-\infty}^{\infty} dE n_s(E+eV) n_{nt}(E)(f_{nt}(E) - f_s(E+eV)), \qquad (1)$$

where R_T is the tunnel resistance of the junction, E is the energy relative to the Fermi energy of the nanotube, n_s is the normalized BCS superconductor DOS, n_{nt} is the normalized nanotube DOS, and f_{nt} and f_s are the Fermi distributions of the electrons in the nanotube and Pb probe, respectively. The nanotube DOS $n_{nt}(E)$ is extracted from the equilibrium tunneling data by deconvolving Eq. (1). Although $n_{nt}(E)$ should have power law dependence as a function of E if the nanotube is an ideal Luttinger liquid, this behavior is not usually seen in our samples (see Ref [63]); it is likely masked by the level discreteness, as the Thouless energy $\hbar v_F/L \sim 0.26$ mV is comparable to the measurement temperatures [64].

Figure 4-3 shows the differential tunneling conductance versus tunnel bias, dI/dV vs. V, of sample A at V_g = 8.285 V and T = 1.3 K. The expected [65] Pb superconducting gap $2\Delta \sim 2.6$ meV is evident as a zero conductance region centered around V = 0 between peaks at $V = \pm\Delta/e$. The peaks are BCS superconductor peaks convolved with the DOS of the nanotube and Fermi distributions of the Pb and the nanotube. The quality of the gap shows that the tunnel junction is relatively clean and non-invasive, and can indeed be used for energy-resolved spectroscopy. Above and below the gap region several more broadened peaks are also evident; these can be understood as tunneling peaks through multiple charge states in the open quantum dot (see Figure 4-2 on right).

4.3 Non-equilibrium Measurements and Results

Next a non-zero voltage U is applied across the end contacts to drive the electrons in the nanotube out of equilibrium [66]: this introduces phase space for e-e scattering and allows measurement of the energy relaxation rates which may be due to this scattering. Because a

complete theory for tunneling into a non-equilibrium one-dimensional system has not yet been formulated, we follow the precedent set in metals [66] and model our data using Eq. (1) with $f_{nt,U}(E)$ to be determined by experiment. In metal wires, $f_U(E)$ depends on the extent of electron energy relaxation in the wire, i.e. on the product of the inelastic scattering rate and the dwell time of an electron in the wire. This dependence can be understood by first considering two extreme cases: no inelastic scattering between electrons and strong inelastic scattering between electrons.

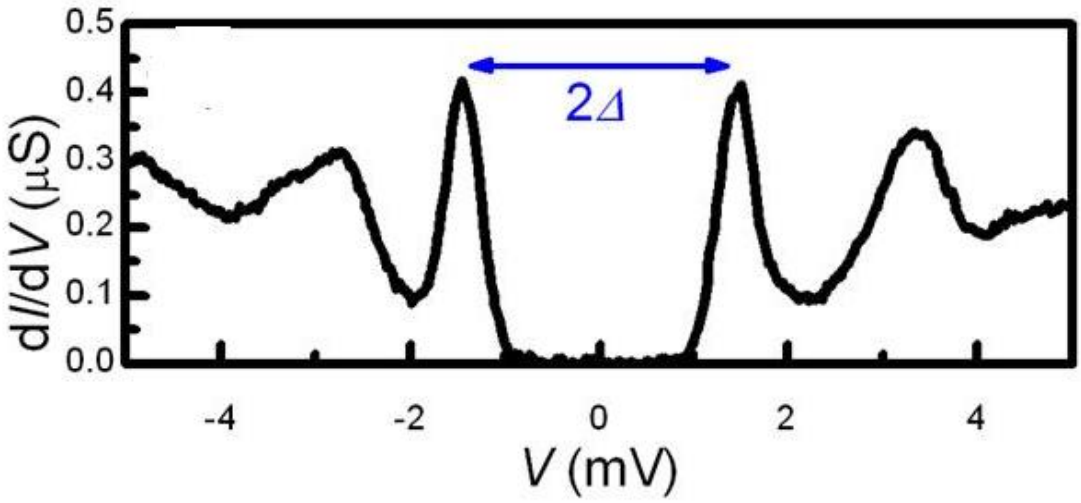

Figure 4-3: Tunneling differential conductance, dI/dV from the superconductor into the nanotube, as a function of V at V_g = 8.285 V. The blue arrow indicates the Pb superconducting gap size. Additional peaks at V ~ -4.9, -2.8, 3.4 mV are resonant tunneling peaks through the open quantum dot defined by the nanotube leads. T=1.5K

In the first case, the non-interacting distribution function preserves the distributions of the two leads [67]: $f_0(E) = rf_L(E) + (1 - r)f_R(E)$, where $f_L(E) = (1 + \exp((E + eU)/k_BT))^{-1}$ and $f_R(E) = (1 + \exp(E/k_BT))^{-1}$ are the Fermi distributions in the left and right end contacts (with the right end grounded), respectively, and r is the weight of $f_L(E)$ (determined by the tunneling rates into the two ends of the tube, the diffusivity of the nanotube, and the position of the superconducting probe [59,66]). When $eU >> k_BT$, $f_0(E)$ is thus a two-step function with a step a 0 and U. See Figure 4-4 on the left. When the SC peak is scanned across this two step function, as the tunnel bias is changed, there is a large change in conductance at each step. Thus measuring dI/dV, one expects a doubling of the SC peaks, separated by U. In the case of strong inelastic scattering between electrons a local electronic thermal equilibrium is created, with an effective temperature $T_{eff} \sim eU/k_B$ when $eU >> k_BT$ [66,68]. This "hot" Fermi distribution is marked by a single broadened step.

This results in a single broadened, displaced set of SC peaks in the conductance versus bias sweep (see Figure 4-4 on the right). In general, the steady-state distribution function $f_{nt,U}(E)$ is between these two extreme cases and the shape of the distribution function reveals the extent of inelastic e-e scattering.

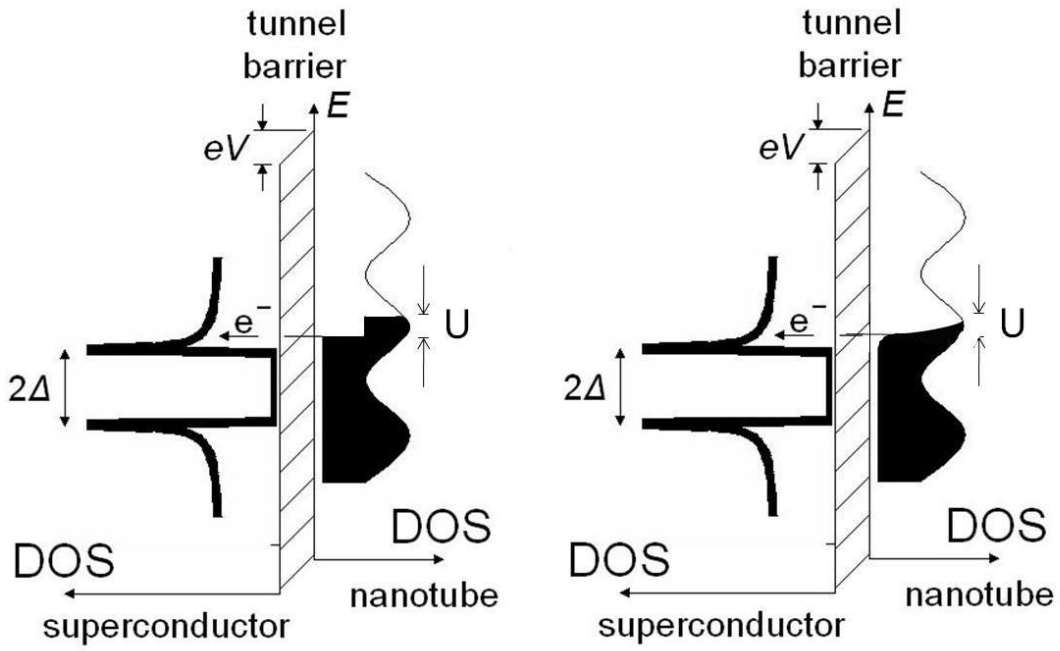

Figure 4-4: Energy diagram for non-equilibrium bias sweep in the case of no relaxation on the left and total thermalization on the right. The black section of the nanotube DOS indicates the shape of f (E). On the left a two step Fermi function. On the right, a smeared or thermalized Fermi distribution.

At T = 1.3 K, we see evidence of both strong and weak inelastic e-e scattering. The top of Column (a) in Figure 4-5 shows dI/dV(V) for various values of bias U across the end contacts; columns (b) and (c) show the same data taken at different gate voltages. The arrows in Fig. 3(a) indicate the superconducting peaks splitting at finite U. The decreasing height of the peaks at $V = \pm\Delta/e$ (compared with U = 0) and the newly developed peaks at $V = \pm\Delta/e + U$ are due to the fact that the states in the nanotube in the energy range of ($-eU$, 0) are now partially occupied. From the differential form of Eq. (1) for finite U, we see that the clear separation between the peaks implies that the electron distribution now has two steps, at $E \sim 0$ and $-eU$, and thus that energy relaxation processes are weak. Figure 3(b), taken at a slightly different gate voltage, shows superconducting peaks that shift slightly, rather than separate, with U. In this case, instead of

having a two-step-like electron distribution, $f_{nt,U}(E)$ has only one broad step in the energy range of ($-eU$, 0), implying that energy relaxation processes are strong. Figure 3(c) shows behavior somewhere between 3(a) and 3(b). If relaxation were caused by defects[55] being tuned in and out one might expect to see less relaxation at high conductance and more at low conductance. Although the back gate voltage tunes the nanotube conductance, we do not observe a clear correspondence between nanotube conductance and energy relaxation processes at finite U: data taken at $T \sim 1.5$ K with end-to-end conductance varied by up to a factor of 15 (near both peaks and valleys, for two samples at nine different gate voltages) shows little correlation between conductance values and the behavior of the superconducting peaks.

In the middle row of Figure 4-5 we show the electron energy distribution functions extracted from the tunneling data in the top row; the deconvolution was done using the differential form of Equation (1) (see Ref. [69]). The shapes of the distributions are as expected from the behaviors of the peaks in the top row and the discussion above. The existence of double-step distribution functions for some of the curves (e.g., column (a)) indicates that it is possible for the electrons to maintain their energy distribution across the lengths of the samples. However, surprisingly, the distribution functions are sometimes smeared and one-step-like near $T \sim 1.3$ K (c.f., column (b)), even though $U >> k_B T/e$. At much lower temperatures (~50 mK), the distribution functions are always two-step like and describe a system with weak energy relaxation.

Finally, the bottom row of Figure 4-5 shows the normalized DOS (n_{nt}) obtained by fitting the data in the top row; the data is consistent with our original assumption that the DOS is continuous and slow varying. We note that the calculated distribution functions are very robust to small changes of Δ and $n_{nt,U}(E)$ in the deconvolution process, implying that the shape of $f(E)$ is rather independent of the precise details of the fitting procedure. In addition, although some aspects of $f(E)$ are affected by the fitting procedure—and even though the non-equilibrium form of Eq. (1) may not be exact for interacting systems—the overall shape of $f(E)$, double-step or rounded, is consistent with the qualitative behavior of the superconducting peaks in the raw $dI/dV(V)$ data.

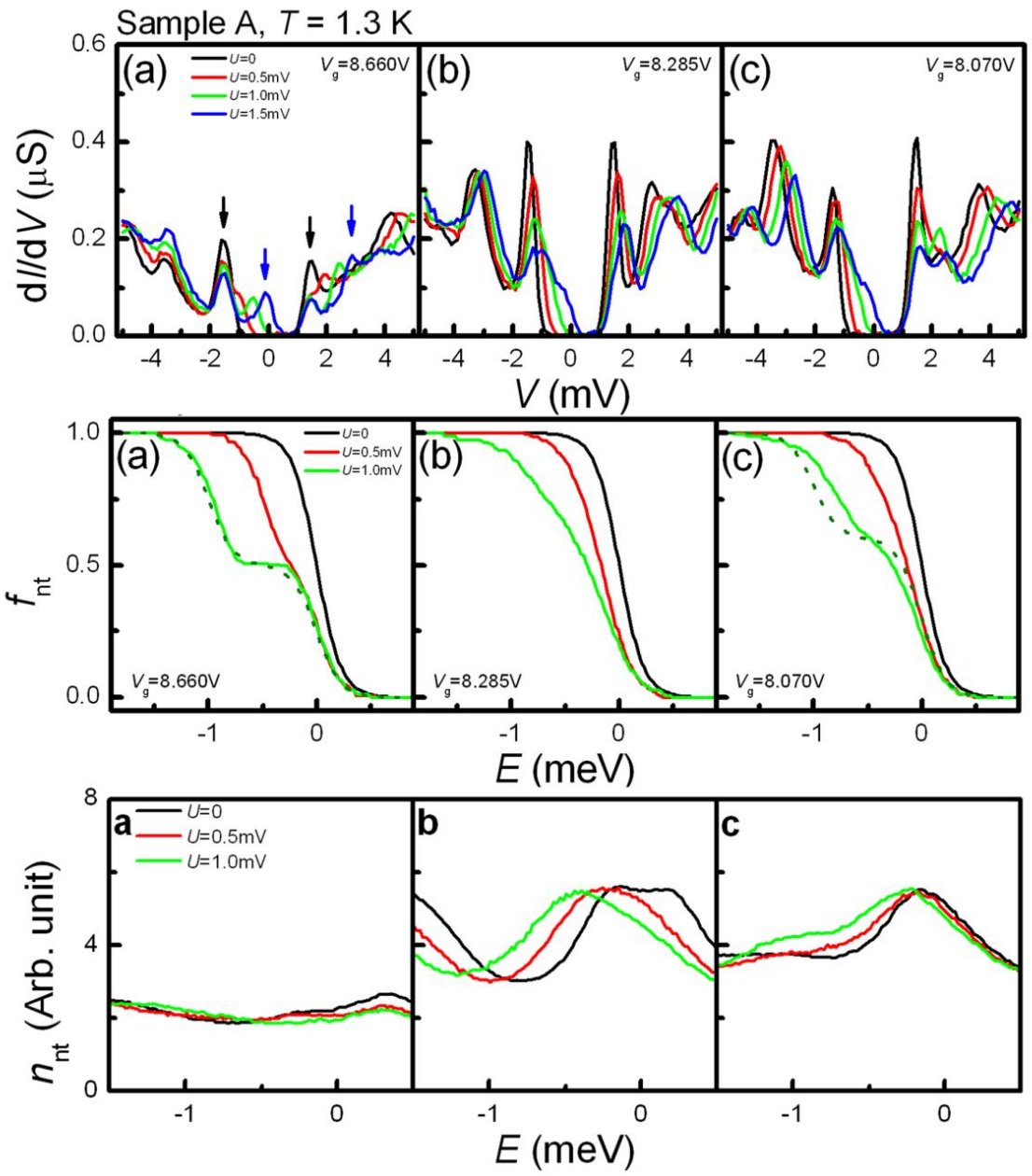

Figure 4-5: Top row, Tunneling differential conductance dI/dV vs. V at multiple values of bias voltage, U, across the tube ends. (a) Sample A at T = 1.3 K, V_{gate} = 8.660 V. The peaks marked by black arrows are the superconducting peaks at $V = \pm\Delta/e$; the blue peaks marked by blue arrows are the superconducting peaks at $V = \pm\Delta/e + U$ (in this case U = 1.5 mV), (b) Sample A at T = 1.3 K, V_{gate} = 8.285 V, (c) Sample A at T = 1.3 K, V_{gate} = 8.070 V. Middle Row; Electron energy distributions calculated from the dI/dV(V) data in the top row. Two-step functions (a), imply limited e-e scattering, while broadened single-step functions (b), imply strong e-e scattering. The dotted lines are non-interacting distribution functions $f_0(E)$ with U = 1.0 mV, T = 1.3 K, r = 0.5 in (a), and U = 1.0 mV, T = 1.3 K, r = 0.4 in (c). Bottom row; Normalized nanotube DOS obtained from fitting the dI/dV(V) data in the top row.

Our data imply that inelastic scattering processes can be relatively weak in nanotubes. We do not see evidence of relaxation at temperatures well below 1.5 K, even in data taken at eight different gate voltage values where the tube conductance varies by a factor of 20. This may be because the typical electron dwell time in our tubes is short compared with that in a disordered metallic wire; $\tau = L/(v_F{*}t) \approx 50$ ps for a 2-micron long tube with nanotube Fermi velocity $v_F \approx 8 \times 10^5$ m/s and transmission $t = 0.05$ (corresponding to $R_{\text{end-to-end}} = 130$ kΩ). However, even dwell times up to 400 ps ($R_{\text{end-to-end}} \sim 1$ MΩ) do not lead to smearing of $f(E)$. The crossover from one-dimension to zero-dimensions may also limit inelastic scattering: in our samples the ballistic Thouless energy, $\hbar v_F/L \sim 0.26$ meV, is not much smaller than the typical bias voltage $U = 1.0$ mV. Our results may be consistent with recent theoretical predictions of no energy relaxation in out-of-equilibrium Luttinger liquid systems [70-73] unless the system is disordered [55].

4.4 Current and Future Efforts

Overall, tunneling spectroscopy with a superconducting probe is clearly a powerful new tool for characterizing e-e scattering and energy relaxation in carbon nanotubes. I've worked to extend this technique in several ways. First, I have fabricated and measured several samples, containing many devices of the two geometries shown in Figure 4-6. These devices allow measurement of the non-equilibrium f (E)'s dependence on distance from the end contacts in a finite CNT device. The device on the left has a single tunnel probe, which is offset from the center of the device. The device on the right contains two tunnel probes with different offsets from the nearest contact.

By fabricating several of these devices, potentially on the same ultra-long CNT, a picture of the density of states and non-equilibrium f (E) as a function of distance from the end contacts can be built up. This information will shed light on several open questions. First, does the non-equilibrium f (E) transition from a two step function near the end contacts to a smeared/relaxed distribution near the center of the CNT in relatively long devices due to increased time spent in the CNT? Or is the function uniformly smeared, since relaxation in finite Luttinger liquid devices is thought to occur mostly near the contacts.[56] Second, to what degree is conduction in the CNT ballistic or diffusive? If conduction is diffusive, the relative height of the double step

should change.[59] If conduction is ballistic the height of the step should always be half way between the energy of the left and right leads.[74] (see Figure 4-7) Finally, long wavelength, low energy, particle-in-a-box like excitations in the density of states are expected in finite Luttinger liquids[75] (see Figure 4-8). By strategically placing several tunnel probes, it may be possible to identify and distinguish between the low energy states.

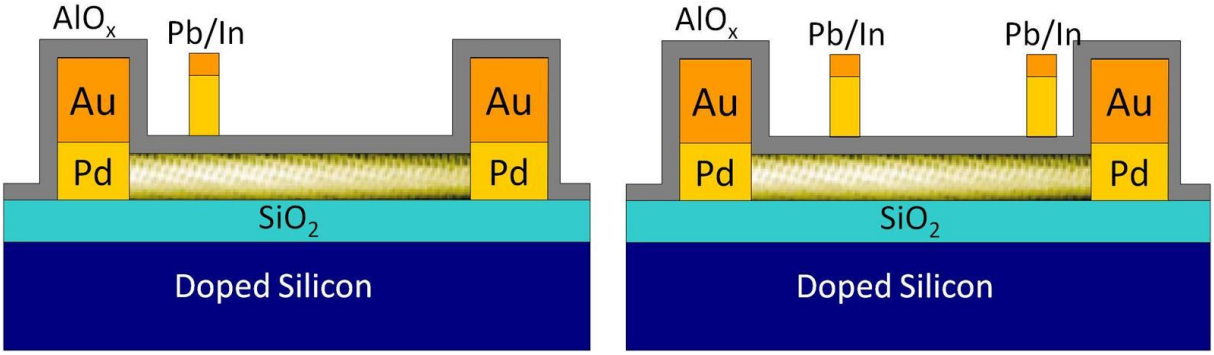

Figure 4-6: Device geometries for studying the energy relaxation as a function of distance from end contacts.

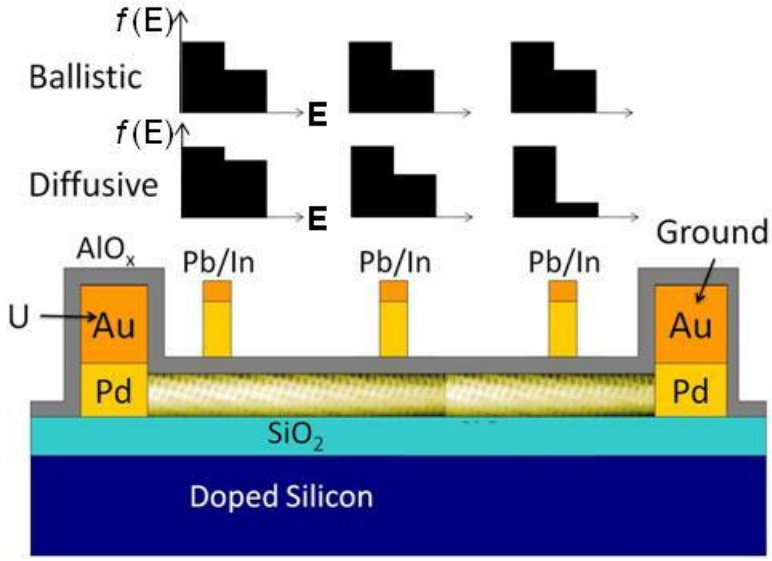

Figure 4-7: Depiction of two different evolutions of the non-equilibrium f (E) with probe position, which we should be able to distinguish between.

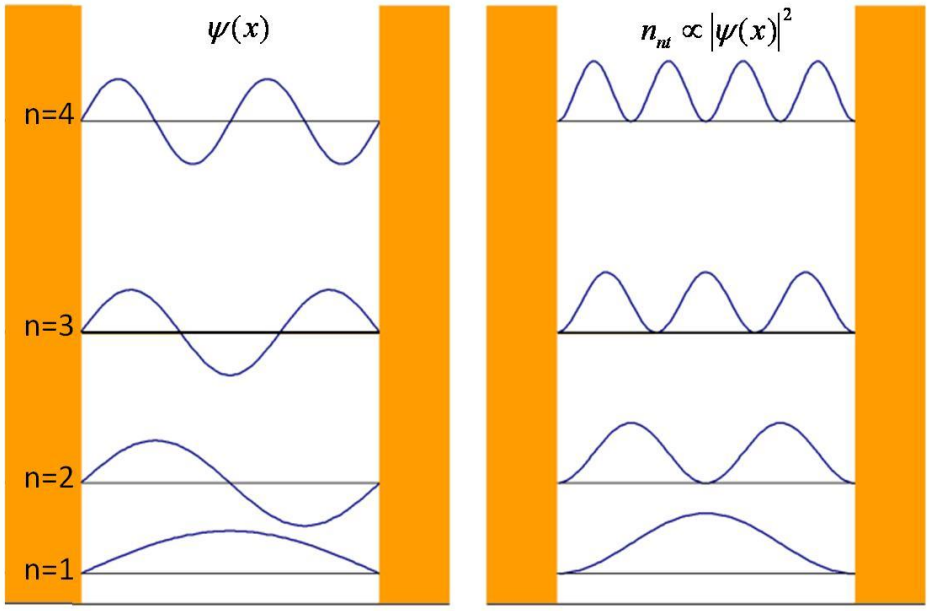

Figure 4-8: Simple particle-in-a-box wave functions. The Luttinger density of states in finite lengths is predicted to be proportional to $|\psi|^2$.[75]

One might wonder, why not make devices with many tunnel probes, so as to map out the length dependence of *f* (E) in a single device? A lesson that I have found must be learned personally and repeatedly in nanofabrication is that any change is a big change, because you can never anticipate all the important variables. For this reason we decided to fabricate devices in which a single probe is offset, as well as devices with two-probes. Sure enough, two-probe devices fail to conduct after tunnel probe evaporation with abnormal frequency. Part of the reason is that two-probe devices must be about 30% longer. This increases R_{end} and therefore the required R_{tunnel}. However, I suspect that the major cause of device failure is a tendency for the underlying CNT to be shocked during or after evaporation of the Pb tunnel probes and that the addition of the second tunnel probe doubles the likelihood of this occurrence.

Unfortunately the realization of offset and multiple tunnel probes has been significantly delayed by frequent equipment failures over the past year. The break downs have been particularly extended in the Atomic Layer Deposition system and the Raith e-beam lithography machine, both of which are absolutely crucial for this work. However, both seem to be working at the moment, and we hope for new results soon.

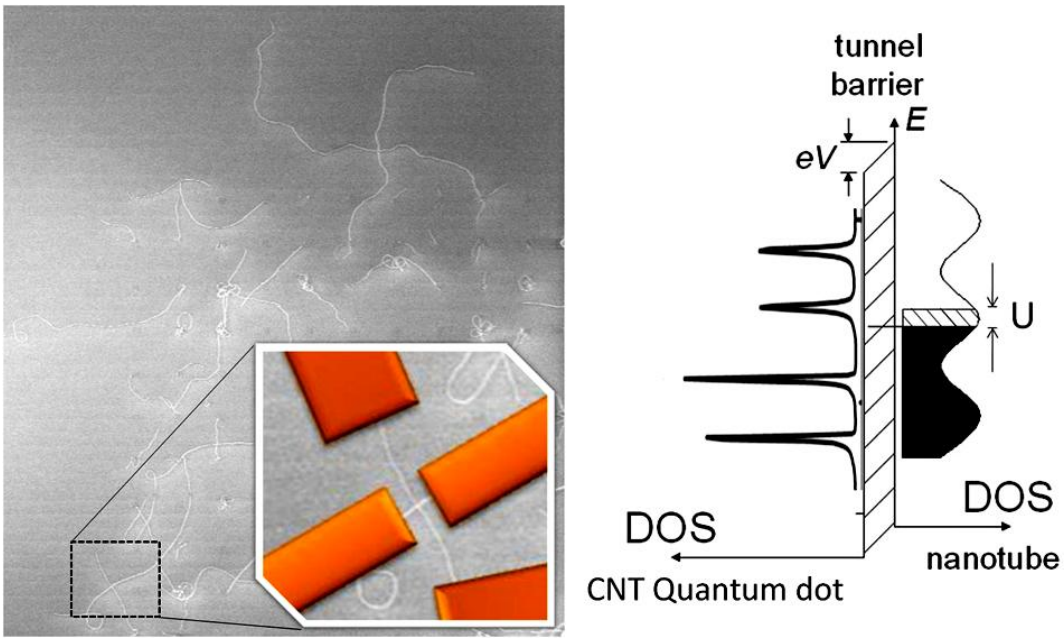

Figure 4-9: New method of non-equilibrium tunneling spectroscopy, in which the probe is a CNT quantum dot. On the left, an SEM of a crossed CNT growth. Inset a depiction of typical device geometry, with on very short CNT functioning as the tunnel probe. On the right, a depiction of the expected tunnel junction analogous to Figure 4-2, in which the Non-equilibrium f (e) is probed by the Coulomb blockade peak, rather than the SC peaks.

Finally I am working an alternate method of non-equilibrium tunneling spectroscopy. The crucial requirement of the technique is a sharp feature in the DOS of the tunnel probe. In the above work, this role was filled by the SC peaks at the BCS gap. In the alternative method this role is will be filled by a CNT in the near-Coulomb blockade regime. The idea is to use a CNT quantum dot in place of the superconductor as the non-equilibrium tunneling spectroscopy probe for a 1D CNT device, as shown in Figure 4-9. In the Coulomb Blockade regime, the temperature is less than the QD charging energy, $U_{c,}$ and energy level spacing, ΔE, which leads to a series of peaks in the conductance spectra and the DOS. In a CNT both U_c and ΔE are inversely proportional to the length. We take advantage of the fact that the sharpness of thermally broadened CB peaks scale with the temperature and inversely with device length by fabricating a crossed tube device in which one CNT is much shorter than the other. Thus, by measuring in the correct temperature regime, $T \sim \Delta E_{shortCNT} / k_{b,}$ one device, the short one, will have a sharply peaked DOS and function as the spectroscopy probe. The other, the longer one, will have a

continuous slowly varying DOS (See Figure 4-9) like the devices presented earlier in this chapter.

I have contacted 8 pairs of crossed tubes with one of the pair fairly long, 2-5 μm, and one fairly short, 0.2-0.5 μm. The crossed tubes are produced in two ultra-long CNTs growths, which are semi aligned. After the first growth Fe catalyst is redeposited and a growth is done at 90 degrees to the first. I have fabricated and measured 8 such devices at room temperature and will measure them at low temperature soon. Initial measurements indicate very low resistance at the CNT-CNT junctions, ~10 kΩ. If this is generally true if could allow for development of crossed-CNT electron, Michelson or Mach-Zehnder type interferometers, which would clear the way for the importation of many of the schemes and advances from optical quantum computing to a small chip based system. However in the context of this work if these low junction resistances persist at low temperatures the devices will be unsuited to non-equilibrium measurement, since current through the CNT would be dominated by electrons from the tunnel probe. If this is the case, in future devices I will place an ALD layer between the two CNTs.

A CNT tunnel probe should be very non-invasive, with contact likely occurring at just a few atoms. Importantly we will also not be limited to such low temperatures by the SC critical temperature. In fact, the only limit is how short one can fabricate devices. With devices of the dimensions mentioned above measurement of the non-equilibrium f (E) in the temperature range between 20 and 50 K should be possible. In this range the longer CNT should not display the zero dimensional effects that somewhat complicated the above work. This technique could open up an entirely new temperature regime to non-equilibrium tunneling spectroscopy.

Chapter 5
Superconducting Tunneling Spectroscopy of a Carbon Nanotube Quantum Dot*

5.1 Introduction

In the last chapter we took advantage of the sharply peaked DOS of a superconducting tunnel probe to study the electron energy distribution in CNTs. Here we take advantage of the large DOS of the SC peak to observe weak tunneling processes. Whereas in the work discussed in the last chapter it was necessary that $R_{tunnel} >> R_{end\text{-}to\text{-}end}$ to avoid affecting the non-equilibrium f (E), here, because we wish to amplify weak signals, R_{tunnel} is much lower, only a few times $R_{end\text{-}to\text{-}end}$. In this chapter, we focus on CNTs in the quantum dot regime, i.e, where electrons are spatially confined to a "box" and display discrete energy spectra. The CNT's have extremely small diameters (~1 nm) making the energy levels in the radial and (the related) circumferential directions very sharply quantized. Thus, the energy regime studied here corresponds to only the ground states of these dimensions (see Chapter 1 for more details). In a CNT quantum dot, the length of the CNT is also cut, to such a degree that the energy levels along the length become noticeably quantized. Physically this is accomplished by evaporating end contacts a short distance from each other on a CNT. Because the contacts damage the underlying tube, the CNT is cut to roughly the distance between the leads, L. The "particle in a box" energy level spacing

* This work is reproduced in part from: Dirks, T., Chen, Y.-F., Birge, N., Mason, N. Superconducting tunneling spectroscopy of a carbon nanotube quantum dot. Appl. Phys. Lett. **95**, 192103 (2009)

is $\Delta E = hv_f / 2L$. Quantum dots are also characterized by a charging energy, $U = e^2 / C_\Sigma$, which is the Coulomb charging energy necessary to add an electron to the dot. In CNTs the charging energy is of the same order of magnitude as the ΔE and is also proportional to 1/L.

Part (a) of Figure 5-1 shows a schematic of a quantum dot, which is connected through tunneling barriers to two normal metal contacts. The dot is also capacitively coupled to those contacts, as well as to the back gate. When both $\Delta E \gg eV + k_b T$ and $U \gg eV + k_b T$ resonant tunneling peaks can be observed. Part (b) of Figure 5-1 shows an energy diagram depicting resonant tunneling through the grounded contact. Part (c) illustrates the zero bias differential conductance as the backgate voltage is varied and four consecutive levels are brought into resonance with the end contacts, demonstrating the conductance peaks (Coulomb blockade peaks) that are separated by ΔE + U. Also shown, in part (d), is a 2D stability diagram which maps out the position of the resonant tunneling peaks on a bias voltage versus gate voltage plot and demonstrates the "diamond structure" from which the energy spectrum of the dot can be spectroscopically determined.

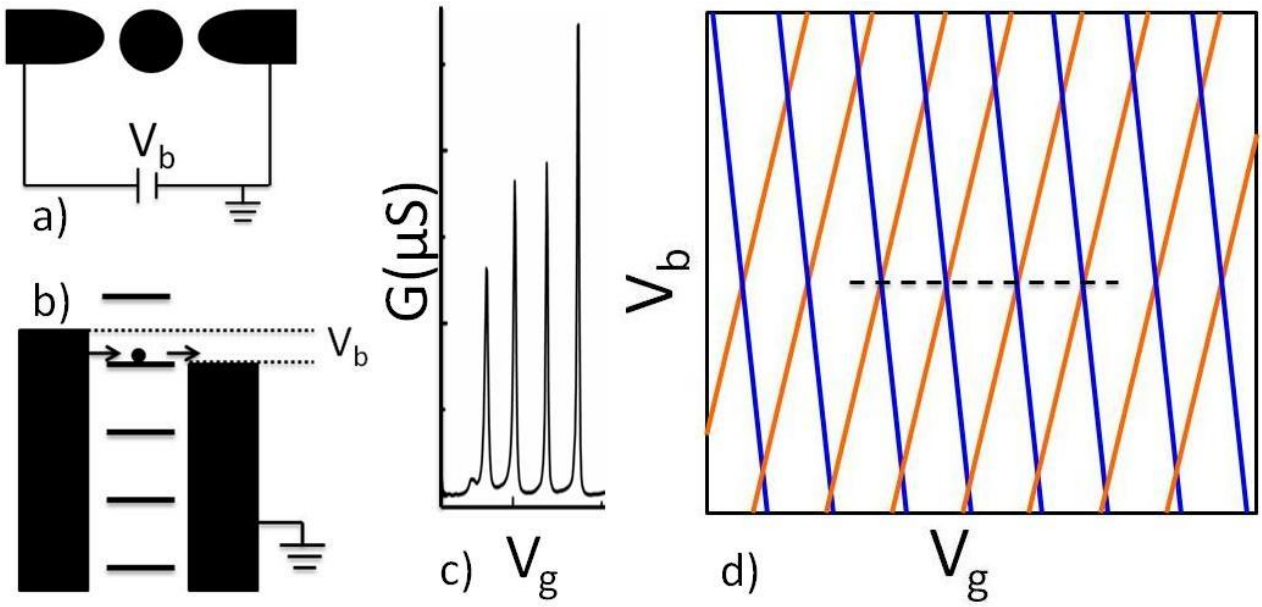

Figure 5-1: a) schematic of biased quantum dot. b) Energy level diagram of biased dot, depicting resonant tunneling through the grounded contact. c) Differential conductance versus gate voltage demonstrating four coulomb blockade peaks, as four levels are tuned though resonance with the end contacts via the gate voltage. d) Stability diagram, mapping out the position of resonant tunneling peaks as a function of bias and gate voltage. Orange lines indicate resonance with biased contact. Blue lines indicate resonance with grounded contact. Dotted line shows where a cut of the 2D plot at zero bias would show Coulomb blockade peaks, such as those in (c).

CNT quantum dots have demonstrated interesting physics such as electron-hole symmetry[40] and Kondo effects.[76] CNT quantum dots can function as single electron transistors and form the basis of prominent schemes for implementing solid-state quantum devices,[77] such as quantum current standards.[78] CNT quantum dots may be more practical than those made by other means (such as nanoparticles or GaAs heterostructures) because of the inherently small sizes and large energy scales. Like other CNT measurements, typical studies of CNT quantum dots involve tunneling between the end contacts, which is a two-terminal measurement. However, there are significant advantages to performing multi-terminal measurements, which are not as dominated by a highly-variable coupling to the leads. While multi-terminal measurements on CNTs have been demonstrated with scanned probes[60] and molecular leads,[61] lithographically fabricating probes allows for the possibility of utilizing multiple probes of varying materials. For example, superconducting probes are known to enhance spectroscopic features[79-81] and enable unusual effects such as magnetic field induced tunneling of spin polarized electrons.[19,82] Also, interesting results, such as split Kondo resonances[76], and multiple Andreev reflections[79,83,84] have been reported in two-terminal quantum dot devices with superconducting leads. Here, we present three-terminal tunneling spectroscopy measurements of a CNT quantum dot, where tunneling occurs via a lithographically fabricated superconducting probe. Evaporated contacts above or below the CNT typically create major defects in, or even cut, the tube.[44,45] As discussed below, these measurements show that our method of applying the third tunnel probe is largely non-invasive.

In the rest of this chapter, I will describe our fabrication process, then discuss low-temperature measurements of tunneling into a CNT quantum dot in which we characterize the energy spectrum of the dot. I will then discuss the observation of weak elastic and inelastic co-tunneling signals made visible by the superconducting probe. Finally, I will discuss the observation of an anomalous conduction channels that open up inside the superconducting gap when an end-to-end bias is applied.

5.2 Fabrication and Measurement*

CNTs were grown via chemical vapor deposition from lithographically defined Fe catalyst islands on a degenerately doped Si wafer having 1 μm of thermally grown oxide. Scanning electron microscopy was used to locate the CNTs, which were then contacted at both ends at device lengths of 1.7 μm. The contacts were made by e-beam evaporation of 6.5 nm of Pd at 1 Å/s followed by 30 nm of Au at 1 Å/s. The entire wafer was then coated with 12 layers or 1.2 nm of Al_2O_3 via atomic layer deposition (ALD). ALD deposition of the insulator allows for manipulation of the tunnel barrier strength via layer-by-layer thickness control, and as shown below, is gentle enough to not create substantial defects in the CNT. Finally 200-nm thick, 200-nm wide Pb tunneling probes, capped with 30 nm of In (to protect from oxidation), were patterned over the middle of the device. The probes were evaporated in a thermal evaporator at a starting pressure of 2.6×10^{-6} torr. Pb was evaporated at 1 Å/s and 72 amps. In was evaporated at 1 Å/s and 55 amps. Devices are stable at room temperature for several weeks, but the tunnel probes do not typically survive thermal cycling. Measurements were performed in a He3 cryostat.

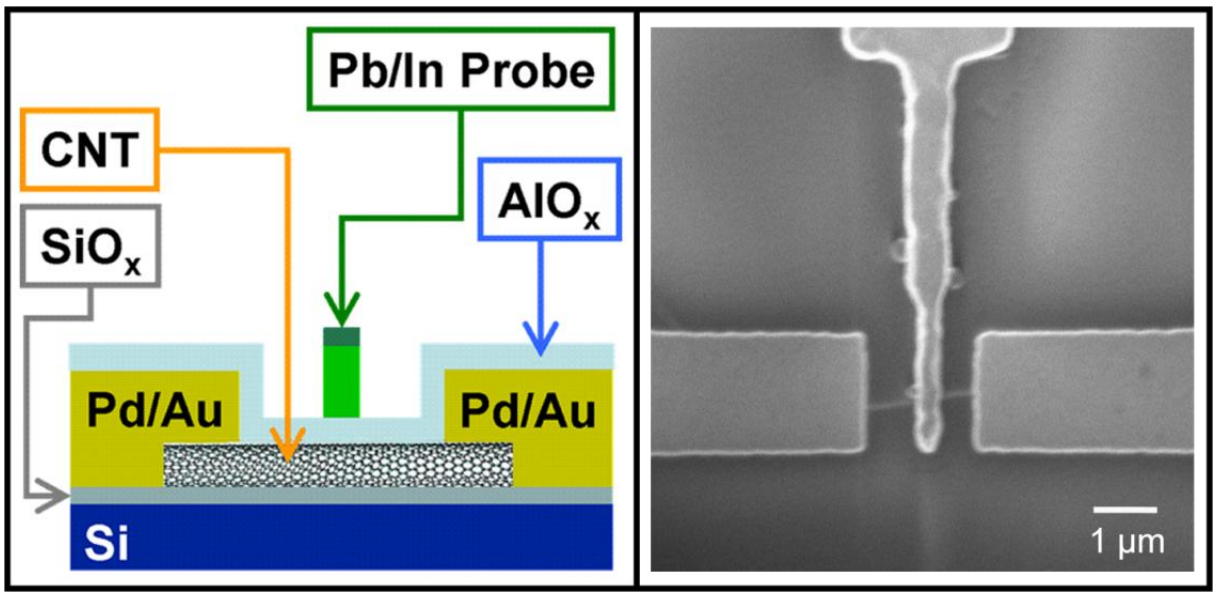

Figure 5-2: On left, side view of device geometry. On right, SEM image of a typical device.

* For details see Chapter 2. For specific deposition recipes, see Appendix 1.

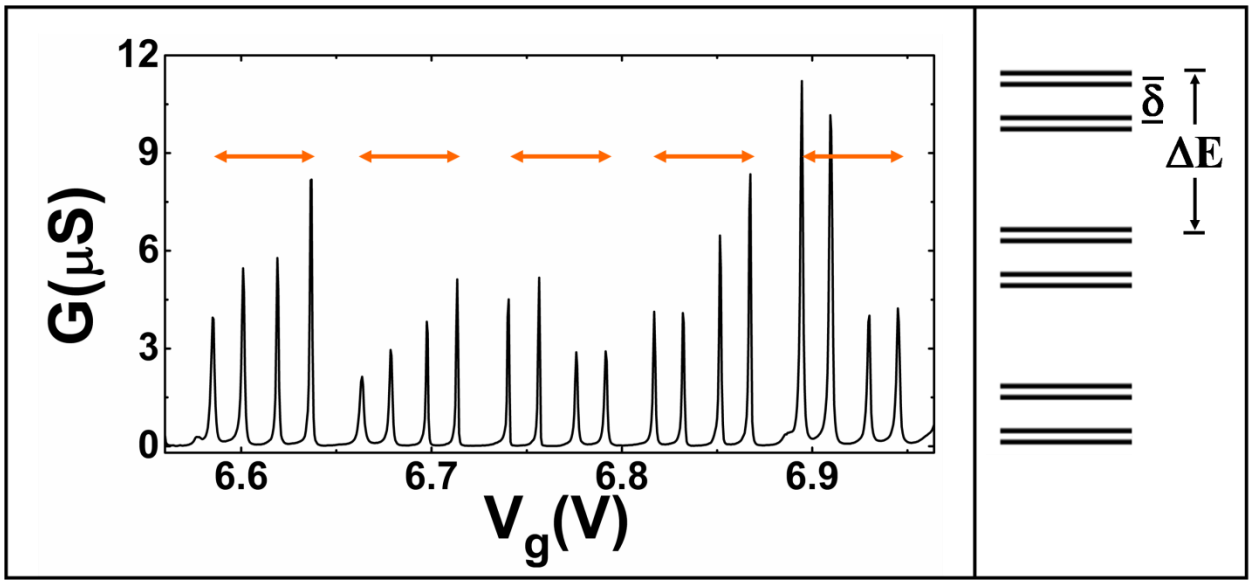

Figure 5-3: On left, end-to-end conductance as a function of back gate voltage. Each orange arrow indicated a set of 4 degenerate CNT levels. On right, expected energy level spectrum of CNT quantum dot, showing sub-band mismatch δ and energy level spacing ΔE.

5.3 Results

Conductance data show that after fabrication of the superconducting tunnel probe, the CNT remains a single, largely defect-free quantum dot. Figure 5-3, on the left, shows the end-to-end zero-bias conductance of a metallic device at 250 mK as a function of back gate voltage, V_g. The well defined Coulomb blockade peak structure occurs because of the finite energy required to add each electron to the quantum dot. The sets of four peaks, indicated by orange arrows, are a signature of four-fold periodicity in the CNT energy levels,[39,85] due to two sub-bands and a two-fold degenerate spin. The sub-band mismatch, δ, can be seen in the separation of groups of two within the sets of four peaks.[39] A schematic of the corresponding electronic energy level spectrum for a CNT quantum dot[39,40,85,86] is shown in Figure 5-3 on the right. The data show that the size of the dot is consistent with the distance between the end leads (see below). If the tunnel probe had created a significant defect in the CNT, the spacing of the Coulomb blockade peaks—particularly the four-fold periodicity[86]—would have been much more irregular.[44]

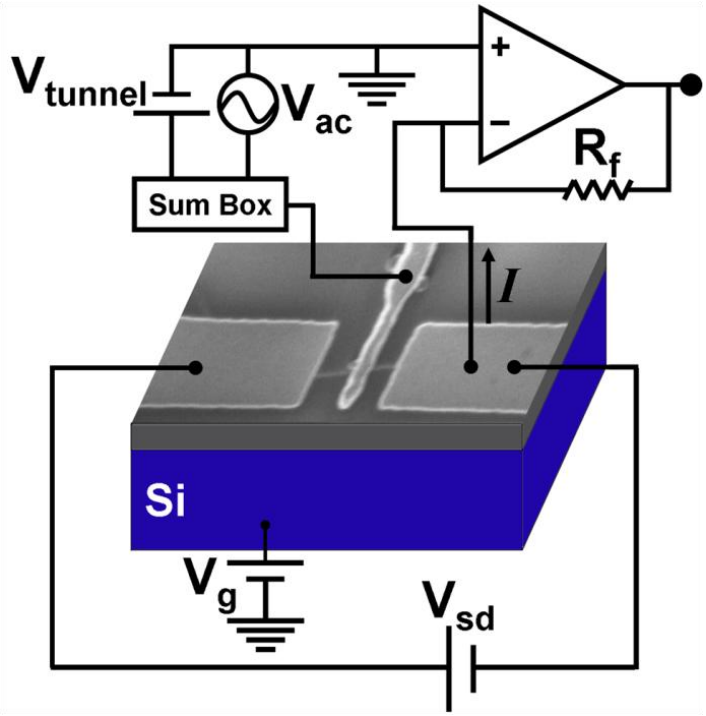

Figure 5-4: SEM image of a typical device, with diagram of the measurement circuit.

The measurement setup for conductance through the superconducting probe is shown in Figure 5-4: a DC voltage, V_{tunnel}, with an AC excitation, V_{ac}, was applied between the superconducting tunnel probe and one end contact, and the resultant current was read out through a current preamplifier, into a lock-in amplifier. A gate voltage, V_g, could be applied to the back of the silicon substrate while a floating bias voltage, V_{sd}, could be applied from end-to-end of the CNT. Figure 5-5 shows the tunneling conductance as a function of V_{tunnel} and V_g at $V_{sd} = 0$. The Coulomb diamond structure is similar to what has been previously observed,[39,40] with the striking exception of a zero conductance stripe that splits the diamond pattern and is consistent with the Pb superconducting gap, $2\Delta \sim 2.6$ meV. The clarity of the gap indicates a high-quality tunnel junction. The usual "closed" diamond pattern is evident when the superconducting probe is made normal with a magnetic field, as shown in Figure 5-6. It is also evident in Figure 5-5 that the tops and bottoms of the diamonds are offset; this is because the tunneling probe also has a gating effect.*

* We also see a weak offset between the top and bottom vertices of the end-to-end diamonds due to source-drain capacitance

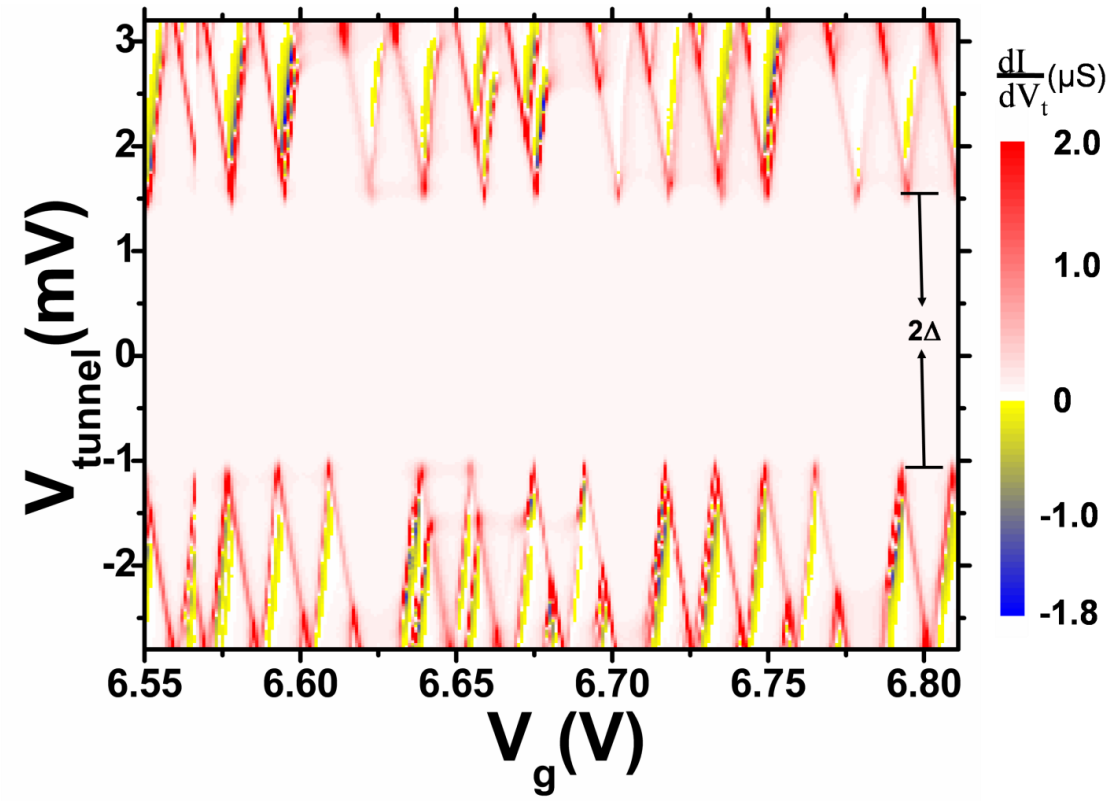

Figure 5-5: Differential conductance between the superconducting tunnel probe and an end lead as a function of tunnel bias and back gate voltage (with end-to-end bias Vsd=0). The Pb superconducting gap, Δ, is labeled. Areas of negative conductance are evident in yellow to blue.

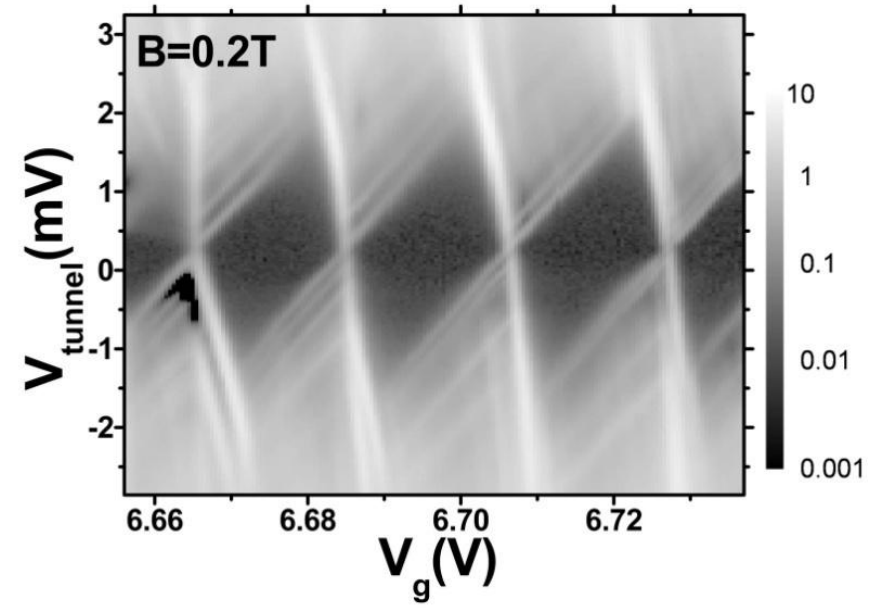

Figure 5-6: Measurement similar to Figure 5-5, but with an applied magnetic field, showing the usual "closed" diamond pattern when the superconducting probe is made normal with a magnetic field.

The data in Figure 5-5 show four-fold periodicity similar to the end-to-end zero-bias conductance in Figure 5-3. The resonant tunneling lines with positive and negative slopes that make up the Coulomb diamonds correspond to energy levels in resonance with the density of states (DOS) at the superconducting probe's gap edges and the Fermi energy of the end leads, respectively. The data is consistent with the expected stability diagram, shown in Figure 5-7. While resonant tunneling lines make up the diamonds, excited states are also visible (denoted by red stars in Figure 5-7); these are due to conduction through an additional energy level, separated from the first by the band mismatch, as the tunnel bias is increased.

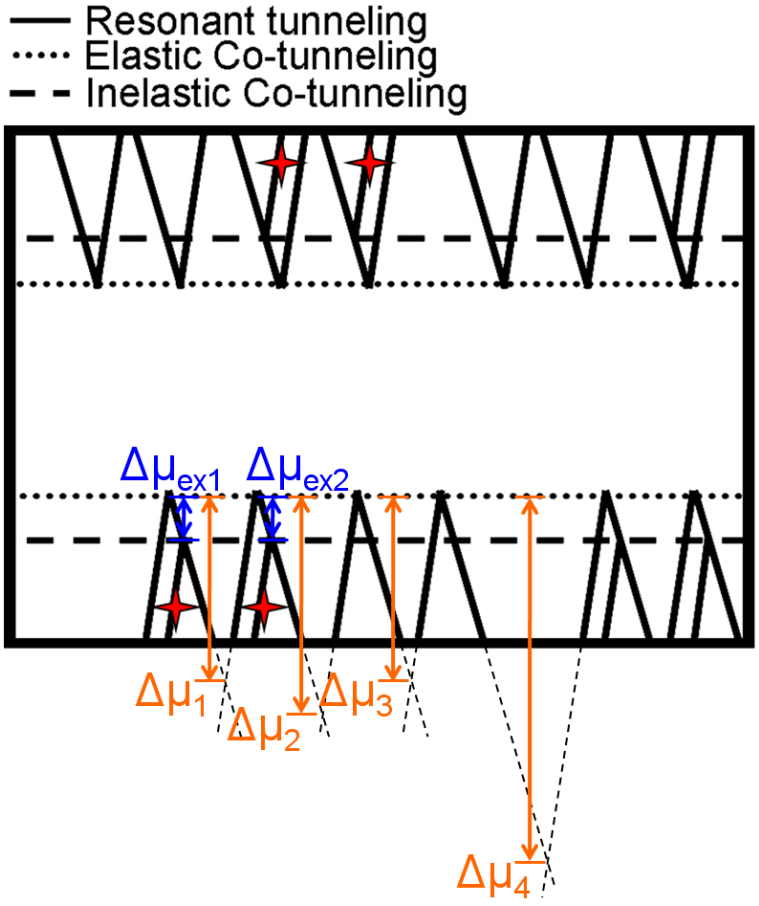

Figure 5-7: Expected stability diagram. Red stars indicate excited states. Orange and blue labels addition energies. The addition energies $\Delta\mu_x$ are the additional energy needed to add another electron to the dot when there are x electrons in the shell already. $\Delta\mu_{ex1}$ and $\Delta\mu_{ex2}$ are the first and second excitation energies and represent the amount of energy needed to excite an electron to the nearest empty energy level.

Interestingly, the band mismatch can change drastically between adjacent sets of four levels. In the four sets of degenerate levels seen in Figure 5-5, the band mismatches are: $\delta_1 \sim 0.25$ meV, $\delta_2 \sim 0.50$ meV, $\delta_3 \sim 0.175$ meV, and $\delta_4 \sim 0.125$ meV. Thus one can tune the band mismatch with gate voltage. This conclusion is consistent with the idea that the band mismatch occurs because of substrate interactions, which can likely be tuned with gate voltage. We also observe negative differential conductance, here in blue and yellow, in the lines corresponding to resonance with the superconducting probe (positive slope) but not in those corresponding to resonance with the normal metal contact (negative slope). Negative differential conductance has been observed in other CNT/superconductor systems.[79,87]

In addition to good qualitative information, quantum dot tunneling spectroscopy also allows for quantitative measurement of important characteristics of the dot. The low energy spectrum of a CNT QD can be characterized by five parameters: the Coulomb charging energy U, the energy level space ΔE, the band mismatch δ, the exchange energy J, and the excess Coulomb energy dU. The addition energies, $\Delta\mu_n$, is the required change in chemical potential when adding the N+1 electron to a QD which contains N charges. These addition energies and therefore the five physical parameters, reveal themselves in the filling of the four degenerate levels, made visible in the tunneling spectroscopy. Theses addition energies are depicted in Figure 5-7. In terms of the physical parameters mentioned above:

$$\Delta\mu_1 = \Delta\mu_3 = U + dU + J$$

$$\Delta\mu_2 = U + \delta - dU$$

$$\Delta\mu_4 = U + \Delta E - \delta - dU$$

$$\Delta\mu_{ex1} = \delta$$

$$\Delta\mu_{ex2} = \delta - J - dU$$

There are basically two ways to fill the four shells, the difference lies in what happens when there are two electrons on the dot.[39] (see Figure 5-8) If $\delta > dU + J$, then the lower energy, spin-degenerate orbital state fills first. This is called the singlet state, and has total spin = 0. If

$\delta < dU + J$, the ground state has both electrons of the same spin, and occupying different orbital levels. This is called the spin triplet state and has a total spin of 1.[88]

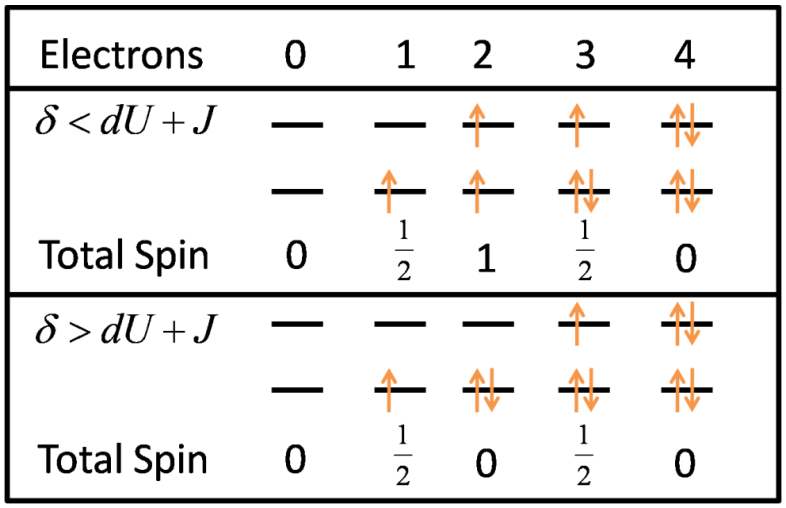

Figure 5-8: Two possible methods of filling the four degenerate levels of a CNT quantum dot. Each line represents two spin degenerate levels. The lines are separated by the band mismatch.

We will now examine a set or peaks in detail. Figure 5-9 is on a log scale to allow a larger dynamic range. We will discuss the weak features below, but for now focus on the set of four peaks on the left side. First notice that $\Delta\mu_{ex1}=\Delta\mu_{ex2}$ within the resolution of the measurement. This shows conclusively that $\delta \gg dU + J$, and therefore our dot fills according to the spin singlet pattern indicated in the lower part of Figure 5-8, S=0,1/2,0,1/2,0. This filling pattern is also evident in the amplitude of the resonant tunneling lines. Notice the bright-dark-bright-dark pattern in the points of the upper triangles made up of the resonant lines from right to left. In the first resonant peak the electron is conducting through two spin degenerate levels resulting in a bright, high conduction peak. In the next triangle, one of the two lower spin degenerate levels is filled and conduction occurs through the other resulting in a dimmer peak. In the third triangle, both of the lower energy orbital levels are full, and conduction is through the top two spin degenerate levels, again resulting in a bright peak. Finally in the fourth triangle, only one level is left empty for conduction, so the peak is again dim. One can see the same pattern in reverse in the lower peaks as the levels are scanned through in the opposite direction at negative bias.

One can use the diamond structure in Figure 5-9 to characterize the quantum dot.[39,60] In Figure 5-9 the tops and bottoms of the Coulomb diamonds are cut off. In calculating the

following results the resonant lines that make up the Coulomb diamonds were fit and their intersections calculated to find the tops and bottoms of the diamonds. As mentioned above, $\mu_{ex1}=\mu_{ex2}$ within the resolution of the measurement, so the five equations collapse to three: $\Delta\mu_1 = \Delta\mu_3 = U$, $\Delta\mu_{ex1} = \Delta\mu_{ex2} = \delta$ and $\Delta\mu_4 = U + \Delta E - \delta$. Thus we find the charging energy is U ~ 2.1 meV. Charging energy is related to total capacitance, $C_\Sigma = e^2/U \sim 80$ aF. The band-mismatch is δ ~ 0.4 meV and the quantum dot level spacing is ΔE ~ 1.6 meV. The level spacing is close to that estimated by quantized energy spacing $\Delta E = h v_F/2L$ ~ 1.2 meV for a 1.7 μm long CNT.[39] The lead capacitances can also be determined from the slopes of the resonant lines. We find the CNT-backgate capacitance C_g ~ 5.0 aF, the CNT-tunnel probe capacitance C_{tunnel} ~ 53 aF, and the CNT source plus drain capacitance C_{sd} ~ 22 aF.

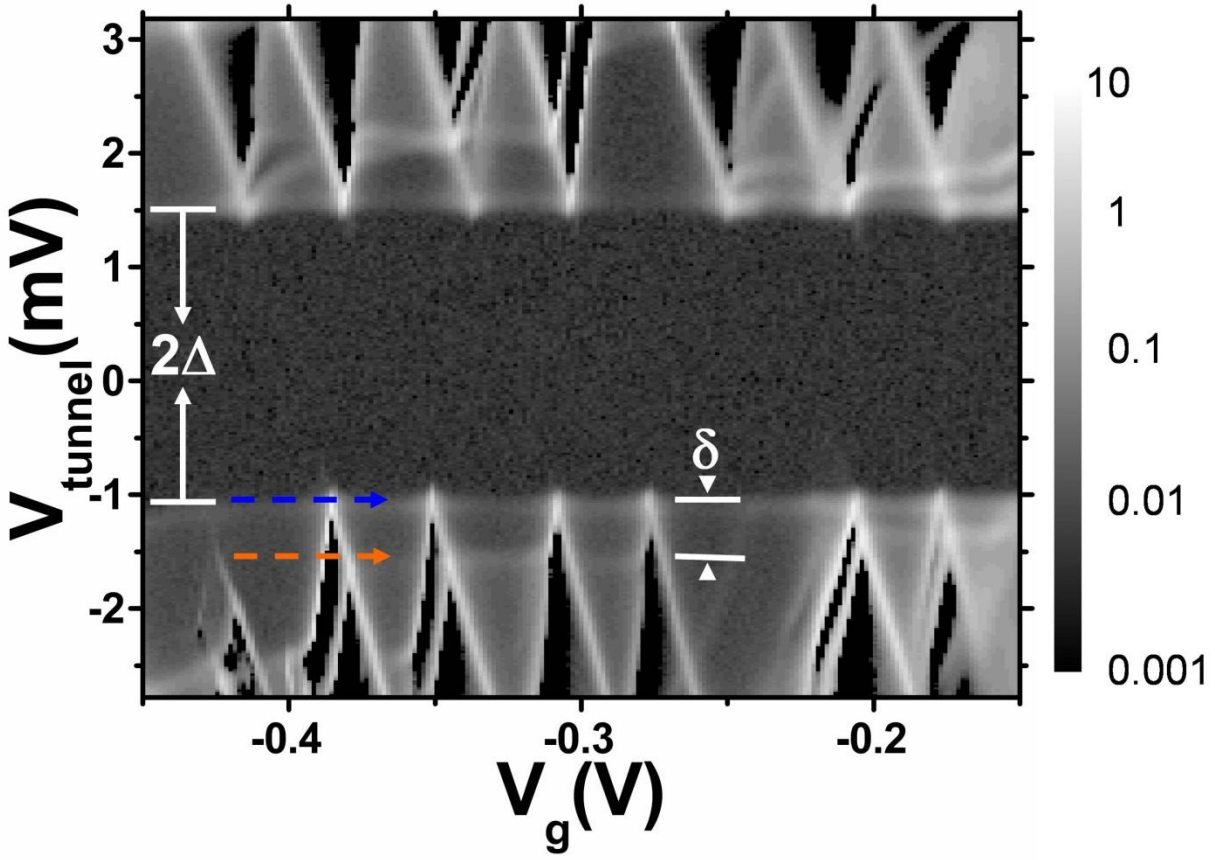

Figure 5-9: Differential conductance between the superconducting tunnel probe and an end lead as a function of tunnel bias and back gate voltage (with end-to-end bias Vsd=0). The Pb superconducting gap, Δ, and the band mismatch, δ, are labeled. Blue and orange arrows point to signals of elastic and inelastic co-tunneling, respectively.

Tunneling via a superconducting probe allows us to observe large enhancements in conductance near the superconducting gap edge. This occurs because the normalized superconducting DOS, $n_s(E) \sim \mathrm{Re}[|E|/(E^2-\Delta^2)^{1/2}]$, is a sharply peaked function that effectively magnifies the tunneling current. In particular, we are able to observe both elastic and inelastic co-tunneling processes (blue and orange arrows in Figure 5-9), which, in this case, are invisible when using a normal metal probe. Co-tunneling events are higher-order tunneling processes that involve the simultaneous tunneling of multiple electrons to transfer one electron, or one Cooper pair across the dot. Hence the process was first dubbed *q*-MQT or macroscopic quantum tunneling of charge[89,90], in reference to the much studied φ-MQT.[91-93] The transfer of one electron through the dot is a macroscopic quantum tunneling event because it requires a coherent excitation of the whole charge of the quantum dot. In the case of co-tunneling, the tunneling electron polarizes the dot in energetically forbidden virtual states, such that the Coulomb energy is given by normal macroscopic electrostatics. This implies that all free electrons on the dot must coherently evolve through the tunneling process together. So it is argued that co-tunneling is not just the tunneling of an electron across the dot, but of the macroscopic variable of the dot's charge, *q*.[90] Macroscopic quantum tunneling systems are believed to be crucial in understanding the quantum measurement problem of Schrödinger's cat paradox. By studying larger and larger systems that display quantum coherence, it is hoped to establish whether or not there is a kind of break between the macroscopic and microscopic world, past which quantum mechanics no longer applies.[94] In addition to their fundamental importance, understanding of *q*-MQT, or co-tunneling, events is crucial to the design of single electron transistors and schemes that depend on them. These schemes rely on the first order tunneling properties of CNT quantum dots; co-tunneling constitutes an error. In fact, in the processor industry co-tunneling is just another ignoble source of leakage current.

Co-tunneling events are further distinguished by their energy requirements. Elastic co-tunneling, which leaves the dot in the same state, dominates at low bias and results in a conductance peak when the Fermi levels of the two contacts are aligned. With a superconducting lead, this happens when the Fermi level of the normal lead is aligned with the superconducting gap edge, yielding enhanced peaks at $V_{tunnel}=\pm\Delta/e$ (see Figure 5-10). Note that with normal leads, elastic co-tunneling is a very low/zero bias phenomena, making it very hard to observe. The superconducting probe enhances the visibility of this process, not only because of its divergent

density of states, but also because it moves the onset of elastic co-tunneling to a finite bias voltage, namely the superconducting gap energy Δ. Inelastic co-tunneling, which leaves the quantum dot in an excited state, only occurs when the bias is greater than the energy needed to put the dot in the first available excited state. Thus we see enhanced inelastic co-tunneling conductance peaks when $V_{tunnel} = \pm(\Delta+\delta)/e$ (see Figure 5-10).

Shell filling is also crucial in understanding the co-tunneling evident in Figure 5-9. Notice that the elastic co-tunneling line is present at all gate voltages, but the inelastic co-tunneling line is not seen between sets of four peaks. Figure 5-10 illustrates the relevant co-tunneling processes. As indicated in the parts a and e, inelastic co-tunneling is not possible without a partially full set of levels.[79] This means that elastic co-tunneling could be the harder SET error to deal with, since inelastic co-tunneling can be simply gated away.

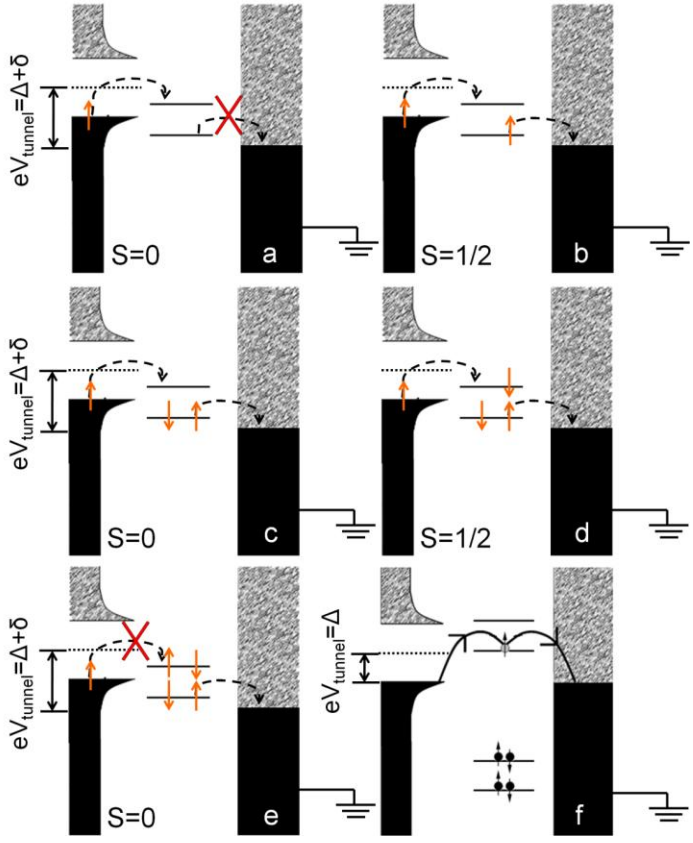

Figure 5-10: Schematic of possible co-tunneling processes. a-e. illustrate co-tunneling processes appropriate to the shell filling indicated. Note that inelastic co-tunneling is not possible without a partially full set of levels. Note that this is consistent with Figure 5-9. Part f is one of the possible elastic co-tunneling processes.

The transition to the inelastic regime can be sharper than the characteristic lifetime broadening of the QD states,[95] and can thus be used to get a more accurate measurement of δ than would be possible from the resonant tunneling lines. The amplitudes of co-tunneling processes also have important implications for the error rates of devices such as single electron transistors,[95,96] and set a limit on the accuracy of metrological devices.[78,97] While weak inelastic co-tunneling has been previously observed in CNTs, [39,85] weak elastic co-tunneling in CNTs has only recently been seen in a two terminal device with superconducting leads.[79] The robust signals that we see allow us to measure the elastic and inelastic co-tunneling currents near V_{sd} = 0 as $I_{el\text{-}co}$ ~ 3.7 pA and $I_{in\text{-}co}$ ~ 11 pA, respectively. The corresponding electron co-tunneling rates are $\Gamma_{\text{el-co}} = I_{el\text{-}co}$ /e ~ 2.3x10^7 s^{-1} and $\Gamma_{\text{in-co}} = I_{in\text{-}co}$/e ~ 7x10^7 s^{-1}. While the magnitudes of the tunneling rates depend on the DOS of the leads, the ratio of elastic to inelastic tunneling should be independent of the leads.[96] Notably, when the tunnel probe is made normal by a magnetic field (See Figure 5-6 on the right) we do not see any co-tunneling features in the Coulomb diamonds.

In addition to the observation of enhanced spectroscopic features, the three-terminal measurement allows us to directly determine the effect of end-to-end bias on the quantum dot spectrum. While it is has been predicted that the bias will not affect the spectroscopy, this has not been directly proven before. Part a of Figure 5-11 shows tunneling differential conductance from the superconducting tunneling probe to the CNT on a log scale as a function of V_{tunnel} and V_g while V_{sd} = 0.8 mV is applied across the ends. The features are similar to those for V_{sd} = 0 (see Figure 5-9), which indicates that the energy spectrum of the dot is largely unchanged. However, another set of peaks, separated by the Pb gap energy but offset by V_{sd}, also appears (see red lines in part b of Figure 5-11). These additional conduction lines show up when energy states of the CNT align with the Fermi level of the left end contact at $E = -eV_{sd}$,[98] demonstrating that the end-to-end bias can be spectroscopically determined. The resonant tunneling to both end leads through the same energy level is separated by V_{sd} in the vertical direction and $(C_\Sigma/C_g)V_{sd}$ in the horizontal direction, where C_Σ is the total capacitance of the nanotube. From this we find C_g ~ 6.4 aF, which agrees well with the value from the slopes of resonant tunneling lines.

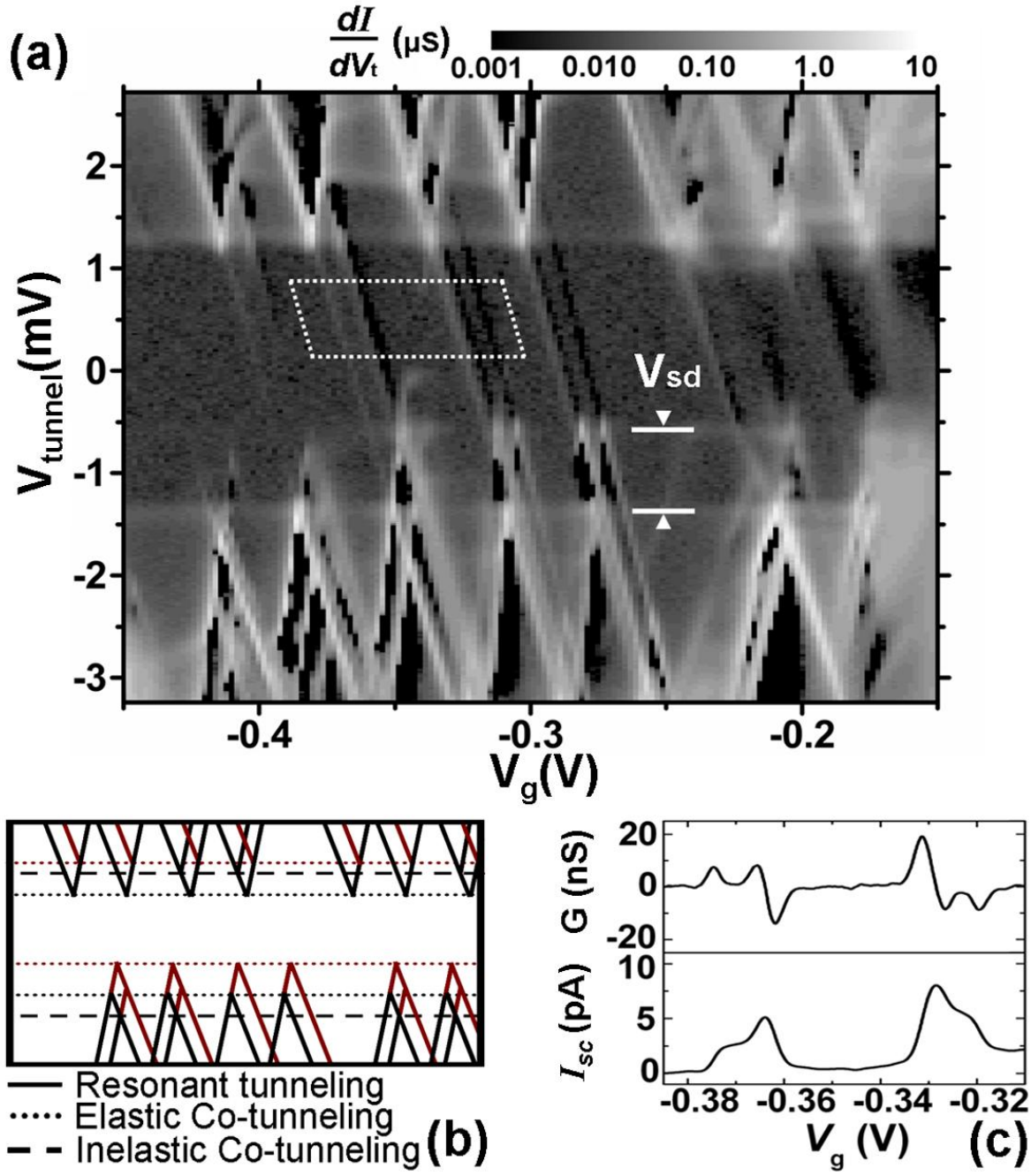

Figure 5-11: a) Differential conductance between the superconducting tunnel probe and an end lead as a function of tunnel bias and back gate with V_{sd} = 0.8mV applied between the end leads. Dotted box indicates data used in (c). Smeared diamonds on the right are due to a lowering of the lead tunnel barriers with gate voltage (an open dot regime). b) expected stability diagram. Red lines show new features expected at finite source-drain voltage. c) horizontal cut through some of the features inside the gap in (a), with data averaged over bias range within dotted box to minimize noise, showing conductance (top) and derived current (bottom) inside the gap (cut shown on linear scale, since negative signals were shown as zero in log plot).

When a bias is applied across the ends of the CNT we observe conductance inside the superconducting gap when the levels of the CNT are aligned with the end contacts (see part c of Figure 5-11), even though V_{sd} = 0.8 mV is smaller than the gap energy of ~ $2\Delta/e$ = 2.6 mV. The conductance in the gap is surprising since it should be suppressed exponentially,[99] and is not observed when V_{sd} = 0 (see Figure 5-9). It is possible that a finite source-drain bias across the tube enhances the inelastic scattering of electrons, creating excited electrons and holes that can tunnel above and below the gap, respectively, and thus create a non-zero tunnel current, I_{sc}. From part c of Figure 5-11 we find I_{sc} ~ 4 - 6 pA, which sets a lower bound on the inelastic scattering rate Γ_{in} of $\Gamma_{in} > I_{sc}/e \sim 2.5\text{x}10^7 - 3.78\text{x}10^7$ s^{-1}. This scattering rate is typically estimated experimentally via level broadening, which often only gives an upper bound because of thermal broadening effects. The mechanism for the enhanced scattering remains unknown and will be investigated in the future.

5.4 Conclusion

In summary, we have described the fabrication and measurement of a device consisting of a noninvasive superconducting tunnel probe over the middle of a clean, contacted CNT quantum dot. The use of a superconducting probe enhanced tunneling signals, and spectroscopy using this three-terminal device allowed the effects of bias to be determined. These results open the door to a better understanding of the mechanisms behind weak, second-order processes in systems like CNT quantum dots, and allow for a better assessment of such systems' use in practical devices, like single electron transistors, quantum current standards, and quantum qubits. All of these schemes take advantage of the systems' unusual first order tunneling properties, namely the Coulomb blockade, with the second order co-tunneling process being errors. In the future we hope to measure similar devices to try and understand the subgap anomalous subgap conductance. In particular, the fact that this conductance is only visible with an applied voltage is tantalizing and implies that it may be related to inelastic scattering. We would like to measure the dependence of these conduction channels on the applied end-to-end bias.

Chapter 6
Superconducting Tunneling Spectroscopy of a Graphene Sheet

6.1 Introduction

Graphene is a zero-gap two-dimensional semiconductor having high mobility and potential for commercial applications.[100] Its unique electronic structure—particularly quasi-particles that behave as massless Dirac fermions—has also led to the discovery of new physics such as an anomalous quantum Hall effect and the observation of Klein tunneling[101,102]. Interesting physics has been observed in superconductor graphene systems, including gate dependence, proximity induced supercurrents in graphene having high transparency superconducting contacts,[103,104] and, Multiple Andreev reflection in superconductor-graphene-superconductor junctions.[105] However, measurements using superconducting tunnel probes have not been reported. Superconducting probes are known to enhance spectroscopic features[79-81], and enable measurements of properties such as densities of states, electron energy distribution functions[59,98], and phenomena such as spin-polarized tunneling[19,82].

Here we report results on superconducting tunneling spectroscopy of a graphene sheet. We have fabricated single- and multi-layer graphene devices having both normal-metal Ohmic contacts and superconducting tunnel probes. Just outside the superconducting gap region we observe conductance oscillations as a function of bias and gate voltage, possibly due to electron

phase interference between the end contact and probe interfaces. These oscillations are suppressed by a magnetic field. Unexpectedly, we also observe structure inside the superconducting gap, particularly two distinct and symmetric peaks whose positions evolve with gate voltage, and which are not suppressed by a magnetic field.

In this chapter I will first discuss fabrication of the graphene devices studied here. I will then discuss the observation of quantum interference oscillations outside the SC gap, followed by discussion of anomalous conduction peaks inside gap. Finally I will discuss a hypothesis that explains the subgap features as resonant conductance though Andreev bound states in a quantum dot that forms between the SC and insulator or in the graphene underneath the SC. We are able to resolve the energy of these bound states and this may be evidence for a novel type of bound-state spectroscopy.

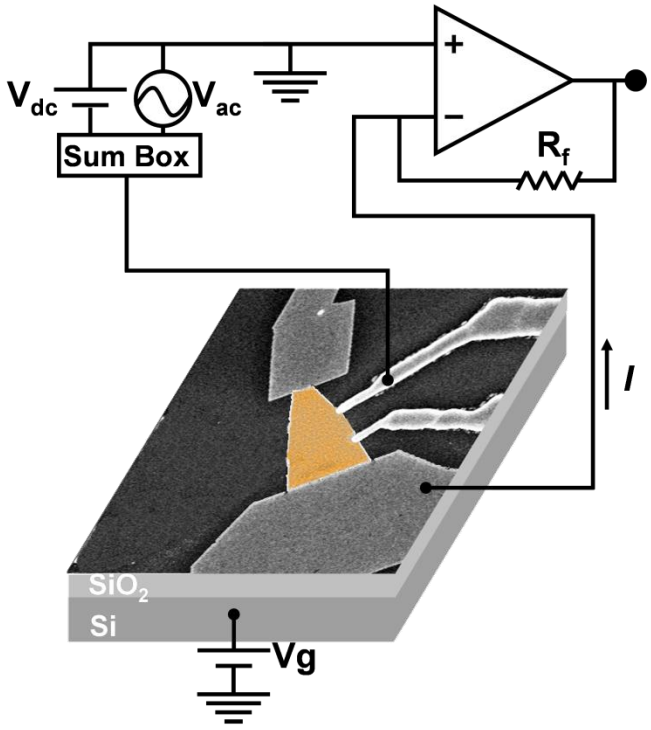

Figure 6-1: False color SEM Image of typical device with Cr/Au end contacts and two superconducting tunnel probes. The device is overlaid with tunneling spectroscopy measurement circuit.

6.2 Sample Preparation and Measurements

The graphene samples were mechanically exfoliated onto highly doped Si substrates capped with 300 nm SiO_2. The graphene thickness was determined by the color variation in optical microscopy, Raman spectroscopy, and atomic force microscopy. The data discussed in this dissertation is taken from one multilayer device (~ 10 layers) and one single layer device, though similar data was taken on two other single layers devices and one bilayer (five out of six measured samples showed the effects discussed below). The devices consist of four electrodes on a piece of graphene (see Figure 6-1). The two large end leads are Cr/Au and the narrower middle probes are Pb/In. The end electrodes were patterned by conventional electron beam lithography and electron beam evaporation of 2 nm Cr and 50 nm Au. The chips were then annealed in H_2 and Ar at 300C for 2 hours to clean surface residue. The devices were then covered in 12 layers AlO_x via Atomic Layer Deposition, and the 200 nm wide superconducting probes to the middle were patterned by conventional electron beam lithography and thermal evaporation of 200 nm Pb and 30 nm In. The tunneling resistances through the superconducting probes, R_{tunnel} ~ 200 – 500 KΩ, are typically 10-100 times larger than the graphene's end-to-end resistances, $R_{end\text{-}to\text{-}end}$ ~ 5 – 20 KΩ.

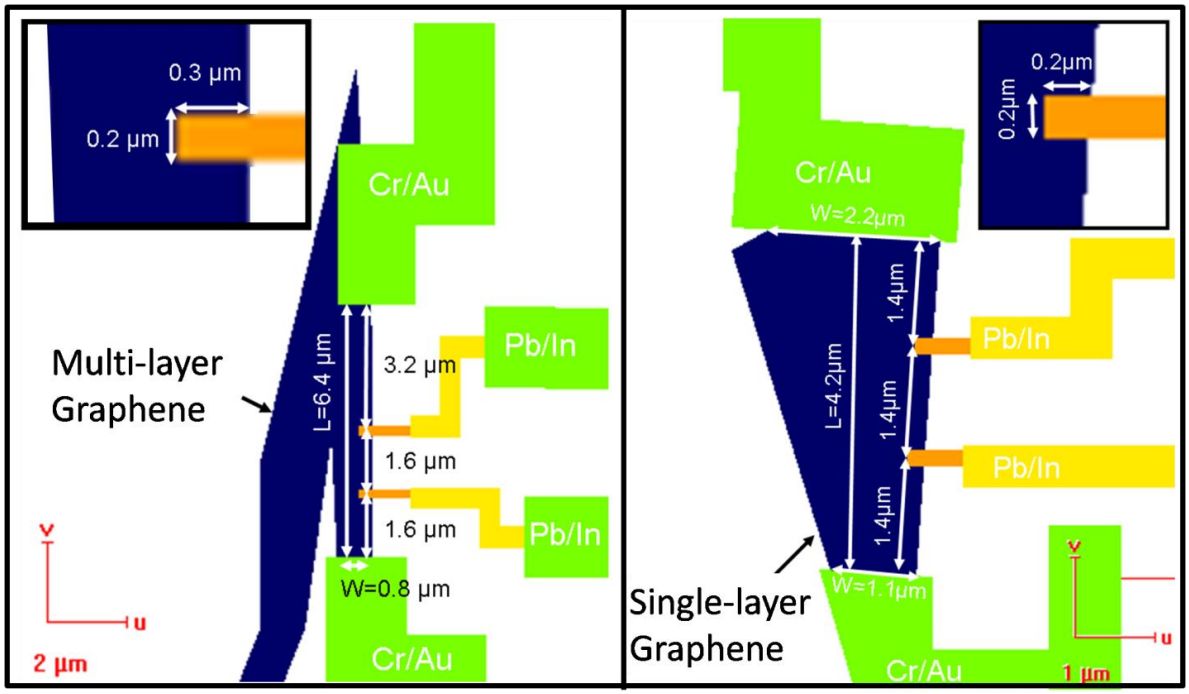

Figure 6-2: Image of Cad design for the two devices, sample B on left, sample A on right, presenting various device dimensions.

The geometry of the presented devices is labeled in Figure 6-2. For the single layer device, Sample A, the distance *L* between the two longitudinal electrodes and the width *W* of the sample are ~ 4.2 μm and 1.5 μm, respectively. The size of the superconducting probe junction with graphene is 0.2 by 0.2 μm. For the multi layer device, Sample B, the distance *L* between two longitudinal electrodes and the width *W* of the sample are ~6.4 μm and 0.8 μm, respectively. The superconducting probe junction with the Graphene is 0.3 by 0.2 μm. The multi layer device is about 10 layers thick.

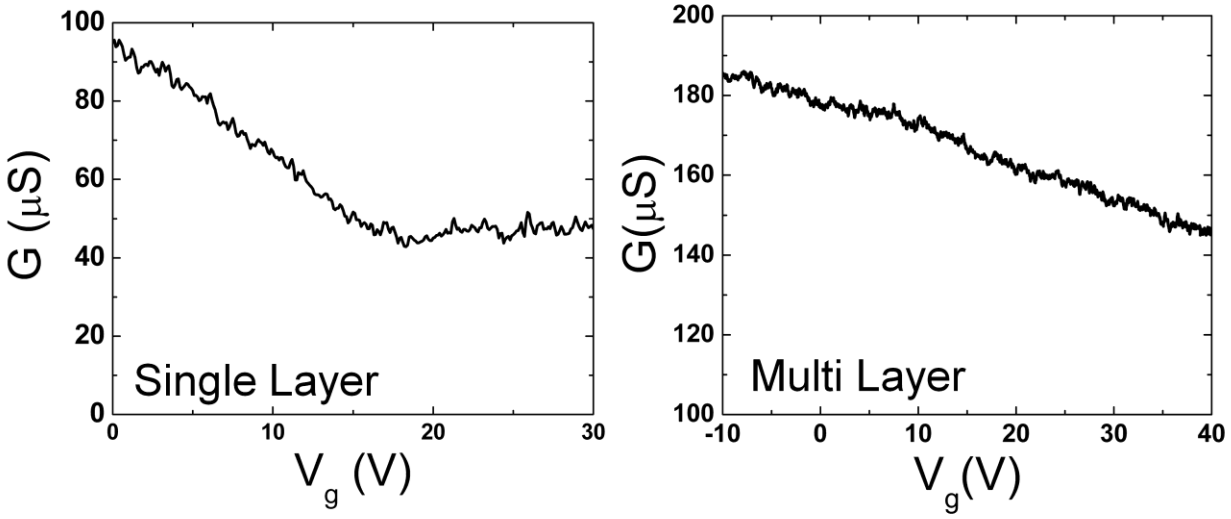

Figure 6-3: On the left, gate sweep of end-to-end device conductance for single layer sample A displaying Dirac cone. On the right, gate sweep of end-to-end device conductance for multi-layer sample B.

Measurements were performed in a Helium-3 cryostat using standard ac lock-in techniques. The measurement set-up is shown in Figure 6-1. To characterize the samples, end-to-end conductance was measured as the back gate (the degenerately doped wafer) potential was varied. As can be seen in Figure 6-3, the single-layer graphene shows an asymmetric Dirac point at V_g ~ 17.5 V. The asymmetry is expected from the large invasive evaporated end contacts and are caused by pinning of the charge density below the metal, forming p-n or p-p junctions depending on the polarity of the carriers in the bulk graphene.[106] The multi-layer sample does not show a Dirac point within the range measured; this is not unexpected, as the gate dependence is typically weak in multi-layer samples. In all cases the Dirac point was far offset to on the positive gate side, greater than 20 volts due to doping from the insulating layers above and below the graphene

sheet. The samples are also likely disordered due to the sandwiching insulating layers and show clear signals of weak localization in magnetoresistance measurements[107]. Tunneling differential conductance measurements were performed by applying a sum of dc bias voltage V and ac excitation voltage V_{ac} to the superconducting tunnel probe, and a voltage V_g to the back gate, while measuring the current I at one of the graphene end contacts as illustrated in Figure 6-1.

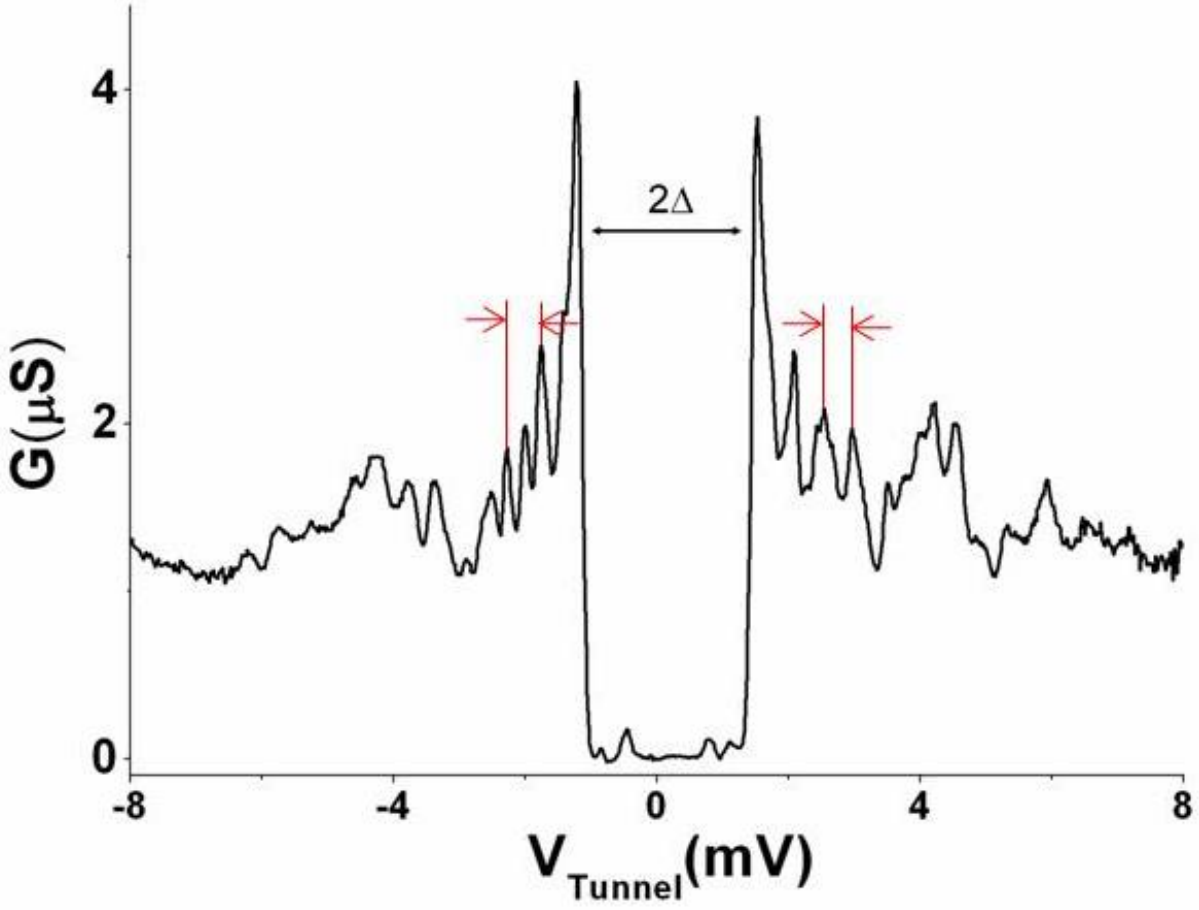

Figure 6-4: : Conductance versus tunnel probe bias voltage in the Sample B measured over the 3.2 μm gap between the top probe and top contact, shown on the left of Figure 6-2. Large conductance oscillations outside the gap that fall off at high bias can be understood as Fabry Perot type interference between the tunnel probe and the end contact. This behavior is present in all measured samples. The two gaps defined by the red arrows is the same size. We could be observing both two bounce and four bounce interference paths.*

* Note: there is an unphysical offset of about 0.25 mV in the bias voltage from an offset in the sumbox in all the data. This is a fairly common occurrence in powered voltage sources.

6.3 Results and Discussion

Figure 6-4, shows the overall shape of the conductance through the tunnel probe to one end contact as a function of DC tunnel probe bias. As expected from the superconducting DOS of Pb there is a prominent gap of $2\Delta = 2.6$ eV flanked by strong superconducting peaks and oscillatory conduction that tapers off at high bias. While we do observe features inside the superconducting gap, between those features we observe a hard zero conductance gap (this is best observed in the black curve of Figure 6-12). The well formed superconducting gap indicates that there is a good tunnel barrier, free of leakage or significant defects between the tunnel probe and graphene.

Oscillations in conduction are also apparent: these have the largest amplitude near the superconducting peaks and grow smaller, eventually disappearing at high bias. These oscillations appear in both single and multi layer samples. It is possible that these oscillations are Fabry-Perot like quantum interference which has been seen in graphene heterojunctions.[102] We can extract a length scale from the period of oscillation and compare it to the size of the device. However, this is complicated by the fact that the oscillations are irregular in period. For example, the gap defined by the red arrows on the right of Figure 6-4 is 0.48 meV. This implies a length of $L = hv_f/2\Delta E \sim 3.3$ μm (where ΔE is the peak to peak energy spacing and the Fermi velocity is 7×10^5 m/s) which is consistent with the space between the top probe and top contact in shown on the left of Figure 6-2. However, in the gap defined by the red arrows on the left of Figure 6-4 there are two oscillations with a period of 0.24 meV, and an implied length of ~6.7 μm. It is possible that this oscillation corresponds to interference in a path that goes down and back twice, a 4-bounce path. If this is the explanation for the oscillations, it is not clear why the "4-bounce" interference is roughly the same amplitude as the "2-bounce", which one might expect to dominate. As seen on top of Figure 6-5, while the superconducting peak height decreases significantly with temperature, the oscillation amplitude decreases less drastically. This is in sharp contrast to the bottom of Figure 6-5 in which the oscillations are quickly suppressed by an applied magnetic field. In Figure 6-6 a 2D plot of tunnel probe conductance vs. tunnel probe bias voltage vs. backgate voltage shows the gate dependent nature of the interference fringes, which is consistent with the interpretation that these are Fabry Perot oscillations and indicates that this is phenomena which occurs in the graphene.

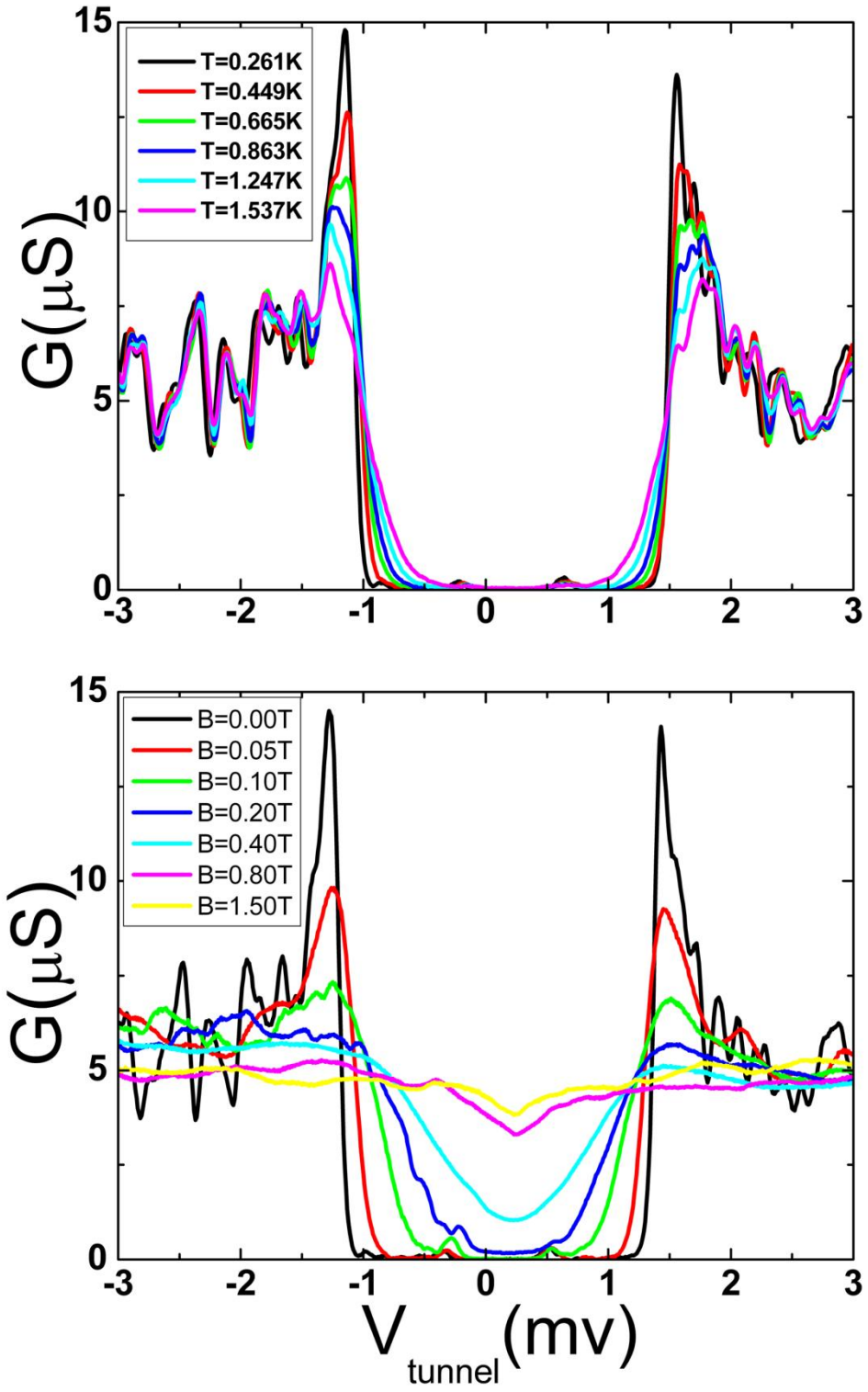

Figure 6-5: On top, tunnel probe conductance versus bias voltage showing superconducting peak and interference fringes at varying temperatures. On bottom, tunnel probe conductance versus bias voltage showing superconducting peak and interference fringes at varying magnetic fields.

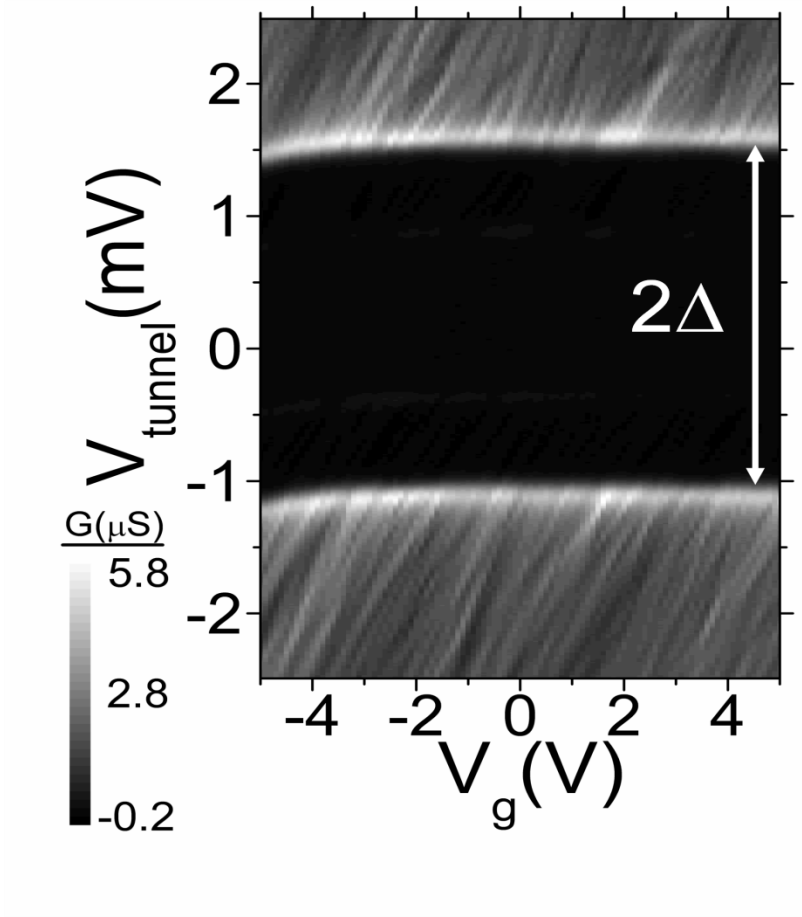

Figure 6-6: 2d plot of tunnel probe conductance versus bias voltage versus back gate voltage showing gate dependent nature of the interference fringes.

Anomalous subgap peaks are observed inside the superconducting gap, as seen in Figure 6-8 and Figure 6-9 (Figure 6-7 is the raw data used for Figure 6-8). These peaks occur in a region where conduction should be energetically suppressed. They are symmetric about zero bias and the gap between them varies with gate voltage. Figure 6-8 and Figure 6-9 show 2D maps of conductance through the tunnel probe on a log scale for the single and multi-layer sample respectively. The vertical axis is the DC tunnel probe bias voltage. The horizontal axis is the DC gate voltage. The wide horizontal band of low conductance labeled 2Δ is the superconducting gap of the tunnel probe. It appears that a conduction channel is opened outside the subgap peaks as interference fringes are observed extending into the gap until they are extinguished at the subgap peak. Notice that the distance between the subgap peaks changes with gate voltage. As one might expect, this gate dependence is much stronger in the single layer sample then in the

multi layer, likely because of screening from the lower graphene layers. The amplitude of the subgap peaks is noticeably larger at negative gate voltage then at positive for the single layer sample, while it is fairly unchanged in the multilayer sample. In the single layer sample, the distance between the subgap peaks closes at about V_g = -7V at which point the amplitude of the peaks adds. The peaks diverge again only to reclose at about V_g = -13V. A similar envelope is present from about V_g = 10 – 16 V

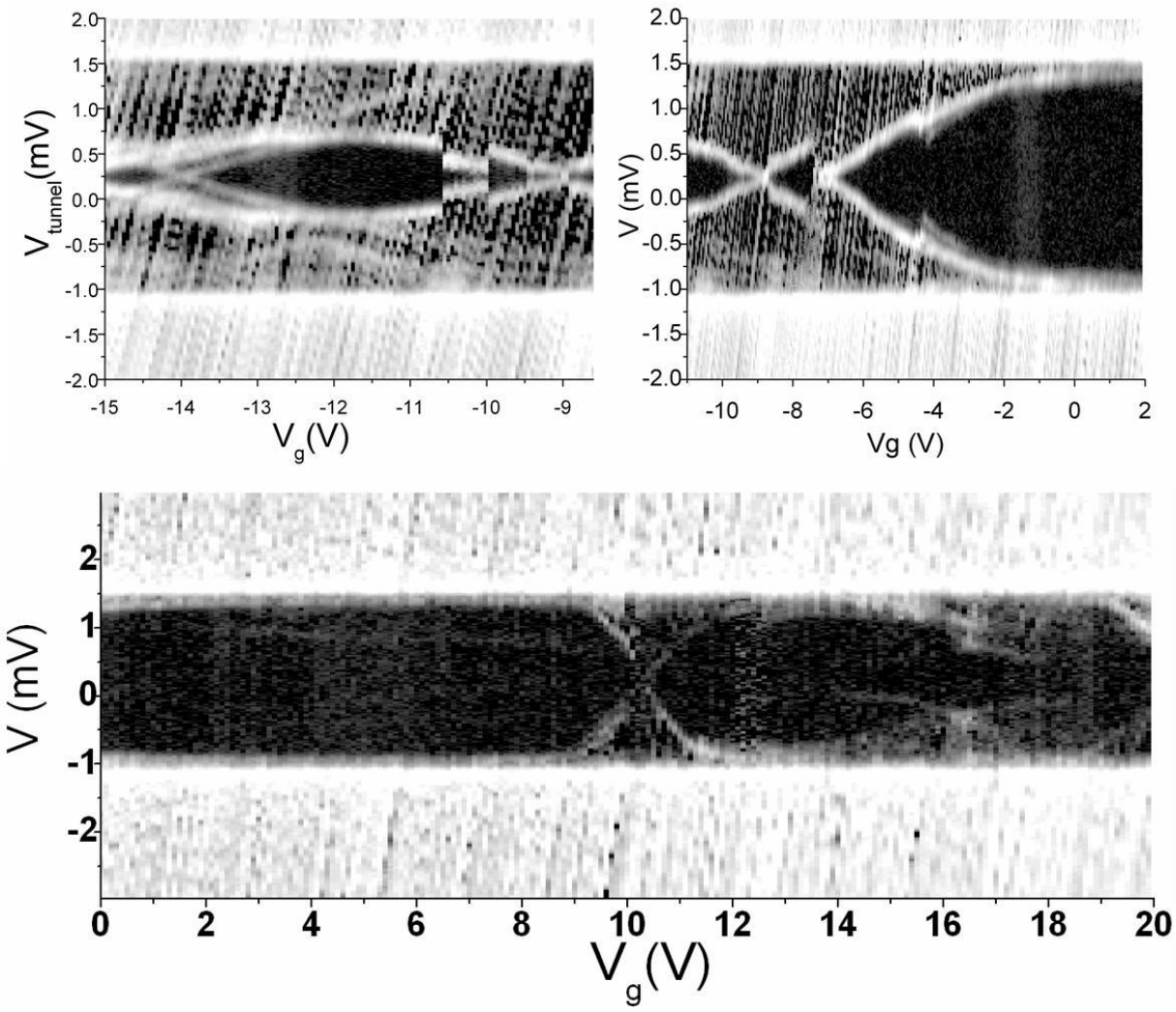

Figure 6-7: 2D plots of Tunnel probe conductance on a log scale versus bias voltage and backgate voltage for the single-layer device at three different gate ranges. Subgap peak separation is symmetric about zero bias and gate dependent.[*]

[*] Note that in all the data there is an unphysical offset of about 0.25 mV in the Bias voltage due to a powered sumbox. Also the top two graphs contain repeated features. This is likely due to sudden movement of charge in the gate, so that the effective potential repeats itself at a higher applied gate voltage and is probably not a real feature of the device.

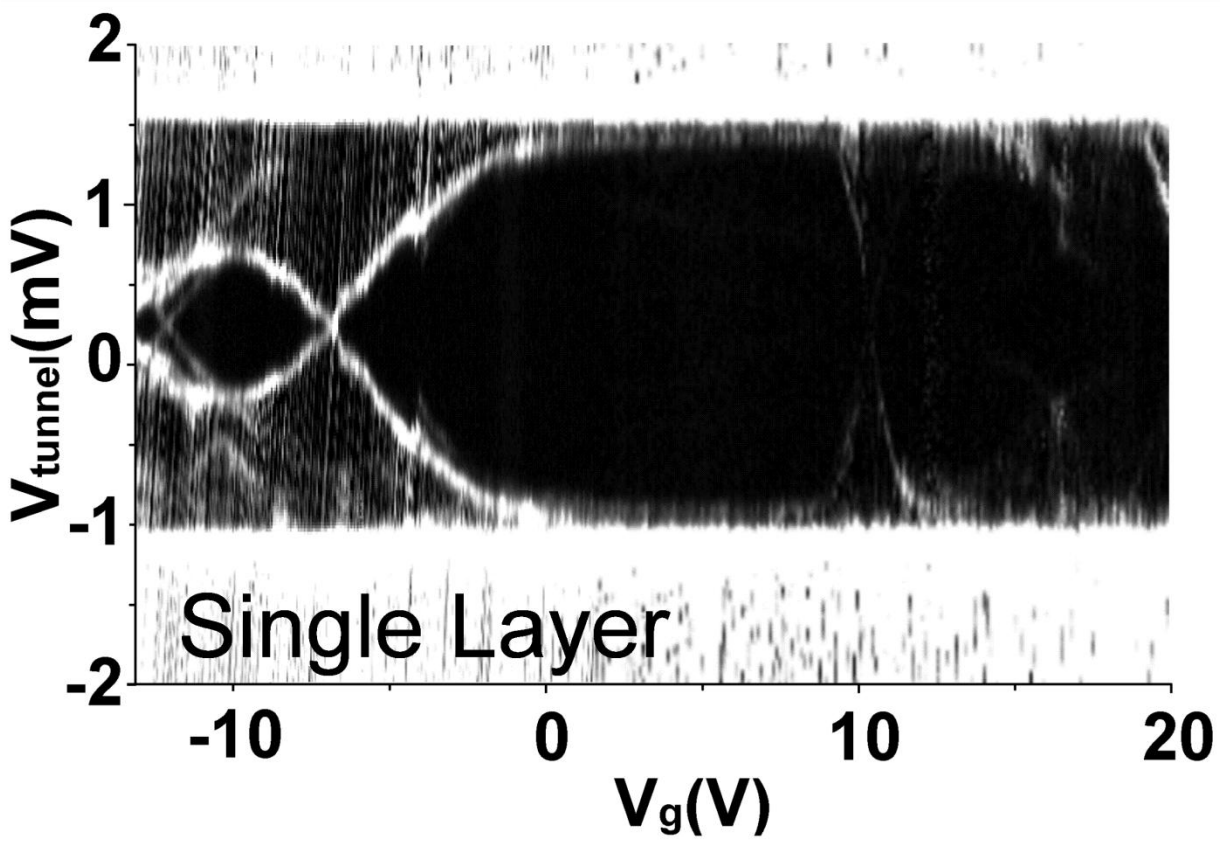

Figure 6-8: Same as Figure 6-7, only the three gate ranges have been put together, and the gate slips manifest as repeated features in the top two graphs of Figure 6-7 have been removed to reveal the evolution of the subgap peaks.

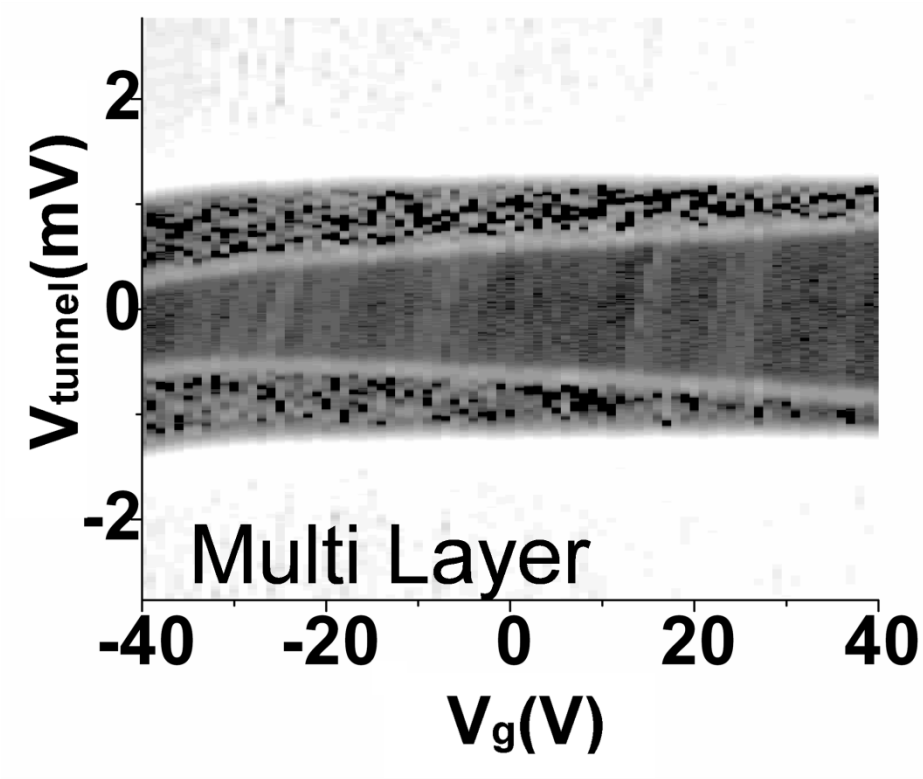

Figure 6-9: Same as Figure 6-8 but for the multi-layer sample in which screening from graphene layers reduces the gating effect. (Note that in all the data there is an unphysical offset of about 0.25 mV in the Bias voltage due to a powered sumbox.)

Figure 6-10 and Figure 6-11 show the temperature dependence of the subgap peaks. The peaks decrease in amplitude and increase in breadth as temperature is increased. As shown in Figure 6-11, the peak heights decrease as the temperature rises, but only until about 0.8K when they stop evolving with temperature and remain fixed as the SC gap closes. The peaks' evolution with magnetic field is quite different. As can be seen in Figure 6-12 and Figure 6-13 the amplitude of the peaks is not suppressed and in the case of the negative bias peak, appears to be enhanced by magnetic field.

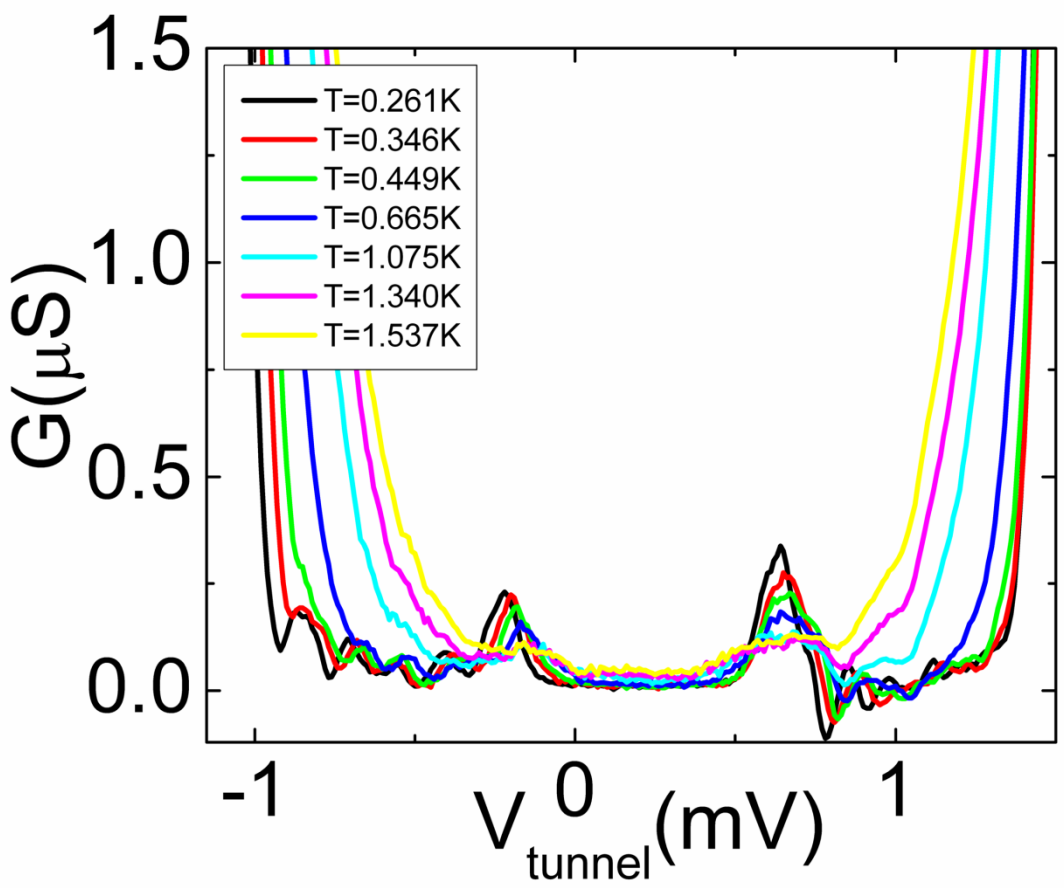

Figure 6-10: Close up of Subgap conduction peaks showing behavior as temperature is varied.

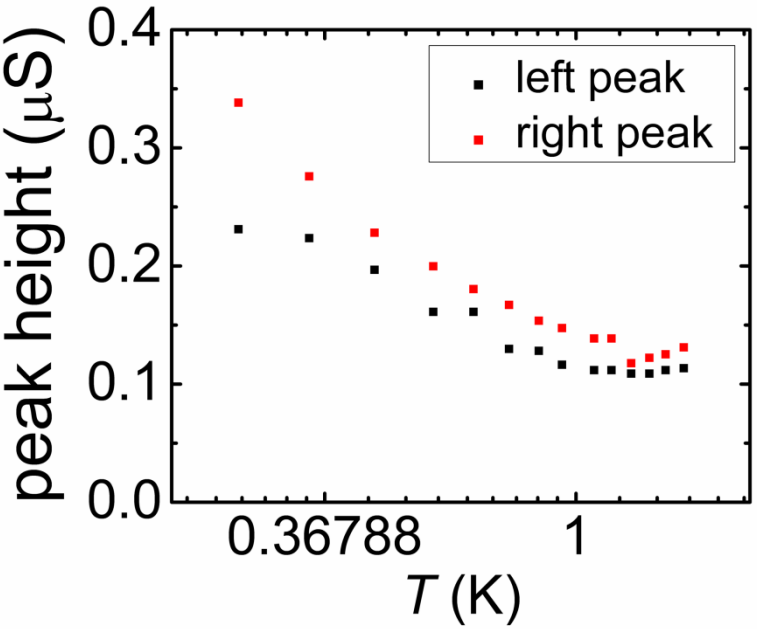

Figure 6-11: Peak height vs. temperature on a semi-ln plot is inconsistent with the Kondo effect.

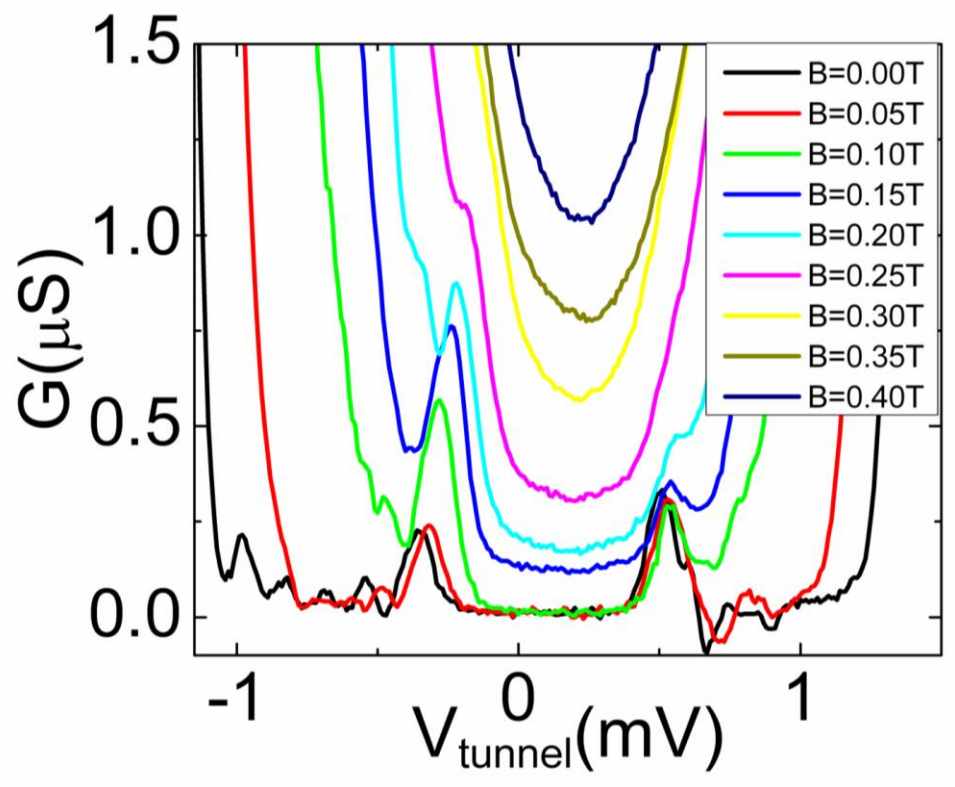

Figure 6-12: Close-up of Subgap conduction peaks showing behavior as magnetic field is varied. The peaks are robust under increased magnetic field.

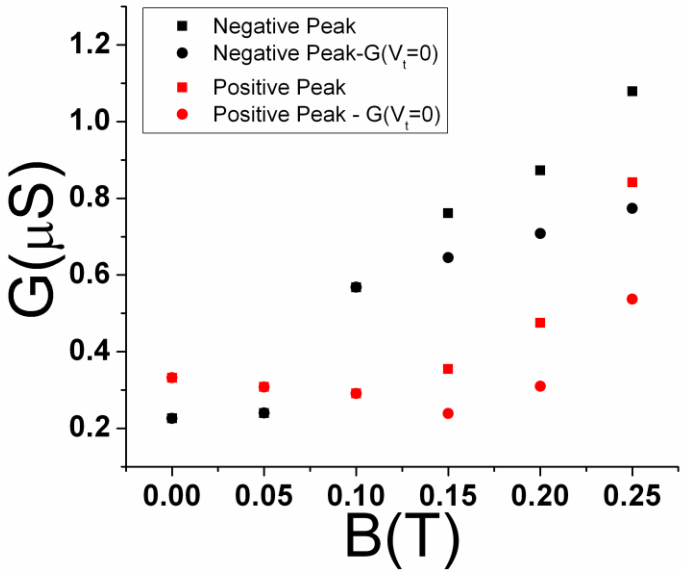

Figure 6-13: Peak height Vs magnetic field. Negative bias peak in black. Positive bias peak in red. Circle data points have the conductance at V_t=0 subtracted from the height.

6.4 What the gap features are not

The subgap features are particularly puzzling since they are energetically forbidden. Before delving into the possible cause of the subgap peaks, it is instructive to rule out a few things. First, one might imagine that the In capping layer may have migrated through or around the probe to make contact with the graphene and we are simply seeing a second superconducting gap. This would explain why the conductance actually goes to zero between the subgap peaks, but not before. This cannot be the case however, since a second superconducting gap would not be gate-dependent. Also, the subgap peaks are likely not a multiple Andreev reflection effect because they depend on gate voltage, show no zero bias conductance, and have little B-field dependence. Another possibility is that the tunnel barrier is leaky. In this case however, we would expect the peaks to be asymmetric with respect to zero bias; they are not.[108] A fourth intriguing idea is that the subgap peaks are a beating pattern between frequencies of the bias oscillations which extend into the gap. This is probably not true since the oscillations are killed quickly by the application of a magnetic field, but the subgap peaks persist. Finally, the subgap peaks are inconsistent with a Kondo effect because the peaks don't split in a magnetic field. Also Figure 6-11 displays the subgap peak height versus temperature on a semi-ln plot. Since $G \propto \ln(T)$ for the Kondo effect, we would expect a straight line on this is plot.

6.5 Bound Andreev States

A final hypothesis for the origin of the subgap peaks involves the possibility of bound Andreev states confined in a quantum dot formed under the tunnel probe in the graphene.* Andreev bounds states are closed trajectories composed of Andreev reflections and regular reflections and have been predicted to exist at Superconductor-Graphene interfaces.[109-111] In

* I'd like to thank Paul Goldbart, Siddhartha Lal and Bruno Uchoa for spending long hours with us bent over this data with the strong sense that it is just too pretty not to be interesting. The result of those hours is a final hypothesis involving the possibility of bound Andreev states at the tunnel probe / graphene interface. I'd also like to thank Taylor Hughes for joining our effort and providing invaluable simulation expertise, and producing the simulation plots shown below.

Figure 6-14 the arrows illustrate one such path in a superconductor / n-type normal metal / p-type normal metal junction. Starting at the top, an electron (a solid black arrow), enters from the normal metal and is Andreev reflected off the superconductor, sending a hole (dotted arrow) back to the p-type metal, where it is reflected off the p-n junction back at the superconductor. The hole Andreev reflects off the superconductor, sending an electron back towards the p-n junction, where it is reflected to close the loop. It is resonant tunneling through the energy levels of these bound states that is proposed to form the subgap peak.

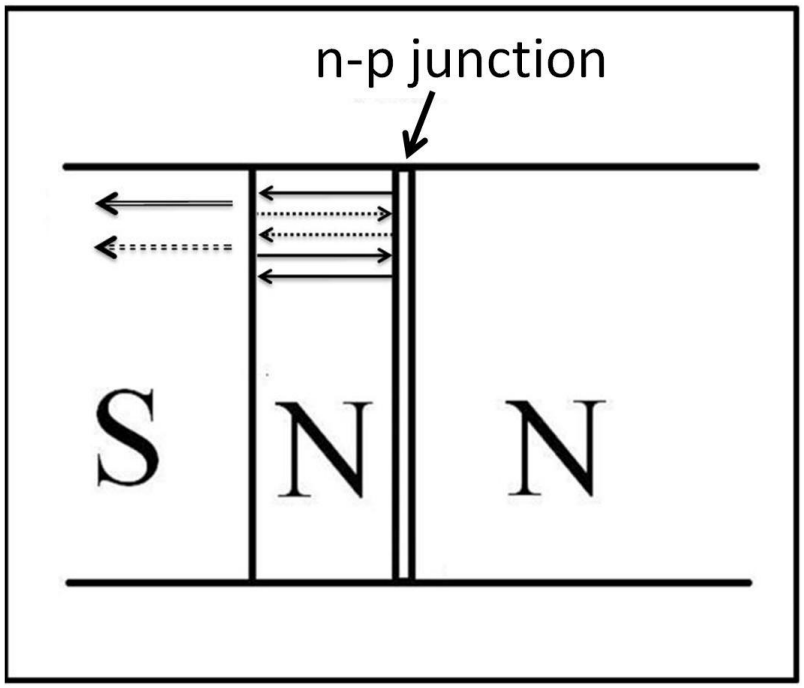

Figure 6-14: A model system, in which a QD between the superconducting tunnel probe and a p-n junction supports Andreev Bound states. Arrows describe an example of a quasiparticles path that forms an Andreev bound states. Starting at the top, and electron, solid black arrow, enters form the normal metal and is Andreev reflected off the superconductor, sending a hole, dotted arrow back to the p-n junction, where it is reflected off the p-n junction back at the superconductor. The hole Andreev reflects off the superconductors, sending an electron back towards the p-n junction, where it is reflected to close the loop.

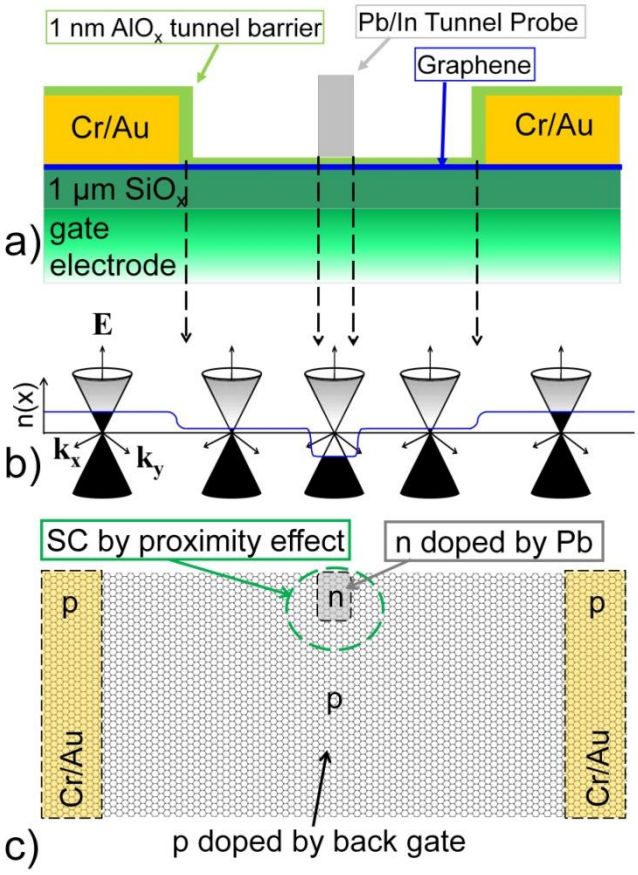

Figure 6-15: a) Side cut schematic of our device. b) Doping profile as a function of position in the device, with Dirac cones showing position of Fermi level. Graphene under Cr/Au contacts is strongly p doped. Bulk graphene is p doped by the backgate. The region under the tunnel probe is n doped by the Pb. c) Top view of graphene lattice showing doping due to contacts and area of pnp quantum dot. Dotted green circle indicated area of graphene which is populated with cooper pairs due to proximity effect.

As can be seen in Figure 6-3, single-layer graphene shows an asymmetric Dirac point at $V_g \sim$ 17.5 V. The multi-layer sample does not show a Dirac point within the measured gate voltage range; this is not unexpected, as the gate dependence is typically weak in multi-layer samples. In all cases the Dirac point was offset to the positive gate side greater than 20 volts and, when the Dirac point is reached, the cone is asymmetric. Both effects have been predicted[112] and observed,[106] and are due to work a function mismatch at the metal graphene interface, that leads to doping of the graphene below the contacts. When materials with differing work functions are brought together, charge is transferred at the interface to equalize the surface potentials. The sign of the charge transfer is the same as the sign of $\Delta W = W_m - W_g - W_c$, where W_m is the work

functions of the metal and W_g = 4.5 eV is the work function of the graphene.[112] W_c is an effective potential that arises from metal-graphene chemical interactions and is estimated at somewhere between 0 and 0.9 eV,[112] depending on the separation between the metal and graphene layer. With only a 3 Å Cr (W_{Cr} = 4.5 eV) sticking layer, the interface is dominated by the work function of the Au (W_{Au} = 5.54 eV). So for the end leads ΔW(=0.14 to 1.04 eV) is positive, indicating hole doping (p type) under the end leads similar to that seen in Ref [106].

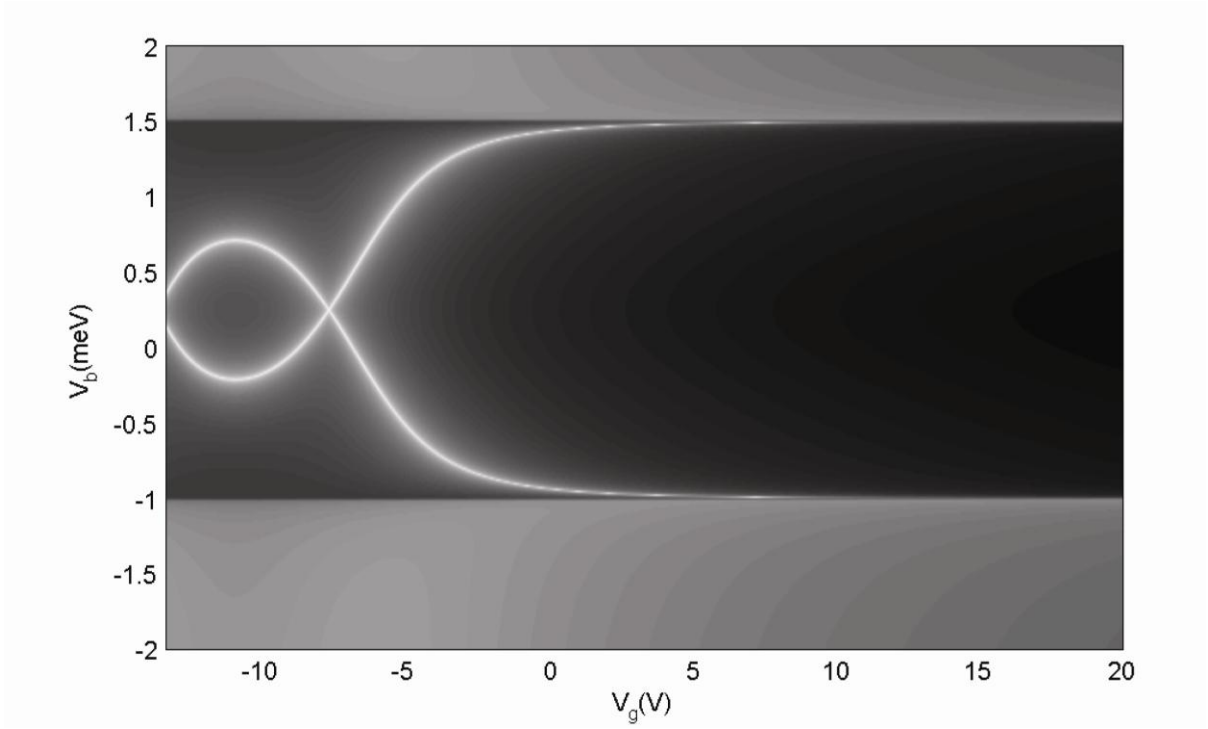

Figure 6-16: Simulation of the Dot in graphene model, fit to our data. Charging energy extracted from the fit is 1.4 meV, which is consistent with the size of the SC/graphene interface.

We believe that the graphene underneath the SC tunnel probes is also doped due to work function mismatch. However in this case, for Pb (W_{Pb} = 4.25), ΔW (=-1.15 to -0.25 eV) is negative, meaning electron doping (n type). As you can see in part (b) of Figure 6-15 this doping causes a potential well underneath of the SC tunnel probe. That potential well is formed by the pn junction that surrounds the n type well under the tunnel probe and is a quantum dot. Quantum dots formed by pn junctions have been observed before in graphene in which the central region was defined by a local top gate.[102] Quantum dots analogous to our system, due to pn junctions

caused by doping of metal contacts have also been observed in carbon nanotubes.[113] Part (c) of Figure 6-15 shows a representation of the graphene lattice from above, with doped areas from the end contacts and the tunnel probe indicated. Although our understanding of the physical situation is still evolving, it is likely that the subgap features are due to Andreev bound states that are formed by electrons and holes residing on the non-degenerate (Coulomb split) energy levels of the quantum dot. The gate voltage dependence of the bound states is due to an interplay between the Coulomb charging energy of the dot and the Andreev binding energy. In fact, it is likely that the gate dependence gives spectroscopic information about the energy of the Andreev bound state. Figure 6-16 shows a simulation of our system in a metal that considers spin-split energy levels and reflections off a superconducting lead. The correspondence with our data is remarkable and the charging energy of 1.4 meV extracted from the simulation corresponds to a dot roughly the size of our tunnel probe/graphene interface, as one would expect.

6.6 Conclusion

In conclusion, we have reported results on superconducting tunneling spectroscopy of a graphene sheet. Just outside the superconducting gap region we observe conductance oscillations as a function of bias and gate voltage, possibly due to electron phase interference between the end contact and probe interfaces. Those oscillations are strongly suppressed by a magnetic field. Unexpectedly, we also observe structure inside the superconducting gap, particularly two distinct and symmetric peaks whose positions evolve with gate voltage, and which are not suppressed by a magnetic field. The characteristics of this subgap conductance are very different from that observed in the CNT quantum dot. First the subgap conductance is observed with no applied end-to-end bias. In addition, whereas in the CNT there are several flat conduction channels crossing the gap, in the graphene there are two peaks symmetric about the bias voltage, that move together and apart with gate voltage, but stay inside the SC gap. These subgap peaks are believed to be due to resonant tunneling through Andreev bound states within a pnp quantum dot in the graphene. It is hoped that theoretical and simulation work underway will confirm this theory or provide guidance on experiments that could.

Dr. Siddhartha Lal and Dr. Bruno Uchoa are working to propose a model for the energy dependence of the bound state. Currently Dr. Taylor Hughes is working on simulating our data.

It is hoped that this model will reproduce the features we see both inside and outside the SC gap, including the lack of conduction between the subgap peaks.

Chapter 7
Conclusion

In this dissertation we investigated the electron transport properties of CNTs and graphene, one and two dimensional systems respectively. We applied a wide variety of tunneling spectroscopy techniques to study electron interactions and weak tunneling processes. Notably, the fabrication of non-invasive top tunnel probes on CNTs and graphene required serious in house development.

We began our investigation with two-probe, normal metal tunneling spectroscopy of CNTs of varying length. We measured the power law exponent, alpha, of the CNT DOS as a function of CNT length over two orders of magnitude. Alpha increases with length in a way that is qualitatively consistent with a naïve Luttinger prediction. Also, devices exhibit a defect density on the order of a micron, as indicated by temperature sweeps, variation of alpha with gate voltage, and direct observation with scanning gate microscopy. Thus, zero dimensional effects are observed on a scale that is determined more by the defect density, than by the length of the CNT. Finally, we found that the area over which conductance is proportional to a power law, in both voltage and temperature, can be significantly less than a decade due to competing effects at low temperature. Future studies will benefit from better control over the defect density. Current routes to decreasing the defect density include suspending the CNT, or using an oxide layer with fewer charge traps, such as Al_2O_3. Another possibility is to fabricate local gates over defects found with scanning gate microscopy. These defects are gate tunable, and with a local

independently addressable gate one could gate the defects away. This would allow not only that study of conductance in a very long Luttinger liquid, but also how conductance changes, as the defects are controllably varied in strength and number.

We then discussed how we created the first CNT devices with a non-invasive fabricated third probe, allowing non-equilibrium superconducting tunneling spectroscopy. Here, the CNT was contacted with two normal metal end contacts, and a third weakly-coupled superconducting tunnel probe was fabricated in the middle of the CNT. The sharp peak in the superconducting DOS, allowed measurement of the non-equilibrium electron energy distribution function, f (E). At low temperature CNTs display a two step Fermi function, with little smearing, implying that inelastic scattering processes can be relatively weak in nanotubes. There was no evidence of smearing at temperatures well below 1.5 K, even in data taken at eight different gate voltage values where the tube conductance varied by a factor of 20. Our results may be consistent with theoretical predictions of no energy relaxation in out-of-equilibrium Luttinger liquid systems [70-72] unless the system is disordered [55]. The crossover from one to zero dimensions may also limit inelastic scattering. In the near future we hope to fabricate multiple tunnel probes on a single device, to measure the dependence of f (E) on position. This will test predictions that scattering in the CNT happens primarily at the end contacts as well as to distinguish between ballistic and diffusive transport. We are also in the later stages of developing a CNT based non-equilibrium tunnel probe that should have the advantage over superconductors of being even less invasive, with a contact area of just 1 nm, and functioning at very high temperatures, up to 50 K. This will allow the study of CNTs' f (E) while firmly in the Luttinger regime.

We then took advantage of the superconductor's large DOS at the gap edge to study very weak tunneling processes. Devices were fabricated similarly to the non-equilibrium devices studied above, except the tunnel probe was much better connected to the CNT, with resistance only a few times larger the end-to-end. The clean fourfold degeneracy of a defect-free CNT quantum dot observed in the conductance gate sweep of this sample gave strong evidence that our method of depositing top tunnel probes is noninvasive. We were able to fully characterize the energy spectrum of the quantum dot. Also, as hoped, the use of a superconducting probe enhanced weak tunneling signals revealing clear evidence of both elastic and inelastic co-tunneling. These results open the door to a better understanding of the mechanisms behind weak, second-order processes in systems like CNT quantum dots, and allow for a better assessment of

such systems' use in practical devices, like single electron transistors, quantum current standards, and quantum qubits. All of these schemes take advantage of the systems' unusual first order tunneling properties, namely the Coulomb blockade, with second order co-tunneling processes constituting error. Finally, when bias was applied end-to-end we observed unexpected, energetically forbidden conductance signals inside the superconducting gap. The origin of these conduction channels is not understood, but could be related to inelastic scattering in the CNT dot. In the future, we hope to measure the dependence of this conduction on the applied end-to-end bias in similar devices.

Finally we applied the same superconducting tunneling spectroscopy techniques to graphene sheets. There are conductance oscillations as a function of bias and gate voltage just outside the superconducting gap region, possibly due to electron phase interference between the end contact and probe interfaces. Unexpectedly, we also observe structure inside the superconducting gap, particularly two distinct and symmetric peaks whose positions evolve with gate voltage, and which are not suppressed by a magnetic field. The two are peaks symmetric about bias voltage, and move together and apart with gate voltage, but stay inside the SC gap. We hypothesize that the peaks are due to conduction through Andreev bound states confined to a quantum dot in the graphene.

In conclusion, the potential for superconducting tunneling spectroscopy and non-equilibrium tunneling spectroscopy in low dimensional materials is only beginning to be tapped. Extensions of this work will provide spatial resolution of electronic density of states and energy relaxation in CNTs which will likely be broadly applicable to other 1-D systems. Open questions remain about the source of the anomalous subgap conductance observed in both CNT and graphene systems, but the enticing answers probably lie in the interplay between the unique correlated electron states of carbon nanostructures and superconductors. We hope that these results will motive further theoretical and experimental work. Finally, the development of other tunnel probes with unique properties holds great promise. In particular, we hope that the CNT tunnel probe proves viable at relatively high temperatures. This would allow non-equilibrium tunneling spectroscopy studies in an entirely different temperature regime. If viable, it is also likely that a

CNT based STM tip could be developed for similar measurements with atomic resolution on short length scales.*

* CNT STM tips exist, but this technique would require development of a very short CNT tip so as to be in the coulomb blockade regime, at the temperature of interest.

Appendix: Fabrication details

The stencil[*]

For nanolithography creating the stencil is a three step process. The mask itself is composed of a polymer solution of polymethyl methacrylate (PMMA) and anisole. The solution is dropped on to the silicon wafer which is then spun at high RPM to distribute the polymer in a thin uniform layer. Finally the solvent is baked out. I use three different PMMA dilutions and spin on recipes for the three different thickness ranges required by the devices. In general lower molecular weight resists will spin on thinner and allow for smaller features. However thicker resist layers will allow for liftoff of taller features. Generally resist layer should be about twice as thick and the layer evaporated on top for easy lift off. See the recipes below.

Table 1: PMMA spin recipes

Step	Thickness ~50-75nm (Fe catalyst pads)	Thickness ~100-150nm (For Contact pads and Alignment marks)	Thickness ~2000nm (For Superconducting Tunnel Probes)
1	Bake chip on hot plat at 180 C for 60 seconds	Bake chip on hot plat at 180 C for 60 seconds	Bake chip on hot plat at 180 C for 60 seconds
2	Drop 950 PMMA A2 onto wafer and spin at 4500 RPM for 45 seconds	Drop 950 PMMA A4 onto wafer and spin at 4500 RPM for 45 seconds	Drop MMA(8.5)MAA onto wafer and spin at 4000 RPM for 45 seconds
3	Bake on hot plate for 60 seconds	Bake on a hot plate for 60 seconds	Bake at 180 for 2mins
4			Drop 950 PMMA A2 onto wafer and spin at 6000 RPM for 45 seconds
5			Bake at 180 for 2 mins

Now that the chip is safely masked we need to remove the parts of the mask where were want to paint. When an electron beam is passed over the PMMA it breaks chemical bonds between the polymer chains. Then this exposed PMMA can be dissolved away, leaving the rest of the mask. A Raith e-line electron beam lithography machines is used for this task. An AutoCad design is loaded onto the Raith with shapes to be exposed and associated dosages to be delivered. The

[*] As I mentioned in chapter 2 Nano-fabrication is a lot like painting a sign with stencils.

Raith has a piezo electric controlled and laser interferometer tracked stage that allow for precise positioning with respect to the alignment marks on the wafer. The Raith is aligned to the marks on the wafer and the pattern is written. The resulting features are limited in size by the width of the electron beam, which is ~3 nm on the e-line and the average length of the polymer chains in the PMMA. Finally the pattern is developed in a 1:3 mixture of Methyl isobutyl ketone (MIBK) and Isopropyl alcohol (IPA) for 60 seconds, then rinsed in IPA and dried in Nitrogen. This process dissolves the exposed PMMA and our mask is complete.

The Paint

In our case the "paint" is various metals. These metals are evaporated onto the sample via two different methods Electron Beam evaporation and Thermal evaporation, described below.

Electron Beam Evaporation: the concept

In electron beam evaporation metal in a crucible, called the source, is heated with a collimated, directed electron beam until it is hot enough to emit gaseous metal. A sample is placed above the source to receive the evaporated metal and the entire process occurs in high vacuum, typically 10^{-5} torr or less. Because the metal tends to stick to whatever it hits first and cool, instead or rebounding, ebeam evaporation is semi-directional with the source functioning, loosely, as a point sources. This is important because it leads to easier liftoff, and allows one to take advantage of shadowing effects in fabrication. The rate of metal evaporation is measured by a crystal monitor, the heart of which is a quartz crystal microbalance. Advantage is taken of the piezo electric effect to measure the resonant frequency of oscillation in a quartz crystal driven with an applied AC current. As mass is added to the crystal in the form of deposited metal, the resonant frequency of the crystal changes. Our system contains two shutters: one pneumatic, which blocks the source from the sample mounting space above and one fixed, which can be used to block a sample from the source below. Finally the sample mounting carriage can be rotated during evaporation to insure uniform thicknesses of multiple samples.

The critical parameters in ebeam evaporation are the pressure in the chamber, the intensity of the electron beam, and the area and frequency of the beam sweep over the source. Generally lower pressures are better. Lower chamber pressures result in less heat transfer to the sample. Also cooling during flight from the source to the sample is minimized, with generally results in

more continuous, less grainy films. Pressure was generally $2x10^{-6}$ torr or lower before evaporation. Note that pressure will rise somewhat during evaporation as things warm and outgas. The power of the electron beam controls the rate of evaporation by indirect influence of the temperature of the source metal. Evaporation rates are also influence by the area and frequency of beam sweep. Beam sweep control affects the rate of evaporation by changing the amount of the source that is hot enough to emit. Ideally the beam is swept quickly over the entire area of the source such that it is one uniform temperature. Usual rates of evaporation are between 1 and 5 angstrom per second. CNTs and Graphene are sensitive to defects caused by heat during evaporation. For this reason rates are kept around 1 Å/s to give heat time to dissipate without taking and unacceptable length of time to evaporate.

Electron beam Evaporation: General procedure

First the chamber is vented and he sample placed facedown over the source. The source-shutter is closed, blocking the source from the sample stage area above. The sample is placed behind a fixed shutter which blocks it from the source below. Clean away any loose metal flake to prevent them from contaminating the source. The chamber is then pumped down to $2x10^{-6}$ torr or less. The electron beam is turned on and the power ramped up until the beam is visible as a hot spot on the source metal over about a minute. Establish a sweep pattern that maximized the source area covered without and visible beam spot touching the side of the crucible. Increase the sweep speed to insure and uniform distribution of heat. Ramp up the power until a rate of evaporation in observed over the course of a minute. It is crucial to watch the source during this process to be sure it does not look too hot. This can be judged from the color of the source during previous normal evaporations. In this way one can avoid overheating and splattering the source when the crystal monitor is not working. It will take a few minutes for the source to warm to a stable temperature. During this time the power required for a given rate of evaporation will drop, so continue to adjust the power until the rate of evaporating is stable at the desired rate for at least 2 minutes. If one observes bright floating bits in the heated metal (particularly with Fe), this is generally an oxide of that metal. It will be observed that the floating oxide is attracted to the hot spot created by the electron beam and that they will eventually evaporate away. Also Oxide can detach itself from the cooler edges of the source and float to the center during an evaporation. To avoid this enlarge the sweep area to free the oxide around the edges of the

source. Once this oxide is free, decrease the sweep size again and wait for the oxide to evaporate. Now you have created an oxide free buffer that should protect your sample from mid-evaporation contamination. Once the Oxide is gone and the rate has been stable for 2 mins open the source shutter and check that the rate does not change, indicated in that the crystal monitor is not shadowed by the shutter. Close the source shutter then turn on the sample rotation. Then open the source shutter to begin deposition. When desired thickness is reached close the source shutter and power off the electron beam. If the evaporator has a load lock, remove samples. If not, wait at least 20 mins for sources to cool to minimized oxidation.

Typically contact materials consist of a sticking layer of Palladium, Titanium, or Chromium between 5 and 30 nm and a 30 nm layer of Gold. Palladium makes nearly ohmic contacts, while Titanium and Chromium typically result in higher resistance tunneling barriers.

Table 2: Electron beam evaporation parameters

Layers	Alignment Marks	Catalyst Pads	Contact Pads Pd/Au	Contact Pads Cr/Au
1	Rate = 0.3 nm/s Total = 60 nm Cr	Rate = 0.02 nm/s Total 0.1 nm Fe	Rate = 0.1 nm/s Total = 5 nm Pd	Rate = 0.05 nm/s Total = 0.3 nm Cr
2			Rate = 0.1 nm/s Total = 30 nm Au	Rate = 0.1 nm/s Total = 30 nm Au

Thermal Evaporation

The process of thermal evaporation is very similar to electron beam evaporation only the method of heating the source is different. Here the metal to be deposited is heated by running current through a “boat” which is a piece of metal with a higher melting point then the source. The metal is thus Joule heated until it evaporates. This process is directional for the same reason as Electron beam evaporation. Also, the geometry of the evaporator is similar to the ebeam evaporator described above with the source on bottom, the sample mounted above and a crystal monitor to keep track of the evaporation rate. The critical parameters in thermal evaporation are the pressure in the sample chamber, for the same reasons mentioned above, and the current through the boat, which determines the temperature of the source-metal and thus the rate of evaporation.

Table 3: Thermal Evaporation Parameters

Step	Pb/In Superconducting Tunnel probe
1	Pre-evaporate Pb Pressure = 2.0 x 10^{-6} torr Current = 49 A Rate = 0.1 nm/s Total = 30 nm
2	Open sample to source and evaporate 200 nm
3	Pre-evaporate In Pressure = 3.3 x 10^{-6} torr Current = 65 A Rate = 0.13 nm/s Total = 25 nm
4	Open sample to source and evaporate 30 nm

Removing the stencil.

This is the easiest part… or it should be. Simply place the chip in a beaker of ACE and stand back for a half hour. The ACE will dissolve the PMMA and the unwanted layer of metal will float away like a leaf on the wind. This is called Lift off and with Chromium it really is that simple. After about 2 seconds in the ACE a wave roles over the mirror Cr surface, crumpling it like a giant earthquake rippling through the earth's surface. Fifteen minutes later the Cr can be peacefully rinsed away. With two angstroms of iron, things are similarly copacetic. Everything else can be a horrible pain.

People say liftoff is an art form. This is what people say when they can do something but they can't tell you how. Liftoff problems can occur for several reasons. The most common newbie error is to attempt to rinse off the metal layer too early. It takes time for the ACE to work its way under the metal layers from the edges of the chip. On the other hand waiting too long can allow the metal layers to fall onto the Si wafer and stick in places. For the Resist recipes mentioned above with a 0.5x0.5cm chip ~35 mins seems to be about right. The metal will come off with a gentle spray of the ACE bottle, except when it doesn't. There are a many techniques to tackle stubborn liftoffs. For example one can sonicate the sample in ACE for a few seconds or sometimes for a few hours. This method and many others are generally useless for these devices. The Pd and Pb in the contacts and tunnel probe do not stick well to the surface and will come off in pieces under this rough treatment. Other common methods involve stronger solvents, heated

solvents, and samples suspended upside down in heated, stronger solvents kept swirling on a stir plate. Generally for the feature sizes used in the devices studied here in, with fresh resist and a well functioning evaporator none the harsh methods are required. The metal should lift off with a few squirts from an ACE rinse bottle. If not, a simple mechanical method that does the trick is to use a syringe to spray the sample harder with ACE. Be very careful not to scratch the pattern with the needle. Generally one can spray 2-3 syringe full's before the pattern starts to come off. Check the pattern under a microscope often when using this method, as it can destroy the smaller parts of the pattern. If the sample has lifted off satisfactorily, rinse it in IPA and blow dry with Nitrogen. If the sample has not lifted off satisfactorily by now the best strategy is to remake the device. Generally something has gone wrong along the way, expired resist, or drastically more metal then you expected to have.

CNT Growth Recipes:[*]

"Standard" recipe:[†] yields ~10 um long CNTs

1) Heat sample to 900 C over ½ hour in 1000 sccm Argon and 300 sccm hydrogen.
2) Turn off Ar, and turn on 5000 sccm Methane. Continue growth in 5000/300 sccm methane/Hydrogen for 15 mins.
3) Cool in 1000 sccm argon

Fast heating recipe:[‡35] yields ~50-500 um long CNTs

1) Place sample about 6-12 inches upstream of the tube furnace.
2) Heat oven to 900 C over ½ hour in 1000 sccm Argon and 1100 sccm hydrogen.
3) Turn off Ar, and turn on 1100 sccm Methane.
4) Role furnace over the sample to begin growth. Continue growth in 1100/1100 sccm methane/Hydrogen for 30 mins.
5) Cool in 1000 sccm Argon

[*] Recipes are for 0.1 nm Fe catalyst and assume a 1" tube furnace CVD with Methane, Hydrogen and Argon unless otherwise noted. Also, always purge system with argon after loading sample and before removal to keep Hydrogen away from oxygen in the air.

[†] This recipe is optimized for a 3" tube furnace. For 1" furnace flows should be scaled down.

[‡] This recipe is based on that from ref 34, but optimized for a 3" tube furnace and must be scaled down for use in a 1" furnace.

Low Flow recipe:[*36] yields ~50-500 um long CNTs more consistently, in 1/3 the growth time, with 1/10th the gas flow. Longer CNTs are possible with longer growth time.

1) Heat oven to 950 C over ½ hour in 100 sccm Argon and 60 sccm hydrogen.
2) Turn off Ar, and turn on 100 sccm Methane. Here the idea is to keep a smooth flow, so do this at the same time. Continue growth in 100/60 sccm methane/Hydrogen for 12 mins.
3) Cool in 200 sccm Argon

Pre-growth annealing recipe: For use when humidity causes CNT yield to fall.

1) Heat oven to 250 C 200 sccm Argon overnight.
2) Next day, increase temperature to 700 C in 100 sccm Argon and 60 sccm hydrogen. Anneal for 10 mins at 700 C.
3) Heat to growth temperature and continue with step 2 of the Low Flow recipe.

Tweezermanship

Scratched and dropped sample can be a major source of lost devices. For this reason Tweezermanship is an essential skill for this type of work. Like other types of work with tools half the battle is using the correct tools for the job. I carry X types of tweezers with me at all times when fabricating, but for handling sample I use only two 99% of the time. There are basically two ways to hold a chip: By the edges, or by the top and bottom. Holding by the top and bottom is much more stable, but is usually ruled out by our necessarily small sample size. Since most of the space is required for devices, edge grabbing is generally required. This is dangerous because chips want to rotate and "squirt" out of the tweezers. The following tweezers are optimized for edge grabbing.

[*] This recipe yields clean single walled CNTs, so I use it even when long devices are not required. It is based on ref 35 in which it is suggested that laminar flow through a small enclosed boat, leads to the long CNT growth. We find, that laminar flow is not necessary and that an open boat in a 1" furnace with the low gas flows they describe efficiently yield ultra long CNT growth.

The work horse: [Techni-tool Swiss made SM111] The cupped tweezers. When combined with gel pack for sample storage these tweezers will make anyone look like an expert and allow one to do things that would be very dangerous with other types of tweezers because they allow for and extremely secure hold. There are two drawbacks to be aware of. First the cups must be able to slide under you sample, so hard flat surfaces can be a problem. This problem can be dealt with in several ways. Look for chips with an undercut edge. This will guide your tweezers underneath even on a hard flat surface. Also, if working on a hard flat surface, like a chemical hood, place the sample on a cleanroom wipe. This will allow just enough "give" in the surface for your cupped tweezers to get under your sample for a good solid hold. Second these tweezers have a defined angle at which you must grasp your sample, so they are not useful when you must reach down into something deep, like a beaker. For this reason I use flat Petri-dish-like containers for solvent soaking and rinsing.

The backup: [Techni-tool Swiss made 2A] If you must pick up your chip from directly above, you need a different tool. The wide rounded tips allow for a large area of contact from many different angles including vertical. These tweezers are worst at very shallow angle, where the Cupped tweezers are the best. Together, these tweezers allow for safe movement to and from almost any situation.

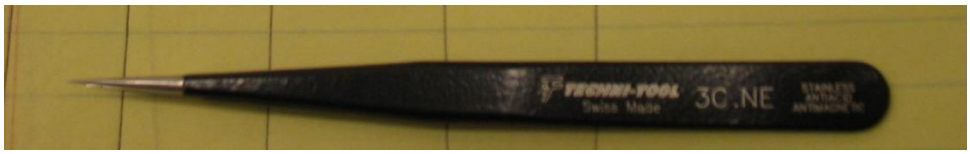

For handling small wires: [Techni-tool Swiss made 3C] Finally, for handing small cryogenic wires these ultra sharp precision tweezers are a must. They are also invaluable for threading a wedge bonding tip.

References

1 Fisher, M. P. A. & Glazman, L. I. *Transport in a one-dimensional Luttinger liquid*, <http://arxiv.org/abs/cond-mat/9610037> (2006).

2 Camino, F. E., Wei, Z. & Goldman, V. J. Realization of a Laughlin quasiparticle interferometer: Observation of fractional statistics. *Physical Review B (Condensed Matter and Materials Physics)* **72**, 075342 (2005).

3 Eun-Ah, K., Michael, L., Smitha, V. & Eduardo, F. Signatures of Fractional Statistics in Noise Experiments in Quantum Hall Fluids. *Physical Review Letters* **95**, 176402 (2005).

4 Leinaas, J. M. & Myrheim, J. On the Theory of Identical Particles. *Il Nuovo Cimento* **Vol 37**, 132.

5 Oshikawa, M. Junction of Tomonaga-Luttinger liquids. *Physica E: Low-dimensional Systems and Nanostructures* **29**, 483-489 (2005).

6 Tomonaga. *Journal of physics C. Solid state physics* **5**, 544 (1950).

7 Luttinger, J. M. An Exactly Soluble Model of a Many-Fermion System. *Journal of Mathematical Physics* **4**, 1154-1162 (1963).

8 Haldane, F. D. M. 'Luttinger liquid theory' of one-dimensional quantum fluids. I. Properties of the Luttinger model and their extension to the general 1D interacting spinless Fermi gas. *Journal of Physics C: Solid State Physics*, 2585 (1981).

9 Auslaender, O. M. *et al.* Spin-charge separation and localization in one dimension. *Science* **308**, 88-92 (2005).

10 Iddo, U. & Leonid, I. G. Signatures of Spin-Charge Separation in Scanning Probe Microscopy. *Physical Review Letters* **93**, 196403 (2004).

11 Lee, J. *et al.* Real space imaging of one-dimensional standing waves: Direct evidence for a Luttinger liquid. *Physical Review Letters* **93** (2004).

12 Lorenz, T. *et al.* Evidence for spin-charge separation in quasi-one-dimensional organic conductors. *Nature* **418**, 614-617 (2002).

13 Yacoby, A. *et al.* Tunneling spectroscopy of quantum wires: Spin-charge separation and localization. *Physica Status Solidi B-Basic Solid State Physics* **243**, 3593-3603 (2006).

14 Kim, N. Y. *et al.* Tomonaga-luttinger liquid features in ballistic single-walled carbon nanotubes: Conductance and shot noise. *Physical Review Letters* **99**, 036802 (2007).

15 Bockrath, M. *et al.* Luttinger-liquid behaviour in carbon nanotubes. *Nature* **397**, 598-601 (1999).

16 Tans, S. J. *et al.* Individual single-wall carbon nanotubes as quantum wires. *Nature* **386**, 474-477 (1997).

17 Reibold, M. *et al.* Materials: Carbon nanotubes in an ancient Damascus sabre. *Nature* **444**, 286-286 (2006).

18 Vishveshwara, S. PhD thesis.

19 Pan, S. H., Hudson, E. W. & Davis, J. C. Vacuum tunneling of superconducting quasiparticles from atomically sharp scanning tunneling microscope tips. *Applied Physics Letters* **73**, 2992-2994 (1998).

20 Rodrigo, J. G., Suderow, H., Vieira, S., Bascones, E. & Guinea, F. Superconducting nanostructures fabricated with the scanning tunnelling microscope. *Journal of Physics: Condensed Matter* **16**, R1151 (2004).

21 Saito, R., Dresselhaus, M. S. & Dresselhaus, G. *Physical Properties of Carbon Nanotubes*. (Imperial College Press, 2003).
22 Durkop, T., Getty, S. A., Cobas, E. & Fuhrer, M. S. Extraordinary mobility in semiconducting carbon nanotubes. *Nano Letters* **4**, 35-39 (2004).
23 Bethune, D. S. *et al.* Cobalt-Catalyzed Growth of Carbon Nanotubes with Single-Atomic-Layerwalls. *Nature* **363**, 605-607 (1993).
24 Iijima, S. & Ichihashi, T. Single-Shell Carbon Nanotubes of 1-Nm Diameter. *Nature* **363**, 603-605 (1993).
25 Thess, A. *et al.* Crystalline ropes of metallic carbon nanotubes. *Science* **273**, 483-487 (1996).
26 Hata, K. *et al.* Water-assisted highly efficient synthesis of impurity-free single-waited carbon nanotubes. *Science* **306**, 1362-1364 (2004).
27 Kristopher, D. M. *et al.* Growth modes of carbon nanotubes on metal substrates. *Journal of Applied Physics* **100**, 044309 (2006).
28 Bhaviripudi, S. *et al.* CVD synthesis of single-walled carbon nanotubes from gold nanoparticle catalysts. *Journal of the American Chemical Society* **129**, 1516-+ (2007).
29 Cheung, C. L., Kurtz, A., Park, H. & Lieber, C. M. Diameter-controlled synthesis of carbon nanotubes. *J. Phys. Chem. B* **106**, 2429-2433 (2002).
30 Lu, C. G. & Liu, J. Controlling the diameter of carbon nanotubes in chemical vapor deposition method by carbon feeding. *J. Phys. Chem. B* **110**, 20254-20257 (2006).
31 Chen, Y. *et al.* Low-defect, purified, narrowly (n,m)-dispersed single-walled carbon nanotubes grown from cobalt-incorporated MCM-41. *ACS Nano* **1**, 327-336 (2007).
32 Wang, B. *et al.* (n,m) selectivity of single-walled carbon nanotubes by different carbon precursors on co-mo catalysts. *Journal of the American Chemical Society* **129**, 9014-9019 (2007).
33 Zhang, G. Y. *et al.* Ultra-high-yield growth of vertical single-walled carbon nanotubes: Hidden roles of hydrogen and oxygen. *Proc. Natl. Acad. Sci. U. S. A.* **102**, 16141-16145 (2005).
34 Yao, Y., Dai, X., Liu, R., Zhang, J. & Liu, Z. Tuning the Diameter of Single-Walled Carbon Nanotubes by Temperature-Mediated Chemical Vapor Deposition. *The Journal of Physical Chemistry C* **113**, 13051-13059 (2009).
35 Huang, S., Cai, X. & Liu, J. Growth of Millimeter-Long and Horizontally Aligned Single-Walled Carbon Nanotubes on Flat Substrates. *J. Am. Chem. Soc.* **125**, 5636-5637 (2003).
36 Hong, B. H. *et al.* Quasi-Continuous Growth of Ultralong Carbon Nanotube Arrays. *J. Am. Chem. Soc.* **127**, 15336-15337 (2005).
37 Yu, Z., Li, S. D. & Burke, P. J. Synthesis of aligned arrays of millimeter long, straight single-walled carbon nanotubes. *Chemistry of Materials* **16**, 3414-3416 (2004).
38 Gawande, A. *The checklist manifesto : how to get things right*. (Metropolitan Books).
39 Sapmaz, S. *et al.* Electronic excitation spectrum of metallic carbon nanotubes. *Physical Review B* **71**, 153402 (2005).
40 Jarillo-Herrero, P., Sapmaz, S., Dekker, C., Kouwenhoven, L. P. & van der Zant, H. S. J. Electron-hole symmetry in a semiconducting carbon nanotube quantum dot. *Nature* **429**, 389-392 (2004).
41 Javey, A., Guo, J., Wang, Q., Lundstrom, M. & Dai, H. J. Ballistic carbon nanotube field-effect transistors. *Nature* **424**, 654-657 (2003).

42 Liang, W. J. *et al.* Fabry-Perot interference in a nanotube electron waveguide. *Nature* **411**, 665-669 (2001).
43 Purewal, M. S. *et al.* Scaling of resistance and electron mean free path of single-walled carbon nanotubes. *Physical Review Letters* **98** (2007).
44 Ishibashi, K., Suzuki, M., Ida, T. & Aoyagi, Y. Formation of coupled quantum dots in single-wall carbon nanotubes. *Applied Physics Letters* **79**, 1864-1866 (2001).
45 Bezryadin, A., Verschueren, A. R. M., Tans, S. J. & Dekker, C. Multiprobe Transport Experiments on Individual Single-Wall Carbon Nanotubes. *Physical Review Letters* **80**, 4036 (1998).
46 Kane, C. L. *Lectures on Bosonization*, <http://research.yale.edu/boulder/Boulder-2005/Lectures/index.html> (2005).
47 Vishveshwara, S. *A Three Act Play of Strongly Correlated Electrons* Doctorate of Philosophy thesis, University of California, Santa Barbara, (2002).
48 Bockrath, M. *et al.* Luttinger-liquid behaviour in carbon nanotubes. *Nature* **397**, 598-601 (1999).
49 Akinobu, K., Kazuhito, T., Yoshinobu, A. & Youiti, O. Gate-Voltage Dependence of Zero-Bias Anomalies in Multiwall Carbon Nanotubes. *Physical Review Letters* **92**, 036801 (2004).
50 Bellucci, S., Gonzalez, J. & Onorato, P. Crossover from the Luttinger-Liquid to Coulomb-Blockade Regime in Carbon Nanotubes. *Physical Review Letters* **95**, 186403 (2005).
51 Bockrath, M. *et al.* Resonant electron scattering by defects in single-walled carbon nanotubes. *Science* **291**, 283-285 (2001).
52 Emery, V. J. in *Highly Conducting One-Dimensional Solids* eds J. T. Devreese, R. P. Evrard, & V. E. van Doren) 247 (Plenum, 1979).
53 Wu, F. *et al.* Shot noise with interaction effects in single-walled carbon nanotubes. *Physical Review Letters* **99**, 156803 (2007).
54 Yao, Z., Postma, H. W. C., Balents, L. & Dekker, C. Carbon nanotube intramolecular junctions. *Nature* **402**, 273-276 (1999).
55 Bagrets, D. A., Gornyi, I. V. & Polyakov, D. G. Nonequilibrium kinetics of a disordered Luttinger liquid. *Physical Review B* **80** (2009).
56 Gutman, D. B., Gefen, Y. & Mirlin, A. D. Tunneling spectroscopy of Luttinger-liquid structures far from equilibrium. *Physical Review B* **80** (2009).
57 Komnik, A. & Gogolin, A. O. Multiparticle effects in nonequilibrium electron tunneling and field emission. *Physical Review B* **66**, 035407 (2002).
58 Lea, C. & Gomer, R. Evidence of Electron-Electron Scattering from Field Emission. *Physical Review Letters* **25**, 804-806 (1970).
59 Pothier, H., Gueron, S., Birge, N. O., Esteve, D. & Devoret, M. H. Energy distribution of electrons in an out-of-equilibrium metallic wire (vol 103, pg 313, 1997). *Z. Phys. B-Condens. Mat.* **104**, 178-182 (1997).
60 LeRoy, B. J., Heller, I., Pahilwani, V. K., Dekker, C. & Lemay, S. G. Simultaneous Electrical Transport and Scanning Tunneling Spectroscopy of Carbon Nanotubes. *Nano Letters* **7**, 2937-2941, doi:doi:10.1021/nl0708112 (2007).
61 Gao, B., Chen, Y. F., Fuhrer, M. S., Glattli, D. C. & Bachtold, A. Four-Point Resistance of Individual Single-Wall Carbon Nanotubes. *Physical Review Letters* **95**, 196802 (2005).

62 Gueron, S. *Quasiparticles in a diffusive conductor: Interactions and pairing* Ph.D thesis, CEA-Saclay, (1997).
63 We did not see these power laws in a sample where the tunneling probe was made normal by a magnetic field. In general, power law behaviors in single wall nanotube tunneling experiments at dilution refrigerator temperature have not yet been directly measured, as previous end-tunneling measurements were dominated by Coulomb blockade or Fabry-Perot effects.Also see See EPAPS Document No. E-PRLTAO-102-025905 for information relevant to the open quantum dot regime of the nanotube`; tunneling conductance measurements when the Pb tunneling probe is made normal in a magnetic field, to reveal the nanotube tunneling density of states`; and numerical deconvolution details. For more information on EPAPS, see http://www.aip.org/pubservs/epaps.html.
64 Nikolic, B. K. & Allen, P. B. Quantum transport in ballistic conductors: evolution from conductance quantization to resonant tunnelling. *J. Phys.-Condes. Matter* **12**, 9629-9636 (2000).
65 Giaever, I. Energy Gap in Superconductors Measured by Electron Tunneling. *Physical Review Letters* **5**, 147 (1960).
66 Pothier, H., Gueron, S., Birge, N. O., Esteve, D. & Devoret, M. H. Energy distribution function of quasiparticles in mesoscopic wires. *Physical Review Letters* **79**, 3490-3493 (1997).
67 Nagaev, K. E. On the Shot Noise in Dirty Metal Contacts. *Phys. Lett. A* **169**, 103-107 (1992).
68 Kozub, V. I. & Rudin, A. M. Shot-Noise in Mesoscopic Diffusive Conductors in the Limit of Strong Electron-Electron Scattering. *Physical Review B* **52**, 7853-7856 (1995).
69 See EPAPS Document No. E-PRLTAO-102-025905 for information relevant to the open quantum dot regime of the nanotube```; tunneling conductance measurements when the Pb tunneling probe is made normal in a magnetic field, to reveal the nanotube tunneling density of states```; and numerical deconvolution details. For more information on EPAPS, see http://www.aip.org/pubservs/epaps.html.
70 Bagrets, D. A., Gornyi, I. V. & Polyakov, D. G. Nonequilibrium kinetics of a disordered Luttinger liquid. *cond-mat*, arXiv:0809.3166v0801.
71 Khodas, M., Pustilnik, M., Kamenev, A. & Glazman, L. I. Fermi-Luttinger liquid: Spectral function of interacting one-dimensional fermions. *Physical Review B* **76**, 155402 (2007).
72 Gutman, D. B., Gefen, Y. & Mirlin, A. D. Nonequilibrium Luttinger liquid: Zero-bias anomaly and dephasing. *Physical Review Letters* **101**, 126802 (2008).
73 Bena, C. The tunneling conductance between a superconducting STM tip and an out-of-equilibrium carbon nanotube. *arXiv:0909.0867v1* (2009).
74 Kuroda, M. & Leburton, J.-P. Carrier mean free path and temperature imbalance in mesoscopic wires. . *arXiv:0903.2504v1* (2009).
75 Anfuso, F. & Eggert, S. Luttinger liquid in a finite one-dimensional wire with box-like boundary conditions. *Physical Review B* **68**, 241301 (2003).
76 Graber, M. R., Nussbaumer, T., Belzig, W. & Schonenberger, C. Quantum dot coupled to a normal and a superconducting lead. *Nanotechnology*, S479 (2004).
77 Avouris, P., Chen, Z. H. & Perebeinos, V. Carbon-based electronics. *Nat. Nanotechnol.* **2**, 605-615 (2007).

78 Leek, P. J. *et al.* Charge Pumping in Carbon Nanotubes. *Physical Review Letters* **95**, 256802 (2005).
79 Grove-Rasmussen, K. *et al.* Superconductivity-enhanced bias spectroscopy in carbon nanotube quantum dots. *Physical Review B (Condensed Matter and Materials Physics)* **79**, 134518-134515 (2009).
80 Ralph, D. C., Black, C. T. & Tinkham, M. Spectroscopic Measurements of Discrete Electronic States in Single Metal Particles. *Physical Review Letters* **74**, 3241 (1995).
81 Rodrigo, J. G. & Vieira, S. STM study of multiband superconductivity in NbSe2 using a superconducting tip. *Physica C: Superconductivity* **404**, 306-310 (2004).
82 Meservey, R. Tunnelling in a magnetic field with spin-polarized electrons. *Physica Scripta* **38**, 272 (1988).
83 Buitelaar, M. R. *et al.* Multiple Andreev Reflections in a Carbon Nanotube Quantum Dot. *Physical Review Letters* **91**, 057005 (2003).
84 Doh, Y.-J., Franceschi, S. D., Bakkers, E. P. A. M. & Kouwenhoven, L. P. Andreev Reflection versus Coulomb Blockade in Hybrid Semiconductor Nanowire Devices. *Nano Letters* **8**, 4098-4102 (2008).
85 Liang, W. J., Bockrath, M. & Park, H. Shell filling and exchange coupling in metallic single-walled carbon nanotubes. *Physical Review Letters* **88**, 126801 (2002).
86 Cao, J., Wang, Q. & Dai, H. Electron transport in very clean, as-grown suspended carbon nanotubes. *Nature Materials* **4**, 745-749 (2005).
87 Eichler, A. *et al.* Even-Odd Effect in Andreev Transport through a Carbon Nanotube Quantum Dot. *Physical Review Letters* **99**, 126602 (2007).
88 Weymann, I., BarnaÅ›, J. & Krompiewski, S. Transport through single-wall metallic carbon nanotubes in the cotunneling regime. *Physical Review B* **78**, 035422 (2008).
89 Averin, D. V. & Odintsov, A. A. Macroscopic Quantum Tunneling of the Electric Charge in Small Tunnel-Junctions. *Phys. Lett. A* **140**, 251-257 (1989).
90 Geerligs, L. J., Averin, D. V. & Mooij, J. E. Observation of macroscopic quantum tunneling through the Coulomb energy barrier. *Physical Review Letters* **65**, 3037 (1990).
91 Caldeira, A. O. & Leggett, A. J. Quantum Tunnelling in a Dissipative System. *Ann. Phys.* **149**, 374-456 (1983).
92 Martinis, J. M., Devoret, M. H. & Clarke, J. Experimental Tests for the Quantum Behavior of a Macroscopic Degree of Freedom - the Phase Difference across a Josephson Junction. *Physical Review B* **35**, 4682-4698 (1987).
93 Schwartz, D. B., Sen, B., Archie, C. N. & Lukens, J. E. Quantitative Study of the Effect of the Environment on Macroscopic Quantum Tunneling. *Physical Review Letters* **55**, 1547-1550 (1985).
94 Leggett, A. J. Testing the limits of quantum mechanics: motivation, state of play, prospects. *Journal of Physics: Condensed Matter* **14**, R415-R451 (2002).
95 De Franceschi, S. *et al.* Electron Cotunneling in a Semiconductor Quantum Dot. *Physical Review Letters* **86**, 878 (2001).
96 Averin, D. V. & Nazarov, Y. V. Virtual electron diffusion during quantum tunneling of the electric charge. *Physical Review Letters* **65**, 2446 (1990).
97 Geerligs, L. J. *et al.* Frequency-locked turnstile device for single electrons. *Physical Review Letters* **64**, 2691 (1990).

98 Chen, Y.-F., Dirks, T., Al-Zoubi, G., Birge, N. O. & Mason, N. Nonequilibrium Tunneling Spectroscopy in Carbon Nanotubes. *Physical Review Letters* **102**, 036804 (2009).
99 Tinkham, M. *Introduction to Superconductivity*. 2 edn, (Dover, 1996).
100 Berger, C. *et al.* Ultrathin Epitaxial Graphite: 2D Electron Gas Properties and a Route toward Graphene-based Nanoelectronics. *The Journal of Physical Chemistry B* **108**, 19912-19916 (2004).
101 Stander, N., Huard, B. & Goldhaber-Gordon, D. Evidence for Klein Tunneling in Graphene p-n Junctions. *Physical Review Letters* **102**, 026807 (2009).
102 Young, A. F. & Kim, P. Quantum interference and Klein tunnelling in graphene heterojunctions. *Nat Phys* **5**, 222-226 (2009).
103 Heersche, H. B., Jarillo-Herrero, P., Oostinga, J. B., Vandersypen, L. M. K. & Morpurgo, A. F. Induced superconductivity in graphene. *Solid State Communications* **143**, 72-76 (2007).
104 Ojeda-Aristizabal, C., Ferrier, M., Gueron, S. & Bouchiat, H. Tuning the proximity effect in a superconductor-graphene-superconductor junction. *Physical Review B (Condensed Matter and Materials Physics)* **79**, 165436 (2009).
105 Du, X., Skachko, I. & Andrei, E. Y. Josephson current and multiple Andreev reflections in graphene SNS junctions. *Physical Review B* **77**, 184507 (2008).
106 Huard, B., Stander, N., Sulpizio, J. A. & Goldhaber-Gordon, D. Evidence of the role of contacts on the observed electron-hole asymmetry in graphene. *Physical Review B* **78** (2008).
107 Chen, Y.-F. *et al.* Magnetoresistance in Graphene: Weak Localization and Universal Conductance Fluctuation Studies. *arXiv:0910.3737v1* (2009).
108 In all the data there is an unphysical offset of about 0.25 mV in the Bias voltage due to a powered sumbox.
109 Burset, P., Herrera, W. & Levy Yeyati, A. Proximity-induced interface bound states in superconductor-graphene junctions. *Physical Review B* **80**, 041402 (2009).
110 Manjarrés, D. A., Herrera, W. J. & Gómez, S. Andreev levels in a graphene-superconductor surface. *Physica B: Condensed Matter* **404**, 2799-2801 (2009).
111 Zhang, Z. Y. Differential conductance through a NINS junction on graphene. *Journal of Physics-Condensed Matter* **20** (2008).
112 Giovannetti, G. *et al.* Doping Graphene with Metal Contacts. *Physical Review Letters* **101**, 026803 (2008).
113 Park, J. & McEuen, P. L. Formation of a p-type quantum dot at the end of an n-type carbon nanotube. *Applied Physics Letters* **79**, 1363-1365 (2001).